Nuclear Magnetic Resonance Study of the Planar Charge Symmetry under Pressure in High-Temperature Superconducting cuprates

-

Detection of charge ordering in the CuO_2 plane

Der Fakultät für Physik und Geowissenschaften
der Universität Leipzig eingereichte

DISSERTATION

zur Erlangung des akademischen Grades

doctor rerum naturalium
(Dr. rer. nat.)

vorgelegt von

M.Sc. Steven Reichardt
geboren am 24.07.1983 in Sömmerda

Gutachter: Prof. Dr. Jürgen Haase
Prof. Dr. Kazuyoshi Yoshimura

Tag der Verleihung Leipzig, den 26.02.2018

Bibliogaphische Beschreibung

Reichardt, Steven

Nuclear Magnetic Resonance Study of the Planar Charge Symmetry under Pressure in High-Temperature Superconducting cuprates - Detection of charge ordering in the CuO_2 plane

Universität Leipzig, Dissertation, 2017

151 S.*, 130 Lit.*, 56 Abb., 14 Tab.

Referat:

Diese Arbeit befasst sich mit der Charakterisierung der Ladungssymmetrie in der CuO_2 Ebene in den hochtemperatur-supraleitenden Kupraten (HTSCs - high-temperature superconducting cuprates). Hierfür wurden Experimente mit kernmagnetischer Resonance (NMR - nuclear magnetic resonance) an Einkristallen von $YBa_2Cu_3O_7$ und $YBa_2Cu_3O_{6.9}$ sowie an Pulverproben von $YBa_2Cu_4O_8$ durchgeführt. Der Fokus der Arbeit lag auf der Untersuchung des elektrischen Feldgradientens (EFG) der CuO_2 Ebene unter hohem Druck und unterschiedlichen Temperaturen. Neben dem Cu Kern wurde für die Hochdruck-NMR-Untersuchung zum ersten Mal auch der O Kern der CuO_2 Ebene verwendet und für beide Kerne die Druckabhägigkeit des vollständigen EFG Tensors bestimmt. Zusätzlich wurde die Magnetfeldabhängigkeit des EFG untersucht.

Ein Schwerpunkt der Arbeit lag in der Vorbereitung der NMR Druckzelle für Einkristallmessungen sowie deren Ausrichtung im Magnetfeld.

Es konnte gezeigt werden, dass die örtliche Variation des Cu EFG Tensors in allen untersuchten HTSCs stark mit Druck zunimmt und ähnlich groß ist, wie die Variation des EFG durch chemisch induzierte Unordnung.

Durch die Analyse der Cu und O NMR Spektren in $YBa_2Cu_3O_{6.9}$ konnte gezeigt werden, dass der EFG der CuO_2 Ebene nicht direkt durch die orthorhombische Kristallstruktur beeinflusst wird - so wie lange angenommen wurde - sondern durch eine geordnete Ladungsvariation am O erklärt werden muss. Druck und tiefe Temperaturen erhöhen die Ladungsordnung. Es konnte eine eindeutige, lokale Ladungssymmetrie und Amplitude bei 18 kbar und 100 K bestimmt werden, die quantitativ mit den Cu und O Spektren übereinstimmt. Die NMR Daten sind mit einer langreichweitigen Ladungsdichtewelle konsistent.

Zusätzlich wurde herausgefunden, dass das Magnetfeld sowohl die Variation als auch die Orientierung des planaren Cu EFG beeinflusst.

---

[*] ...S. (Seitenzahl insgesamt)
...Lit. (Anzahl der im Literaturverzeichnis ausgewiesenen Literaturangaben)

Mit der Arbeit konnte gezeigt werden, dass Ladungsordnung in Y-basierten HTSCs nahe der Dotierung mit der höchsten kritischen Temperature T_c existiert und sie durch Druck, Variation der Temperatur sowie Magnetfelder beeinflusst werden kann.

Lebenslauf

Persönliche Daten

Steven Reichardt
Geboren am 24.07.1983 in Sömmerda

Bildungsweg

1994 - 2000	**Realschulabschluss** an der Regelschule Rastenberg (Thüringen)
2000 - 2003	**Ausbildung zum Kommunikationselektronikers** bei Hörmann Funkwerk Kölleda GmbH
2003 - 2006	**Abitur** am Thüringen Kolleg Weimar (2.Bildungsweg)
2006 - 2012	**Studium der Physik** an der Universität Leipzig Abschluss 2012: M.Sc. (1.2), Thema der Masterarbeit: *NMR - Double Resonance in a High Temperature Superconductor*
seit 2012	**Promotion** an der Universität Leipzig zum Thema: *Nuclear Magnetic Resonance Study of the Planar Charge Symmetry under Pressure in High-Temperature Superconducting cuprates - Detection of charge ordering in the* CuO_2 *plane*
2012 - 2017	**wissensch. Mitarbeiter** der Universität Leipzig (ESF-geförderte Stelle vom 15.01.2013 bis 31.12.2014)

Stipendium

Alumnus der Studienstiftung des deuschen Volkes

Acknowledgements

The work for this thesis took more than five years and I had to discover that besides the academic education, a large part of it constitutes personal development. Therefore, my first thanks goes to Anna-Lena who always encouraged me, in particular when nothing worked out. Thank you very much. The same gratitude I would like to express to Philipp Schierz who was always deeply interested in scientific and personal topics.

I am grateful to Jürgen Haase for his guidance and patience throughout my work in his group. With his help I learned to question my own results and my physical understanding on a fundamental level.

I want to thank Michael Jurkutat who supported me from the day I started working in the group until now. A lot of my NMR understanding I owe to him. Sorry, that I always bet you in our little game _o. I am also very thankful for all the help and advice from Robin Gühne, Jonas Kohlrautz and Nataliya Georgieva, as well as from Damian Rybicki and Elisabeth Vonhof. The experience of Thomas Meier and Marco Stäter in manufacturing the pressure cells has been very valuable. Without the help from Gert Klotsche and Stefan Schlayer some experimental problems would not have been solved so fast. The helpfulness of the whole MQF group was always great.

I am grateful to Andreas Erb and Grant Williams who provided the samples for this work and helped me especially with the oxygen exchange. I also truly appreciated the additional advice for the oxygen exchange process from Dr. Ruixing Liang and Prof. Dr. Kazimierz Conder. The small single crystals cut by Andreas Erb's group were of inestimable value for this work.

I would also like to thank Bettina Wedel for her help improving some of the photographs and Tobias Lühmann who made it possible to obtain a microscope image of the crystal surface with a polarization filter.

Finally, this work would not have been possible without the skilled workers of our faculty's mechanical and glass blowing workshops .

This work was supported by the European Social Fund (ESF) project no. 100124929 and the Free State of Saxony.

Contents

List of Figures

List of Tables

Abbreviations

BCS	**B**ardeen **C**ooper and **S**chrieffer - founders of the microscopic theory of superconductivity
CDV	charge density variation
CDW	charge density wave
CO	charge ordering
CSW	central of spectral weight (first moment of a distribution)
CT	denotes the NMR central transition ($m = 1/2 \leftrightarrow -1/2$)
Cu(1)	denotes the copper crystal site in the CuO-chains of $\mathrm{YBa_2Cu_3O_{6+y}}$
Cu(2)	denotes the copper crystal site in the $\mathrm{CuO_2}$-plane of $\mathrm{YBa_2Cu_3O_{6+y}}$
EFG	electric field gradient
FID	free induction decay
FWHM	full width at half maximum
HF	high frequency
Iso	indicates that the samples where washed with isopropanol
LF	low frequency
LS	large sample - indicate samples having a size of $\approx 1{\times}1{\times}0.5\,\mathrm{mm}^3$

µS	micro-sample - indicate samples having a size of $\approx 0.15\times 0.1\times 0.1\,\mathrm{mm}^3$
µ-coil	denotes the NMR coil used for the pressure cell. Typical µ-coils have a wire diameter of 20 µm, a height of 150µm, a diameter of 300µm, 4-5 turns and possess high DC-losses($\approx 1\Omega$)
NMR	nuclear magnetic resonance
NQR	nuclear quadrupole resonance
O(1)	denotes the oxygen crystal site in the CuO-chains in $\mathrm{YBa_2Cu_3O_{6+y}}$
O(2)	denotes the oxygen crystal site in the $\mathrm{CuO_2}$-plane of $\mathrm{YBa_2Cu_3O_{6+y}}$ with the CuO-bond axis parallel to the crystal a-axis, i.e., perpendicular to both the CuO-chains and the crystal c-axis
O(3)	denotes the oxygen crystal site in the $\mathrm{CuO_2}$-plane of $\mathrm{YBa_2Cu_3O_{6+y}}$ with the CuO-bond axis parallel to the crystal b-axis, i.e., parallel to the CuO-chains
O(4)	denotes the oxygen crystal site in the BaO-layer of $\mathrm{YBa_2Cu_3O_{6+y}}$
obs.	observed
$\mathrm{O}_{\sigma\parallel}$	denotes the planar oxygen sites having their Cu-O bond parallel to the external magnetic field ($c \perp B_0$)
$\mathrm{O}_{\sigma\perp}$	denotes the planar oxygen sites having their Cu-O bond perpendicular to the external magnetic field ($c \perp B_0$)
SNR	signal to noise ratio
ST	denotes the NMR satellite transition ($m \leftrightarrow m-1$; $m \neq 1/2$)
YBCO	denotes materials of the Y-based cuprate superconductors, e.g., $\mathrm{YBa_2Cu_3O_{6+y}}$ and $\mathrm{YBa_2Cu_4O_8}$

Sites and Orientations

$c \parallel B_0$ or c	indicates sample orientation with B_0 parallel to the crystal c-axis
$c \perp B_0$	indicates sample orientation with B_0 perpendicular to the crystal c-axis
$a \parallel B_0$	indicates sample orientation with B_0 parallel to the crystal a-axis

$b \parallel B_0$	indicates sample orientation with B_0 parallel to the crystal b-axis
$ab \parallel B_0$ or ab	indicates sample orientation of a twinned crystal with B_0 parallel to the crystal a and b-axis at the same time
$\sigma \parallel B_0$ or σ	indicates sample orientation with B_0 parallel to the planar oxygen p_σ bond

Chapter 1

Introduction

The understanding of the superconducting cuprates is still one of the largest challenges in condensed matter physics. At the center of interest is the ubiquitous CuO_2 plane, the total charge content of which controls the rich phase diagram of these materials [Schrieffer and Brooks, 2007]. These planar charges can be ordered under some circumstances and thereby signal new electronic states of broken symmetry. Currently, the significance of planar charge ordering for cuprate physics is widely discussed, in particular, its relation to superconductivity or the pseudogap state. For the experimental investigation and the theoretical understanding of these relations, external parameters are needed to enable the tuning of planar charge ordering. While in the cuprates charge ordering has been investigated by varying the chemical doping level, temperature and the magnetic field strength, the pressure dependence has not been measured with charge sensitive methods yet. Therefore, this work aims at the characterization of the charge symmetry in the CuO_2 plane under *high pressure* using nuclear magnetic resonance (NMR).

NMR is a very powerful local bulk probe for chemical and electronic properties and contributed a lot to the understanding of cuprates, in particular by temperature dependent shift and relaxation measurements [Slichter, 2007; Walstedt, 2008]. Our group has developed high pressure anvil cell NMR and demonstrated its utility for improving our understanding of cuprate physics, for instance by uncovering the disappearance of the pseudogap behavior in the NMR shift under pressure [Meissner et al., 2011]. Besides magnetic interactions, NMR is also very sensitive to the local charge symmetry and its spatial variation through the interaction with the nuclear quadrupole moment. This work focuses on the pressure dependence of the quadrupolar linewidth that has so far been enigmatic to the scientific community.

Most of the cuprates reveal a large quadrupolar linewidth indicating inhomogeneities, which have been attributed to chemical disorder that is mostly considered to be of no particular importance for cuprate physics. However, a few exceptions exist: the stoichiometric materials $\mathrm{YBa_2Cu_3O_7}$ and $\mathrm{YBa_2Cu_4O_8}$ appear to be homogeneous, i.e., show almost no excessive line broadening. In these materials substantial NMR line splittings were observed which have been attributed to their orthorhombic crystal structure. However, also a contradicting explanation for the line splitting is possible: strong charge density variations in the ubiquitous $\mathrm{CuO_2}$ plane of certain symmetry could explain these observations as well. The great advantage of pressure experiments for the investigation of the NMR linewidth is obvious: they allow the modification of the system without introducing chemical disorder. Using pressures high enough to modify the planar electronics but low enough to leave the crystal structure unchanged, it should be possible to separate electronic spatial variation from effects due to the crystal structure.

In chapter 2, the crucial NMR concepts, which allow the measurement of the planar charge symmetry in cuprates will be introduced and a brief overview of selective charge related effects of the $\mathrm{CuO_2}$ plane in cuprates will be given.

Single crystals are needed to determine the planar charge symmetry and the combination of high pressure and single crystal NMR experiments is particularly difficult. The necessity of tiny samples for high pressure experiments constitutes an issue for NMR as a bulk probe. Furthermore, the alignment of a tiny single crystal within anvil pressure cells is not readily done. Therefore, the preparation of the NMR pressure cell for single crystal measurements as well as the orientation procedure of the tiny crystals constituted a main element of the work for this thesis and will be described in chapter 3.

A large modification of the planar Cu (quadrupole) linewidth with pressure, but also with the application of an external magnetic field will be reported in chapter 4. The results show that the increased quadrupolar linewidth by pressure is similar to the line broadening obtained by chemically induced disorder. Pressure inhomogeneities could be ruled out, presenting a surprising result as pressure is not expected to induce such disorder.

It has previously been shown by NMR in underdoped $\mathrm{YBa_2Cu_3O_{6+y}}$, that the magnetic field affects the planar charge symmetry [Wu et al., 2011]. The results presented in this thesis show that there is a similar correlation in $\mathrm{YBa_2Cu_3O_{6+y}}$ close to optimal doping at rather high temperatures. Furthermore, it is revealed that not only the strength, but also the orientation of the magnetic field affect the planar charge symmetry.

The dissent of the NMR line splitting will be resolved in chapter 5. It will be shown that the long-standing interpretation of the NMR line splitting of the planar nuclei as due to the crystal's orthorhombicity is wrong. Furthermore, moderate pressure induces local charge ordering at planar O in $YBa_2Cu_3O_{6.9}$. These observation can be explained by a long-range charge density wave. The results demonstrate that pressure affects planar charge ordering and the existence of charge ordering in $YBa_2Cu_3O_{6+y}$ close to optimal doping.

Chapter 2

Nuclear Magnetic Resonance and the charge distribution in the CuO_2 plane

Cuprate superconductors are ceramic materials with a strongly two dimensional character and despite a great diversity of compositions, the CuO_2 plane is the unique feature of that material class. The charge content of the CuO_2 plane and its spatial distribution determine the essential physical properties: Early on, it was found that the undoped cuprates, so called parent materials, are Mott insulators, however, they become conducting and even superconducting upon doping the CuO_2 plane chemically, e.g., by adding oxygen or substituting rare-earth elements. Depending on the planar charge content, an unusual variety of electronic phases was discovered which are similarly present in all cuprates. Still, the mechanism of the different electronic states, in particular, superconductivity, are not understood. For an overview see for example [Schrieffer and Brooks, 2007]. Furthermore, planar charge ordering (CO), i.e., a spatial modulation of the planar charge content, became another important aspect in the strongly correlated materials and it is discussed how charge ordering is related to the different electronic phases [Chang et al., 2012; da Silva Neto et al., 2014; Tabis et al., 2014]. Pressure on the other hand was found to affect the electronic properties and is suspected to alter the planar doping level substantially. Thus, pressure is a tool to manipulate the electronic properties without changing the material's composition [Schilling, 2007].

In these complex materials, local probes such as nuclear magnetic resonance (NMR) and nuclear quadrupole resonance (NQR) are of particular importance since they can measure site specific information which otherwise are lost in average. Besides magnetic effects, NMR and NQR can measure the local charge symmetry and are thus capable to give information about doping and charge ordering within the plane. For example, it was shown with these methods that the sharing of the charges between the planar Cu and O gives a more precise picture of the superconducting properties than the average planar hole content [Rybicki et al., 2016], e.g., the maximal possible T_c of different cuprate families scales with the oxygen hole content of the related parent materials, cf. Sec. 2.3.2.

For this thesis, NMR and NQR were used to measure the influence of pressure on the planar charge distribution as well as its spatial variation in the Y-family (short YBCO), i.e., $YBa_2Cu_3O_{6+y}$ and $YBa_2Cu_4O_8$, and this chapter will introduce relevant aspects of the system under study and the methods employed, that are necessary to follow the argumentation. First, the structural features of the Y-family are given and the basic principles of NMR and NQR are presented, which allow to disentangle the observed spectra and obtain physical properties. The average doping level of the CuO_2 plane and its relation to different electronic phases is briefly summarized and the pressure dependence on the planar doping level is discussed. It will be shown how NMR and NQR measures the hole contents at planar Cu and O separately, which results in a differentiated perspective on the phase diagram. Charge variation as well as charge ordering in the cuprates will be introduced and their manifestation in the NMR or NQR spectrum is discussed.

2.1 $YBa_2Cu_3O_{6+y}$ and the orthorhombic CuO_2 plane

In this thesis, we focus on the Y-family, i.e., $YBa_2Cu_3O_{6+y}$ and $YBa_2Cu_4O_8$, which are one of the most studied cuprate families. This is mainly due to the fact, that it was the second discovered cuprate superconductor, and the synthesis of high quality specimens is comparatively good accomplished. Furthermore, this material class is interesting for technology since the superconducting transition temperature T_c is above the boiling point of liquid nitrogen accompanied by a high critical current density even at high temperature (77 K) and in high magnetic fields [Hartwig et al., 2012; Schneider-Muntau, 1997].

As shown in Fig. 2.1 (a), the unit cell of $YBa_2Cu_3O_{6+y}$ possesses two CuO_2 planes which are separated by a single layer of Y^{3+} ions. While planar Cu is expected to be in $3d^9$ configuration with an hole in the Cu $3d_{x^2-y^2}$ orbital, planar O is in an almost full $2p^6$ state. However, the hybridization of the O $2p_\sigma$ orbital with the Cu $3d_{x^2-y^2}$ orbital will lead to a small hole content at planar O as well. Note, that the actual sharing of holes between Cu and O varies substantially between different materials, cf. Sec. 2.3.2. The CuO_y chains are separated from the planes by the BaO layer and function as a doping layer as it can receive O along the *b*-direction, while the *a*-direction is unoccupied. In the parent material ($y = 0$), there is no oxygen in the chains and one hole reside at Cu, but oxygenated chains ($y \neq 0$) introduce holes to the system which are not fully compensated by a chain Cu^{2+} state.

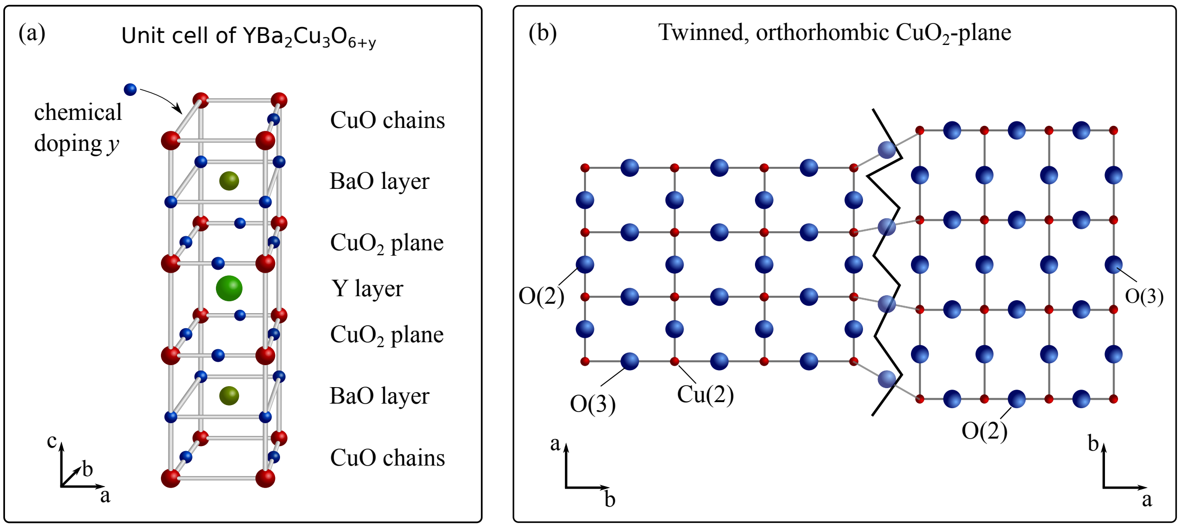

Figure 2.1: (a) Layered strucure of the cuprate $YBa_2Cu_3O_{6+y}$. The two CuO_2 planes are separated by a Y-layer. The chains can be chemically doped with oxygen ($y = 0...1$) along the crystal b-axis, i.e., empty and full chains corresponds to $y = 0$ and $y = 1$, respectively. Doping the chains changes the symmetry from tetragonal to orthorhombic and crystals grow with alternating phases (twinning), i.e., a switch of the a and b-axis. The twinned, orthorhombic CuO_2 plane (b) reveal two chemically inequivalent O sites - O(2) and O(3). For visualization the orthorhombicity is exaggerated by a factor of about 20.

Thus, the chain layers act as hole donors which effectively dope the CuO_2 plane with holes [Walstedt, 2008].

From the crystallographic point of view only the parent material ($y = 0$) and the slightly overdoped compound ($y = 1$) are well defined states (hereinafter referred to as stoichiometric compounds). Intermediate doping levels result in crystal inhomogeneities, however, there are doping levels in which it is possible to have long CuO chains - the so called ortho-phases, e.g., Ortho-II with alternating full and empty chains [Andersen et al., 1999]. An underdoped, stoichiometric representative of the Y-family is $YBa_2Cu_4O_8$, which is structurally similar to $YBa_2Cu_3O_{6+y}$ but contains (fully oxygenated) double CuO chain layers [Karpinski et al., 1988].

Upon doping, $YBa_2Cu_3O_{6+y}$ changes its symmetry from tetragonal $y < 6.4$ to orthorhombic $y > 6.4$ [Conder, 2001]. The resulting distortion of the CuO_2 plane is illustrated in Fig. 2.1 (b). During the growth (synthesis) of the crystal twinning occurs, i.e., the orthorhombicity gives rise to two phases described by a switch of the a and b-axis, cf. Fig. 2.1 (b). While the c-axis is well defined, the two phases alternate with a periodicity of 1-3 µm. Crystal twinning often hampers the analysis of experiments but the crystals can be de-twinned [Liang et al., 2000]. However, for high pressure NMR experiments crystal twinning is of advantage since only two (instead of three) orientations are needed to determine the full set of NMR parameters, and it turned out that twinning allows to draw other important conclusions readily.

For NMR the distinction of different nuclear sites is important and from the chemical structure, there are two distinct Cu sites: one in the CuO_y chains and the other in the CuO_2 planes, which are denoted as Cu(1) and Cu(2), respectively. There are four oxygen sites: the chain O (O(1)) and the apex O (O(4)) are found in CuO_y and BaO-layer, respectively. Due to the orthorhombic structure, there are two planar O sites, i.e., the O(2) site having the Cu-O bond along the crystal a-axis and the O(3) site with the bond along the b-axis. If not explicitly specified, Cu and O refer in this thesis to the planar sites. NMR on Y and Ba is possible but is not of relevance here.

2.2 Nuclear magnetic and nuclear quadrupole resonance of planar nuclei

Nuclear resonance methods are based on the energy splitting of nuclear spin states and the inspection of their transitions. While for nuclear magnetic resonance (NMR) the splitting is in leading order due to the interaction of the nuclear magnetic moment with an external magnetic field (Zeeman interaction), for nuclear quadrupole resonance (NQR) it is solely due the interaction of the nuclear quadrupole moment with the electric field gradient at the nucleus. In both cases, the spin states (described by the density matrix) can be mixed by the perturbation of the system with an oscillating magnetic field. The resulting magnetization oscillates with a frequency determined by the nuclear energy splitting.

Thereby, the nuclei provide a local probe of the sample to be investigated, i.e., even in complex systems it is possible to address experiments to specific sites, but always as a histogram of all nuclei of that site. Various nuclei and their isotopes, different chemical sites and inhomogeneous electronic states can give rise to a rich frequency spectrum. From the evaluation of the obtained spectra, e.g., position of the lines, line assignment and also the width of lines, valuable microscopic information can be extracted - touchstones for new theories.

With regard to the cuprates' planar Cu and O, in this section the basic principles of both resonance techniques are presented and interactions relevant for this thesis are introduced. A comprehensive overview about cuprate NMR can be found in the following references [Pennington and Slichter, 1990; Slichter, 2007; Walstedt, 2008].

2.2.1 Principles of NMR

Magnetic contributions to the NMR spectrum Nuclei with a non-vanishing spin ($I \geq 1/2$) possess a magnetic moment which gives rise to $2I+1$ Zeeman levels in an external magnetic field B_0, labeled with m ($m = -I, -I+1, ..., I$). The equidistant splitting between those energy levels is characterized by the Larmor frequency:

$$\omega_0 = 2\pi\nu_0 = \gamma B_0, \tag{2.1}$$

with the nuclear gyromagnetic ratio γ.

In addition, the external magnetic field induces virtual orbital currents and polarizes electron spins within the sample. Both effects generate additional magnetic fields at the nuclear site which affects the Zeeman splitting and are captured by the magnetic shift K:

$$\nu_{\mathrm{mag}} = (1+K)\nu_0. \tag{2.2}$$

It is customary to decompose the shift into $K = K^{\mathrm{L}} + K^{\mathrm{S}}$ with an orbital K^{L} and a spin K^{S} part. Those mechanisms can be anisotropic, which is expressed by the shift tensor $\boldsymbol{K}$ characterized by its principle values K_{ll} which are obtained by aligning the magnetic field along the tensor's principle axis $l = X, Y, Z$. The shift can be decomposed into an isotropic $K_{\mathrm{iso}} = (K_{XX} + K_{YY} + K_{ZZ})/3$ and an anisotropic $K_{\mathrm{ani}} = K_{ZZ} - K_{\mathrm{iso}}$ part:

$$K(\beta, \alpha) = K_{\mathrm{iso}} + K_{\mathrm{ani}}\, A(\beta, \alpha, \eta_{\mathrm{m}}), \tag{2.3}$$

where the orientation of the principle axis system with respect to B_0 is given by:

$$A(\beta, \alpha, \eta_{\mathrm{k}}) = \frac{3\cos^2\beta - 1}{2} + \frac{\eta_k}{2}\sin^2\beta\cos 2\alpha; \quad k = m, q\,, \tag{2.4}$$

with the Euler angles β and α as well as the anisotropy parameter $\eta_{\mathrm{m}} = (K_{XX} - K_{YY})/K_{\mathrm{ani}}$ [1].

Quadrupole contributions to the NMR spectrum Besides magnetic interactions, the nuclear energy levels can be altered by electrostatic interactions. Quadrupole nuclei ($I > 1/2$) possess an electric quadrupole moment eQ which interacts with the electric field gradient (EFG) at the nuclear site. Thereby, the Zeeman levels m are modified and they are not equidistant any more,, cf. Fig. 2.2. Since eQ is known, NMR is capable to measure the EFG (V_{ij}) which is generated by the surrounding charge distribution of the nucleus. In its principle

---

[1] $K(90,0) = K_{XX}$; $K(90,90) = K_{YY}$; $K(0,\alpha) = K_{ZZ}$

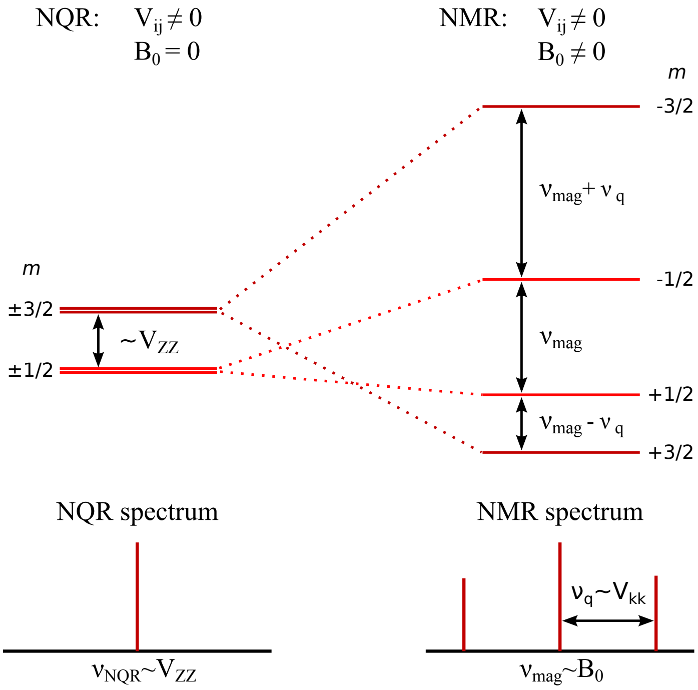

Figure 2.2: Schematic nuclear energy levels for a nuclear spin $I = 3/2$ and corresponding spectra. (left) Without an external magnetic field (B_0), the degeneration of the nuclear spin levels is lifted due to the interaction of the quadrupole nuclei with a non-vanishing electric field gradient (V_{ij}) at the nuclear site. Nuclear quadrupole resonance (NQR) can inspect the energy splitting of the Kramer doublet which results in a single line proportional to the largest EFG principle value V_{ZZ}. (right) In high magnetic fields, the Zeeman interaction is much larger than the quadrupole interaction ($\nu_{\text{mag}} \gg \nu_q \sim eQV_{ZZ}/2h$) and the latter is treated as a perturbation of the former. Using nuclear magnetic resonance (NMR), three lines ($2I$) can be observed. Aligning the magnetic field with the EFG's principle axis system $l = X, Y, Z$, the splitting between the lines measures the respective principle values V_{ll}.

axis system ($l = X, Y, Z$), the EFG is diagonal with its principle values V_{ll}. However, the EFG as a traceless tensor is already described by a set of two parameters, i.e., the quadrupole frequency $\nu_{\text{Q}} = 3eQV_{ZZ}/2I(2I-1)h$ and the asymmetry parameter $\eta_{\text{q}} = (V_{XX} - V_{YY})/V_{ZZ}$ with the convention $|V_{XX}| \leq |V_{YY}| \leq |V_{ZZ}|$. The spectrum of quadrupole nuclei consists of a central transition ($m = 1/2$) and $2I - 1$ satellite transitions, cf. Fig. 2.2, and is described by:

$$\nu_{(m \leftrightarrow m-1)} = \nu_{\text{mag}} + \nu_{\text{q},(\text{m}\leftrightarrow\text{m}-1)}. \tag{2.5}$$

While the quadrupolar contribution differs for each transition ($m \leftrightarrow m - 1$), the magnetic part remains the same, cf. Fig. 2.2. To simplify notation, the subscript for the transition in the quadrupolar part is omitted. The influence of the quadrupole interaction in high magnetic fields ($\nu_{\text{mag}} \gg \nu_{\text{Q}}$) is obtained by perturbation theory, i.e., $\nu_{\text{q}} = \nu_{\text{q}}^{(1)} + \nu_{\text{q}}^{(2)} + \nu_{\text{q}}^{(3)} + \ldots$. The

Table 2.1: Quadrupole correction for $I = 3/2$ up to third order with the magnetic field B_0 along ($\beta = 0°$) and perpendicular ($\beta = 90°$) to the main principle axis of the EFG. For simplicity: $\kappa = \cos(2\alpha)$

Spin 3/2 - Central transition ($1/2 \leftrightarrow -1/2$)

	$\beta = 0$	$\beta = 90$
$\nu_{\mathrm{q}}^{(1)}$	0	0
$\nu_{\mathrm{q}}^{(2)}$	$\frac{\nu_{\mathrm{Q}}^2}{12\nu_{\mathrm{mag}}}\eta^2$	$\frac{\nu_{\mathrm{Q}}^2}{2\nu_{\mathrm{mag}}}\left(\frac{3}{8} + \frac{1}{4}\eta\kappa + \frac{3}{8}\eta^2\kappa^2 - \frac{1}{3}\eta^2\right)$
$\nu_{\mathrm{q}}^{(3)}$	0	0

Spin 3/2 - Satellite transition ($m \leftrightarrow m-1$)

	$\beta = 0$	$\beta = 90$
$\nu_{\mathrm{q}}^{(1)}$	$-(m-\frac{1}{2})\nu_{\mathrm{Q}}$	$(m-\frac{1}{2})\frac{\nu_{\mathrm{Q}}}{2}(1-\eta\kappa)$
$\nu_{\mathrm{q}}^{(2)}$	0	$\frac{\nu_{\mathrm{Q}}^2}{6\nu_{\mathrm{mag}}}\eta^2(1-\kappa^2)$
$\nu_{\mathrm{q}}^{(3)}$	$(m-\frac{1}{2})\frac{\nu_{\mathrm{Q}}^3}{24\nu_{\mathrm{mag}}^2}\eta^2$	$-(m-\frac{1}{2})\frac{\nu_{\mathrm{Q}}^3}{4\nu_{\mathrm{mag}}^2}\left(\frac{3}{16} - \frac{\eta\kappa}{16} - \frac{7\eta^2\kappa}{16} + \frac{\eta^2}{3} - \frac{\eta^3\kappa}{3} + \frac{15\eta^3\kappa^3}{48}\right)$

leading order affects only the satellite transitions (ST) and is given by:

$$\nu_{\mathrm{q}}^{(1)}(\beta,\alpha) = (m - 1/2) \cdot \nu_{\mathrm{Q}} \cdot A(\beta,\alpha,\eta_{\mathrm{q}}). \tag{2.6}$$

The angular dependence $A(\beta,\alpha,\eta_{\mathrm{q}})$ is also given by Eq. (2.4) but here β and α measures the orientation of the EFG in respect to B_0[1]. In second order all transitions are affected but for the course of this thesis only the angular dependence of the central transition (CT) with vanishing asymmetry ($\eta_{\mathrm{q}} = 0$) is needed:

$$\nu_{\mathrm{q}}^{(2)}(\beta) = \frac{3\nu_{\mathrm{Q}}^2}{16\nu_{\mathrm{mag}}}\sin^2\beta(9\cos^2\beta - 1). \tag{2.7}$$

Determination of the shift and EFG tensor in YBCO The shift and EFG tensors are determined by the local symmetry, and thus, in YBCO, planar Cu and O have their shift and EFG principle axis system along the unit cell axis, i.e., along the planar Cu-O bond direction (a, b -axis) and perpendicular to the plane (c-axis). While the largest principle values of both shift and EFG tensors for Cu are along the c-axis, for O they are along the planar Cu-O bond, i.e., obtained along the a and b-axis [Pennington and Slichter, 1990; Walstedt, 2008].

The principle axis system of the planar nuclei were aligned with B_0 using the angular

---

[1] $\nu_{\mathrm{q}}^{(1)}(90,0) \propto V_{XX}$; $\nu_{\mathrm{q}}^{(1)}(90,90) \propto V_{YY}$; $\nu_{\mathrm{q}}^{(1)}(0,\alpha) \propto V_{ZZ}$

Table 2.2: Quadrupole correction for $I = 5/2$ up to second order with the magnetic field B_0 along ($\beta = 0°$) and perpendicular ($\beta = 90°$) to the main principle axis of the EFG. For simplicity: $\kappa = \cos(2\alpha)$

Spin 5/2 - Central transition ($1/2 \leftrightarrow -1/2$)

	$\beta = 0$	$\beta = 90$
$\nu_\mathrm{q}^{(1)}$	0	0
$\nu_\mathrm{q}^{(2)}$	$\frac{2\nu_\mathrm{Q}^2}{9\nu_\mathrm{mag}}\eta^2$	$\frac{4\nu_\mathrm{Q}^2}{3\nu_\mathrm{mag}}\left(\frac{3}{8}+\frac{1}{4}\eta\kappa+\frac{3}{8}\eta^2\kappa^2-\frac{1}{3}\eta^2\right)$

Spin 5/2 - Satellite transition ($m \leftrightarrow m-1$)

	$\beta = 0$	$\beta = 90$
$\nu_\mathrm{q}^{(1)}$	$-(m-\frac{1}{2})\nu_\mathrm{Q}$	$(m-\frac{1}{2})\frac{\nu_\mathrm{Q}}{2}(1-\eta\kappa)$
$\nu_\mathrm{q}^{(2)}$ $(m = \frac{3}{2}; -\frac{1}{2})$	$\frac{5\nu_\mathrm{Q}^2}{36\nu_\mathrm{mag}}\eta^2$	$\frac{\nu_\mathrm{Q}^2}{24\nu_\mathrm{mag}}\left(\frac{15}{2}+5\eta\kappa+\frac{7}{2}\eta^2\kappa^2-\frac{8}{3}\eta^2\right)$
$\nu_\mathrm{q}^{(2)}$ $(m = \frac{5}{2}; -\frac{3}{2})$	$-\frac{\nu_\mathrm{Q}^2}{9\nu_\mathrm{mag}}\eta^2$	$-\frac{\nu_\mathrm{Q}^2}{12\nu_\mathrm{mag}}\left(3+2\eta\kappa+11\eta^2\kappa^2-\frac{32}{3}\eta^2\right)$

dependence of the Cu CT and the O ST which will be discussed in Sec. 3.2.3. For the deconvolution of the obtained spectra in different orientations the explicit quadrupole corrections up to third order [Wolf et al., 1970] were used which are shown in Tab. 2.1 and Tab. 2.2. For both planar Cu and O with the magnetic field (11.7 T) along the main principle axis, only first order quadrupole interaction has to be taken into account ($\nu_\mathrm{q}^{(2)} < 1\,\mathrm{kHz}$). Thus, the largest shift and EFG components are directly measured by the position of the CT and the difference between the satellites (or difference between the ST and CT), respectively, cf. Fig. 2.2. However, with the magnetic field along the other two principle axes higher order quadrupole corrections have to be used. For planar O, the second order term is significant but small ($\nu_\mathrm{q}^{(2)} < 10\,\mathrm{kHz}$) and each transition (also the CT) was corrected according to Tab. 2.2. The corrected set of five lines reveals than the magnetic shift and EFG component of the particular orientation. For planar Cu in YBCO, the situation is not straightforward since the satellites reveal a double peak pattern with different peak intensities and its origin is a central issue of this thesis. The NMR parameters were obtained in following way. The quadrupole frequency ν_Q measured with NMR for $c \parallel B_0$ (but also with NQR) was used to calculate η_q from the more intense satellite line. Both EFG parameters enable to correct the CT for second order effects and reveal the magnetic contribution. Note, that the third order contribution to the ST is substantial for Cu, i.e., $\nu_\mathrm{q}^{(3)} \approx 80\,\mathrm{kHz}$ at 11.7 T.

The NMR lines can also be calculated by a numerical diagonalization of the nuclear spin and quadrupole Hamiltonian[Walstedt, 2008]. Using the distribution $S_\mathrm{NQR}(V_{ZZ})$ of the largest planar Cu EFG component V_{ZZ} measured by NQR (see below) as well as the determined Cu shift tensor $\boldsymbol{K}$ and the EFG asymmetry parameter η_q, this method allows to simulate the quadrupole broadened planar Cu NMR lines $S_{(m\leftrightarrow m-1)}(V_{ZZ})$. The obtained distribution $S_{(m\leftrightarrow m-1)}(V_{ZZ})$ reveals the manifestation of $S_\mathrm{NQR}(V_{ZZ})$ in the NMR spectrum for a particular orientation, i.e., the position and shape of all three Cu NMR transitions for non-interacting nuclear spins possessing a well defined shift $\boldsymbol{K}$ as well as EFG asymmetry η_q but including a variations of V_{ZZ}. Thus, the distribution of V_{ZZ} measured without a magnetic field can be compared with the measured NMR lines which will be of importance for this thesis.

Excitation and detection Without quadrupolar effects, the external magnetic field lifts the degeneracy of nuclear spin states by changing their energies. According to Boltzmann statistics, the individual spin states of N nuclear spins I are differently occupied in equilibrium. The resulting macroscopic magnetization is given by the Curie law:

$$M_0 = \frac{N\gamma^2\hbar^2 B_0 I(I+1)}{3k_B T}. \tag{2.8}$$

The observation of resonances is due to the mixing of the nuclear spin states by an alternating magnetic field whose frequency matches the corresponding energy splittings, i.e., typical magnetic fields in the range of $1-20\,\mathrm{T}$ requires radio frequency (RF) fields of $10-1000\,\mathrm{MHz}$. This is achieved in (pulse) NMR by applying a strong and short RF pulse in a coil in which the sample is embedded. The induced linear polarized RF-field of amplitude B_RF can be decomposed into two circularly polarized fields of amplitude $B_1 = B_\mathrm{RF}/2$. While for NQR both circular fields induce transitions, cf. Sec. 2.2.2, for NMR, only one component couples effectively to the nuclear spins. In case of pure Zeeman splitting, the pulse of duration t_p perturbs the spin states in such a way that parts of the equilibrium magnetization $M_0 \parallel B_0 \parallel z$ are rotated into xy-plane ($\perp z$):

$$M_{xy} = M_0 \sin\gamma B_1 t_\mathrm{p} \tag{2.9}$$

$$M_z = M_0 \cos\gamma B_1 t_\mathrm{p}. \tag{2.10}$$

Thus, for $t = t_{\pi/2} \equiv \pi/2\gamma B_1$, the magnetization is completely flipped into the xy-plane and the pulse is called $\pi/2$-pulse. Furthermore, an inversion of the magnetization is achieved by a π-pulse, i.e., $t = t_\pi \equiv \pi/\gamma B_1$. After a $\pi/2$-pulse the magnetization oscillates within the xy-plane which thereby induces a measurable alternating voltage in the coil. The observed voltage is proportional to NB_0^2/T and thus is increased in higher magnetic fields and for lower temperatures. For high pressure experiments, only small samples can be used, cf. Sec. 3.2.1, containing less spins N, which makes high pressure NMR experiments particularly difficult.

In the presence of quadrupole interaction, the $\pi/2$-pulse is only well defined if all transitions are excited equally (non-selective). However, for the excitation of certain transitions, the pulse length which maximizes the in-plane magnetization M_{xy} as well as the observed intensity depends on the selected transition. The scaling of the pulse length and intensities between different transitions can be found in Man et al. [1988].

Relaxation processes The nuclear spin magnetization is disturbed from thermal equilibrium ($M_0 \parallel B_0$) by the excitation of the nuclear spins and relaxes back to thermal equilibrium after the pulse. The time constant T_1, called spin-lattice relation time, is characteristic for the relaxation process and is determined by the energy transfer between the nuclear spin system and the "lattice", i.e., any subsystem which can accept energy from the nuclei as for example scattering of conduction electrons. Using the inversion recovery experiment, cf. Sec. 3.1.1, the relaxation process can be followed and T_1 can be extracted using a multiple-exponential decay (for quadrupole split energy levels). For example, for a perfect inversion of the CT of Cu, the deviation from the equilibrium magnetization M_0 for a time τ_{sep} after the inversion is described by

$$M(\tau_{\text{sep}}) - M_0 = -M_0 \left(0.1 e^{-\tau_{\text{sep}}/T_1} + 0.9 e^{-6\tau_{\text{sep}}/T_1} \right) . \tag{2.11}$$

A comprehensive discussion of the relaxation of quadrupole nuclei can be found in Suter et al. [1998].

After the $\pi/2$-pulse, the magnetization oscillates with the transition-specific frequency $\nu_{(m \leftrightarrow m-1)}$ in the xy-plane. However, there will be always a spatial frequency distribution, cf. Sec. 2.2.3, and spins will accumulate a phase difference. After the characteristic time T_2, the phase of the spins in the xy-plane is almost randomly distributed and the measurable magnetization (above noise) is gone. This process which is not necessarily related to an energy exchange is called transversal relaxation and, depending on the origin, it can be given by an exponential decay. In many solids the macroscopic magnetization is lost before the spectrometer is able to measure it[1], however, except for some contribution, e.g., contributions from equal spins (homonuclear) or from spin-lattice relaxation (Redfield-contribution), the magnetization can be "refocused" using an additional π-pulse. This pulse sequence is called spin echo, cf. Sec. 3.1.1, and by varying the time between the two pulses the spin echo decay can be inspected.

---

[1] There is a deadtime of the spectrometer due to ring down of the RF-components after a high power excitation pulse.

2.2.2 Nuclear quadrupole resonance

In this section, the basic principles of nuclear quadrupole resonance (NQR) are introduced for a spin $I = 3/2$. A comprehensive overview of NQR can be found in [Das and Hahn, 1958].

The presence of an electric field gradient (EFG) at the nuclear site lifts the degeneracy of the energy levels of quadrupole nuclei ($I > 1/2$) even in the absence of an external magnetic field. For a spin $I = 3/2$, the energy levels can be calculated analytically which results in a Kramer doublet, cf. Fig. 2.2, and the transition frequency is given by:

$$\nu_{(\pm 3/2 \leftrightarrow \pm 1/2)} = \nu_{\mathrm{Q}} \left(1 + \frac{\eta^2}{3}\right)^{1/2} \tag{2.12}$$

Both ν_{Q} and η can not be obtained from a pure spin-3/2 NQR spectrum, however, for planar Cu the asymmetry is small ($\eta < 0.02$) and the observed spectra reveal the distribution $S_{\mathrm{NQR}}(V_{ZZ})$ of the largest EFG component[1].

In equilibrium, the spin states $\pm m$ are equally occupied and thus give no net magnetization. Still, transitions between the energy levels can be induced in the same way as for NMR. An oscillating magnetic field which is applied along the X-axis of the EFG's principle axis system, couples to the nuclear spins and generates a time-dependent perturbation of the nuclear spin states. Thereby, generating a macroscopic oscillating magnetization $M_X \propto \sin(\sqrt{3}\gamma B_1 t_{\mathrm{p}}) \sin(\nu_{\pm 3/2 \leftrightarrow \pm 1/2} t)$, which is in fact linearly polarized, i.e., $M_Y = M_Z = 0$ [Bloom et al., 1955]. Since transitions between $(3/2 \leftrightarrow 1/2)$ and $(-3/2 \leftrightarrow -1/2)$ are possible, both circular polarized field components (decomposition of linear polarized RF-field) couple to spin system[2]. The maximal magnetization is achieved if $t_{\mathrm{p}} = \pi/2\sqrt{3}\gamma B_1$. Note, that only components of the RF-field perpendicular to the main principle axis Z of the EFG can induce transitions with $\Delta m = \pm 1$ and the excitation is most efficient if the applied RF-field oscillates along the X-axis. Therefore, for powders, some crystallites are not excited at all (RF-field parallel to Z) and for the others crystallites the excitation conditions are not well defined. The powder average is described by a sum of Bessel functions [Bloom et al., 1955] and results in a smaller macroscopic magnetization compared to the excitation of a single crystal. Clearly, this effect is enhanced if multiple pulse sequences are used, e.g., spin echo pulse sequence.

After the pulse sequence, similar to NMR, the oscillating macroscopic magnetization of a system containing N spins which is described by Boltzmann statistics give rise to a voltage in the coil which is proportional to $N\nu_{\mathrm{Q}}^2/T$. Furthermore, spin-lattice relaxation processes

---

[1] η contributes by less than 2 kHz which can be neglected for the broad spectra (> 100 kHz).

[2] In a spin-1/2 formalism one could describe the problem with $\pm\gamma$, i.e., spins precess in opposite sense.

generate equilibrium population of the spin states and T_2-processes generate incoherences of the oscillating nuclear magnetic moments. Both effects lead to the decay of the measured oscillating voltage.

2.2.3 Frequency distribution of the NMR and NQR spectra

A major issue of this thesis is to investigate the origin of the large NMR frequency distributions observed for the planar nuclei in the cuprates. On the basis of the above introduced principles, NMR on a single quadrupolar nucleus would result in a spectrum of $2I$ delta peaks[1]. However, for a solid with 10^{23} nuclear spins, the interaction among the spins as well as inequivalent nuclear sites due to the spatial variation of NMR parameters give rise to a frequency distribution. Thereby, the lineshape can reveal (symmetric) line broadening, for example caused by a random distribution of NMR parameters, but also complex patterns may be observed, for example, due to inequivalent nuclear sites.

Two broadening mechanism due to magnetic interactions will be discussed here. A spatial distribution of the shift components ΔK_{ll} $(l = X, Y, Z)$ will give rise to a frequency distribution which is proportional to B_0. In addition, broadening due to nuclear dipole-dipole interaction is caused by the variation of the dipolar field at the nuclear site and can be calculated using the methods of moments [Slichter, 1990]. Note, that the latter interaction is independent of the applied magnetic field[2]. Both mechanisms affect the CT and ST equally and since they are not distinguished in this thesis, the total magnetic linewidth in different directions l is given by $\sigma_{\mathrm{mag},l}$.

A spatial distribution of the EFG, i.e., ΔV_{ll} $(l = X, Y, Z)$, will cause in first-order a variation of the satellite frequency which is independent of B_0 as long as the EFG is independent of the magnetic field, cf. Tab. 2.1 and 2.2. The variation of the EFG principle values is measured by $\sigma_{\mathrm{q},l}$ in frequency units. The second-order quadrupole contribution $\sigma^{(2)}_{\mathrm{q},n}$ can be estimated by $\sigma^{(2)}_{\mathrm{q},n} = \frac{d\nu^{(2)}_{\mathrm{q}}}{d\nu_{\mathrm{Q}}}\sigma_{\mathrm{q}}$ and it is inversely proportional to ${B_0}^3$. Third order effects can be neglected since even for a large quadrupolar distribution of 1 MHz (for Cu) the broadening is two orders of magnitude smaller in the used magnet of 11.7 T.

Besides the qualitative analysis of the lineshape, a simple approach is used to separate different contributions to the experimentally determined width $\sigma_{\mathrm{exp},n}$ of the different transitions

---

[1] Inhomogeneities of the magnetic field ($<$ 10 ppm) as well as linewidth due to lifetime of spin states are neglected and thus only linewidths larger than 1 kHz are discussed.

[2] Dipole-dipole interaction broadens the NQR line as well, however, it can be neglected for the NQR spectrum of planar Cu, since the EFG distribution is much larger, cf. Sec. 4.2.

[3] From the size of the quadrupolar interaction in the used magnetic field of 11.7 T one can show that second-order broadening is only important for the Cu CT.

$n = m - 1/2$ (for $m \leftrightarrow m-1$):

$$\sigma^2_{\mathrm{exp},n} = \sigma^2_{\mathrm{mag}} + 2n \left\langle \sigma_{\mathrm{mag}} \sigma_{\mathrm{q}} \right\rangle + n^2 \sigma^2_{\mathrm{q}} + (\sigma^{(2)}_{\mathrm{q},n})^2, \tag{2.13}$$

where $\langle \sigma_{\mathrm{mag}} \sigma_{\mathrm{q}} \rangle$ reflects possible correlations between magnetic and quadrupolar contributions which can be significant in the cuprates [Haase et al., 2000].

The NQR frequency distribution is affected by the EFG but also magnetic effects as the dipole-dipole interaction or unshielded magnetic fields such as earth's magnetic field or stray fields can in principle influence the NQR linewidth. However, these effects were found to be negligible for the investigated cuprates[1]. Thus, the linewidth and shape is solely given by the variation of the EFG. Again, since the EFG asymmetry η is small, the variation of the largest principle components dominates the quadrupolar contribution, cf. (2.12), which is quantified by the linewidth $\sigma_{\mathrm{q,Z}}$. Note, that a variation of η which is not revealed by the NQR spectrum may still contribute to the NMR lines.

To conclude, from the comparison of the lineshape and width of different transitions, in different magnetic fields and for different orientations valuable information regarding the origin of the linewidth can be determined.

2.3 The charge distribution in the CuO_2 plane

The study of the charge distribution of the CuO_2 plane in YBCO is the main topic of the presented thesis. The term charge distribution includes two aspects: First, it was found that doped charges do not add to the CuO_2 plane uniformly but are shared between planar Cu and O differently. This opens up a new dimension, and different cuprate properties, e.g., the pressure response of T_c, has to be discussed in this new perspective. Second, there is a large spatial charge variation within the CuO_2 plane which in some cases reveals ordered structures. However, the origin of this variation and its relation to cuprate properties is unclear.

The charge distribution of the CuO_2 plane is investigated by applying moderate stress to the material, i.e., magnetic fields, various temperatures and moderate pressures. While this leaves the chemical structure largely unchanged, the electronics are altered and the origin of the charge distribution may be revealed.

In the next sections, the relevant background for the latter discussions will be introduced and some related details of the large body of publications in this field will be highlighted.

---

[1] Stray fields were excluded by comparing the lines of the two Cu isotopes and since the CT is much more narrow than the ST in high fields one conclude that dipole-dipole interaction does not significantly contribute to the NQR line.

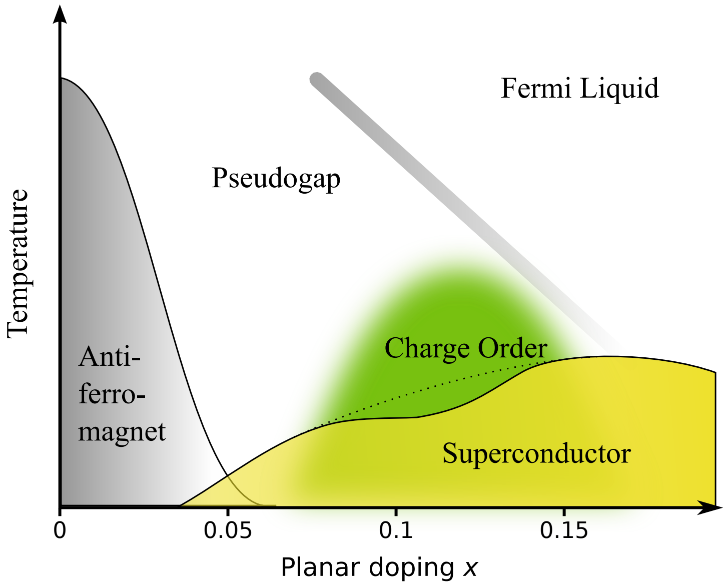

Figure 2.3: Schematic phase diagram of $YBa_2Cu_3O_{6+y}$ exhibits the most prominent electronic phases of the cuprate superconductors. The parent material ($x = 0$) is an insulator with an antiferromagnetic ground state. Upon doping the material becomes conducting and even superconducting below T_c while the long range antiferromagnetic order vanishes. The superconducting phase is customarily described as a dome-like doping dependence centered near $x = 0.15$ (dotted line), but is suppressed in the underdoped region ($x \approx 0.125$). This anomaly coincides with the appearance of charge order.

2.3.1 Doping the cuprates - the classical phase diagram

Cuprate superconductors can be doped chemically and by this the average hole content of the CuO_2 plane is altered by x. Based on whether holes are added ($x > 0$) or removed ($x < 0$), one distinguishes between hole doped or electron doped materials. For a few compounds such as $La_{2-x}Sr_xCuO_4$, the average planar doping level x can be directly deduced from the stoichiometry[1], however, for most cuprates it is difficult to estimate x and it is customarily referred to T_c, see for example Liang et al. [2006] for $YBa_2Cu_3O_{6+y}$. Nevertheless, upon varying x different electronic phases occur which are similarly found in all cuprates and they are usually summarized in an electronic phase diagram (x, T). A schematic phase diagram of YBCO is depicted in Fig. 2.3 as a representative for the doping related phenomenology of the cuprates. The undoped materials ($x = 0$) are insulators with an antiferromagnetic ground state. Upon doping, the cuprates become conducting and even superconducting, while the antiferromagnetic long range order vanishes. At optimal doping ($x \approx 0.15$), the materials reveal their maximal T_c. Doping levels below and above optimal doping are referred to as

---

[1] For these compounds, x is also used in the molecular formula. For materials, where x is not simply related to the composition, the chemical doping is denoted by y or δ.

underdoped and overdoped, respectively. The critical temperature $T_c(x)$ is usually described by a parabolic doping dependence, however, an abnormal suppression of T_c is found close to $x = 0.125$ (1/8-anomaly) in some systems, i.e., there is a plateau in $T_c(x)$ in $YBa_2Cu_3O_{6+y}$ [Liang et al., 2006] or even a singular spot where T_c almost vanishes in $La_{2-x}Ba_xCuO_4$ [Moodenbaugh et al., 1988]. Since this suppression was found to be accompanied by spin and charge ordering [Tranquada et al., 1995], the relation between superconductivity and other ordering phenomena gained a lot of interest, cf. Sec. 2.3.4. At higher temperatures in the underdoped region, the pseudogap phase below T^* is encountered where the electronic behavior is somewhat similar to a metal with an electronic gap. Still, the origin of this phase is unclear but the relation to the planar hole content in general and charge ordering in particular are discussed [Parker et al., 2010]. Overdoped materials show a "normal" metal-like behavior. Evidently, fundamental physical properties are modified by planar doping and NMR and NQR contributed to the discovery, characterization and understanding of the different phases [Slichter, 2007; Walstedt, 2008].

Clearly, the (x, T)-phase diagram can not cover all phenomena of the cuprates, e.g., it is well known that magnetic fields but also pressure can affect the superconducting state. Since magnetic fields are not expected to change the average doping level, it constitutes a new dimension. However, pressure is suspected to modify the planar doping level, but also fundamental electronic properties, e.g., the superconducting pairing mechanism [Schilling, 2007] or the electronic properties in the pseudogap phase [Meissner et al., 2011]. Obviously, the separation of doping and non-doping related pressure effects is of great importance for the understanding of this material class. Charge ordering seems to be most prominent in the underdoped materials but it is controversial whether it is an omnipresent feature of the superconducting cuprates, cf. Sec. 2.3.4 for details. If pressure is able to change the planar charge content, the question arises whether pressure affects planar charge ordering as well. In addition, a principle issue regarding the doping of the plane and charge ordering is the role of charge distribution between planar Cu and O which is not covered in the classical phase diagram. In the following sections, some mentioned aspects will be discussed in more detail which will help to introduce and motivate the presented investigation of YBCO with NMR and NQR under pressure.

2.3.2 Planar charge distribution measured by NMR - a new perspective on the phase diagram

Even though most phenomena can be well ordered in the common phase diagram according to their position in respect to the maximal T_c which occurs at about $x = 0.15$ in all cuprates,

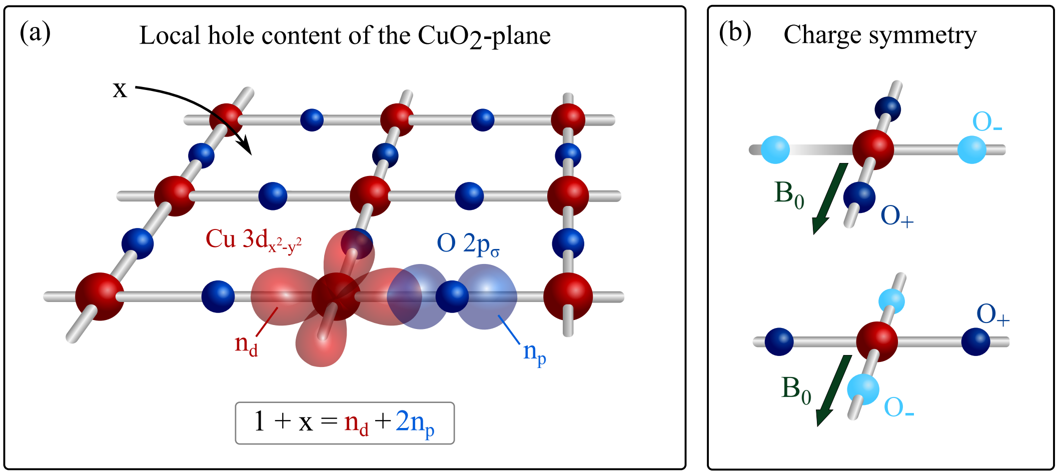

Figure 2.4: Cu and O hole contents and the local charge symmetry in the ubiquitous CuO_2 plane of the cuprates. (a) Doped holes x are shared differently among the planar bonding orbitals Cu $d_{x^2-y^2}$ (n_d) and O $2p_\sigma$ (n_p) obeying $1+x = n_\mathrm{d}+2n_\mathrm{p}$. (b) NMR can distinguish differently charged O orbitals denoted by O_+ and O_- and for a given magnetic field direction B_0, the charge symmetry of the local CuO_4 unit can be analyzed.

their extension can vary drastically, e.g. the size of the maximal T_c changes from 38 K in $La_{2-x}Sr_xCuO_4$, over 93 K in $YBa_2Cu_3O_{6+y}$ to 133 K in $HgBa_2Ca_2Cu_3O_{8+\delta}$. Recently, our group found that the cuprates are ordered according to their maximal T_cs if one takes the hole content of planar Cu and O into account [Jurkutat et al., 2014; Rybicki et al., 2014, 2016]. The study is based on the observation, that the electric field gradients (EFGs) of the planar nuclei as measured by NMR are determined by the hole content of the planar bonding orbitals, i.e., by n_p the hole content of O $2p_\sigma$ which is hybridized with Cu $3d_{x^2-y^2}$ having a hole content of n_d, cf. Fig. 2.4 (a). Since this analysis is of great importance for later interpretations of the measured data it will be explained in some detail.

The EFG measures the local charge symmetry and thereby also the partial occupation of non s-like orbitals. Using the electric hyperfine coefficients determined by atomic spectroscopy, Haase et al. [2004] obtained relations between the hole contents n_p and n_d and the NMR quadrupole frequencies of planar Cu and O:

$$^{17}\nu_{\mathrm{Q},\sigma} = 2.453\ \mathrm{MHz} \cdot n_p + {}^{17}C_c \tag{2.14}$$

$$^{63}\nu_{\mathrm{Q,c}} = 94.3\ \mathrm{MHz} \cdot n_d - 5.68\ \mathrm{MHz} \cdot 4(2-n_p) + {}^{63}C_c. \tag{2.15}$$

While the first term in both equations accounts for the effect of the on-site hole content to the EFG of the respective nuclei, the second term in Eq. (2.15) is attributed to the effect of planar O charges on the Cu EFG. The latter is modeled by an overlap of the in-plane Cu

4p orbital with the four O $2p_\sigma$ orbitals of the neighboring O sites. The constants $^{17}C_\sigma$ and $^{63}C_c$ were introduced initially to account for the differences in the quadrupole splitting of the undoped materials.

In the following, these relations were shown to hold for the hole doped $La_{2-x}Sr_xCuO_4$ but also for electron doped $Pr_{2-x}Ce_xCuO_4$ and $Nd_{2-x}Ce_xCuO_4$, where the stoichiometry directly gives the planar hole doping x, i.e., the changes of the planar hole contents Δn_p and Δn_d deduced by NMR agree with the changes of the stoichiometry $\Delta x = \Delta n_\mathrm{d} + 2\Delta n_\mathrm{p}$ [Jurkutat et al., 2014]. The factor two stems for the stoichiometry of the CuO_2 plane. Furthermore, considering the parent materials, where the one inherent hole is present in the CuO_2 plane, the modification of the quadrupole frequencies among different parent materials was shown to be already described (without any adjustable parameter) by Eq. (2.14) and (2.15) with the constraint $n_\mathrm{d} + 2n_\mathrm{p} = 1$ [Jurkutat et al., 2014]. This means that the large changes of the quadrupole splittings of the planar nuclei in the parent materials, e.g., the quadrupole frequency for planar ^{63}Cu changes from 12.2 MHz in Pr_2CuO_4 to 33.2 MHz in La_2CuO_4, is due to the differently shared inherent hole of the CuO_2 plane. Thus, the constants $^{17}C_\sigma$ and $^{63}C_c$ must be rather universal for the cuprates. It is worth to stress, that so far no parameter was fixed by NMR and that the Eq. (2.14) and (2.15) hold for hole and electron doped materials with different structures[1] and compositions.

From the asymmetry of the planar O EFG which also shows material independent relations and from the empirical linear relation of the maximal T_c with $^{17}\nu_{\mathrm{Q},\sigma}$, a lower and upper bound for $^{17}C_\sigma$ was extracted [Jurkutat et al., 2014], i.e. $0.24\ \mathrm{MHz} < {}^{17}C_\sigma < 0.5\ \mathrm{MHz}$. Since for Cu the lattice contribution should be negligibly small, $^{63}C_c$ was set to zero. From the constraint $n_\mathrm{d} + 2n_\mathrm{p} = 1$, $^{63}C_c = 0$ results in $^{17}C_\sigma = 0.39\,\mathrm{MHz}$ which is within the determined boundaries. As a consequence, Eq. (2.14) and (2.15) could be used to determine the absolute values of n_p and n_d as well as $x = n_\mathrm{d} + 2n_\mathrm{p} - 1$ for doped cuprates [Jurkutat et al., 2014].

The analysis of all available cuprate quadrupole splittings leads to a three dimensional phase diagram which is reprinted from Jurkutat et al. [2017] in Fig. 2.5. It does not use the average planar hole doping x as abscissa but shows the critical temperature T_c as a function of $2n_\mathrm{p}$ and n_d for all cuprates where data were available. In this plot the parent materials are found on the thick black line which is given by $n_\mathrm{d} + 2n_\mathrm{p} = 1$. Thus, all cuprate families have their characteristic place in the phase diagram depending on how the inherent hole of the parent material is shared. Electron and hole doping result in different paths in the $(2n_\mathrm{p}, n_\mathrm{d})$-plane, and the chemical asymmetry between both material classes is lifted. Along these paths the dome-like dependence of T_c can be recognized and according to this analysis

---

[1] While the T-structured hole doped materials posses an O above planar Cu (apex oxygen), for the electron doped materials with T'-structure this site is unoccupied.

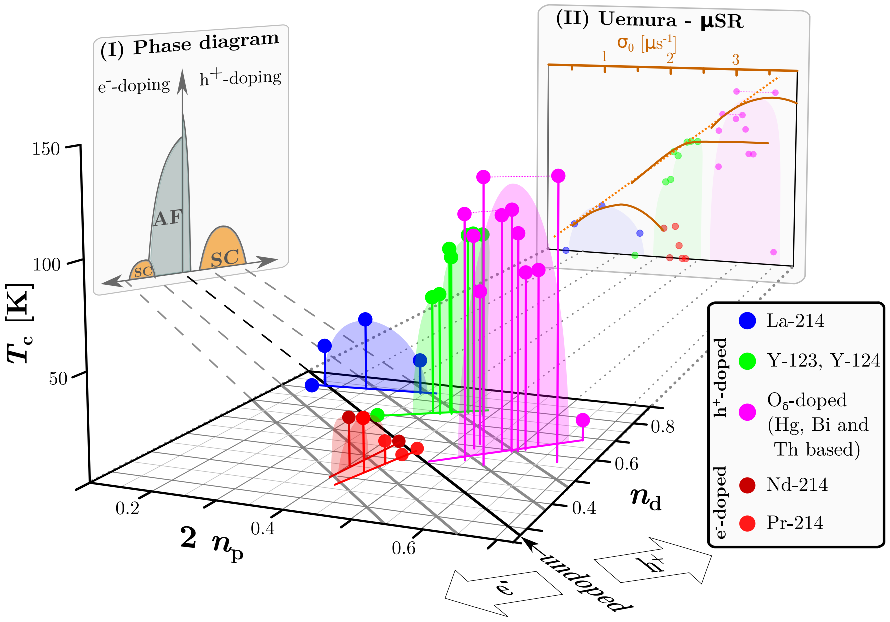

Figure 2.5: Critical temperature T_c as a function of the planar oxygen ($2n_p$) and copper (n_d) hole contents for various electron and hole doped cuprates. Due to the different sharing of the inherent hole of the parent materials, all cuprate families can be distinguished in the three dimensional phase diagram and appear to be order with increasing n_p. The classical phase diagram (x, T) appears as a projection (inset I). The solid lines are given by $x = n_d + 2n_p - 1$ with $x = 0$, ± 0.1 and ± 0.2. Reprint from Jurkutat et al. [2017].

all cuprates have their maximal T_c at $x = n_d + 2n_p - 1 \approx 0.15$. An important finding is that the materials are ordered according to their maximal T_c, i.e., the higher the O hole content n_p in the parent materials, the higher is the observed maximal T_c which is unlocked by doping the parents. The interplanar chemistry seems to determine the charge distribution between Cu and O and thereby set the maximal T_c. This can be seen more clearly on the projection $T_c(2n_p)$ shown in the Inset II of Fig. 2.5. Note that, the projection resembles the Uemura plot [Uemura et al., 1989] which establishes another correlation of the material chemistry parameter n_p and a superconducting property, i.e. the superfluid density per effective mass measured by σ_0, the muon spin relaxation rate [Rybicki et al., 2016]. The classical phase diagram (x, T) appears simply as a projection with $x = n_d + 2n_p - 1$ which is shown in Inset I of Fig. 2.5.

This new phase diagram suggests that the complex properties of the cuprates should rather be discussed in terms of n_p and n_d instead of the planar average doping x, cf. Rybicki et al. [2016]. For example, the static charge variations are known to be large ($\Delta x \approx 0.05$) within the CuO$_2$ plane [Rybicki et al., 2009; Singer et al., 2002] and the relation of planar charge ordering to other cuprate phenomena is still under discussion. With this analysis at hand, NMR is capable to distinguish spatial charge variations and ordering phenomena between Cu and O, for instance, the different charge symmetries of the CuO_4 units depicted in Fig. 2.4 (b) can be discriminated which will be useful later on. Another issue concerns the pressure dependence of T_c and its relation to pressure induced doping of the planar oxygen plane which is of importance for this thesis and it will be introduced in the next section.

2.3.3 Pressure and the planar doping level

Pressure, like temperature, is a fundamental thermodynamical variable which affects electrical, magnetic and superconducting properties and thus leads in many areas to important findings and serves as a touchstone for theory [Schilling, 1998]. In fact, the universal decrease of the superconducting transitions temperature T_c with pressure in simple metal superconductors could be attributed within the BCS framework to the decreasing pairing interaction, i.e., the increasing stiffness of lattice vibrations. For cuprates, the situation is more complex and this section will give a brief overview on pressure related effects on T_c and establishes the concept of charge transfer with pressure. A more comprehensive overview on pressure effects in conventional as well as cuprate superconductors can be found in Schilling [2007].

For cuprate superconductors the pressure response $T_c(p)$ is not unique. Most materials show an initially linear increase of T_c with pressure. However, the curves $T_c(p)$ depend strongly on the studied cuprate family, cf. Fig. 2.6 (I), and the chemical doping level cf. Fig. 2.6 (II), and exhibit maxima , i.e., $T_c(p)$ decreases for larger pressures [Mori et al., 1991; Sadewasser et al., 2000]. Note that pressure reveals the largest critical temperature of the cuprates of 164 K which was found in $HgBa_2Ca_2Cu_3O_{8+\delta}$ above 200 kbar [Gao et al., 1994].

It is not straightforward to relate the rich variety of $T_c(p)$ curves as shown in Fig. 2.6 to fundamental properties such as the pairing interaction since besides experimental issues such as nonhydrostatic strain, the complex structure can lead to additional effects. Most prominent are structural phase transitions and oxygen migration [Sadewasser et al., 2000; Schilling, 2007], but also multiple yet inequivalent CuO_2 planes [Wijngaarden et al., 1999] may hamper the analysis of $T_c(p)$.

Fortunately, these effects can be neglected for the studied samples[1] and it is believed that two contributions dominate the pressure dependence of T_c [Schilling, 2007] which are described by the following phenomenological formula:

$$\frac{dT_c}{dp} = \left(\frac{dT_c}{dx}\right)\left(\frac{dx}{dp}\right) + \left(\frac{dT_c}{dp}\right)_{\text{intrinsic}}. \tag{2.16}$$

---

[1] There is no structural phase transition known for the investigated pressure range in YBCO and the (almost) full CuO chains leave no room for oxygen migration.

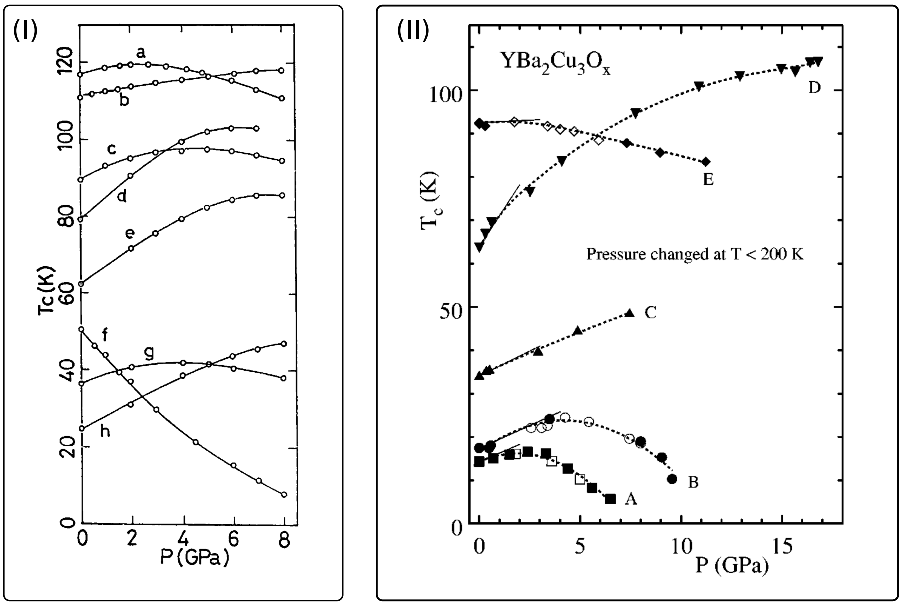

Figure 2.6: Pressure dependence of the critical temperature T_c for (I) various cuprates and (II) different dopings of $\mathrm{YBa_2Cu_3O_{6+y}}$. In (I) a: $\mathrm{Tl_2Ba_2CaCu_2O_8}$; b: $\mathrm{Bi_{1.68}Pb_{0.32}Ca_{1.85}Sr_{1.75}Cu_{2.65}O}$; c: $\mathrm{Y_{0.9}Ca_{0.1}Ba_2Cu_4O_8}$; d: $\mathrm{YBa_2Cu_4O_8}$; e: $\mathrm{CaBaLaCu_3O_{7-y}}$; f: $\mathrm{Tl_2Ba_2CuO_{6+y}}$ g: $\mathrm{La_{1.85}Sr_{0.15}CuO_4}$ h: $\mathrm{Nd_{1.3}Ce_{0.2}Sr_{0.52}CuO_4}$. In (II) A: $y = 0.41$; B: $y = 0.41$; C: $y = 0.45$; D: $y = 0.66$; E: $y = 0.95$. Reprint from Mori et al. [1991] and Sadewasser et al. [2000].

The first term on the r.h.s. accounts for the observation that pressure modifies the doping level x of the $\mathrm{CuO_2}$ plane and thereby changes T_c. Since for most investigated samples $dx/dp > 0$ [Schilling, 2007], this simple charge transfer model explains the experimental observation in many cuprates, that dT_c/dp seems to track the dome like behavior of $T_\mathrm{c}(x)$, i.e., $dT_\mathrm{c}/dp > 0$ in the underdoped region, $dT_\mathrm{c}/dp \approx 0$ at optimal doping and $dT_\mathrm{c}/dp < 0$ for overdoped materials, see for example Klotz et al. [1991]; Mori et al. [1991]; Murayama et al. [1991]. The second term of Eq. 2.16 is related to an intrinsic, i.e., not doping related pressure effect on T_c which may reflect fundamental electronic properties of the superconducting state, e.g., the pressure dependence of the pairing mechanism. The modified charge transfer model of Eq. (2.16) was used successfully to describe the pressure and doping dependence in YBCO close to optimal doping by Neumeier and Zimmermann [1993]. However, aside from this particular doping range, it is difficult to quantitatively separate intrinsic and doping related effects to T_c largely due to the unknown pressure dependence of x.

The possibility to measure the average planar doping level x as well as the charge distribution n_p and n_d with NMR, cf. Sec. 2.3.2, is a large advance in this field. High pressure NMR experiments, cf. Sec. 3.2.1, in combination with the in situ measurement of T_c, cf. Sec. 3.2.4, can yield simultaneously $x(p)$ and $T_\mathrm{c}(p)$ and may help to separate overlapping effects. More precisely, taking into account the insights from the new phase diagram, there might be a pressure component which modifies the average planar doping level $x(p)$, but also the charge distribution between Cu and O might be affected, i.e., $\Delta n_\mathrm{d}(p) = -2\Delta n_\mathrm{p}(p)$. Since it was shown that the intra-planar sharing of charges affects T_c [Jurkutat et al., 2014; Rybicki et al., 2016], the charge redistribution between planar Cu and O can be seen as another doping related effect which was not considered in the modified charge transfer model given by Eq. (2.16).

As pressure alters the planar doping level it may also affect planar charge variation, in particular, charge ordering. The next sections will give an overview of planar charge variation and ordering.

2.3.4 Spatial charge variations in the cuprates

The CuO_2 plane constitutes a universal and simple feature of the cuprates and is believed to be the crucial element for superconductivity. From NMR [Crocker et al., 2011; Hammel et al., 1990; Jurkutat et al., 2013; Singer et al., 2002], but also from other methods [Bianconi et al., 1996; Tranquada et al., 1995] it is well known that the CuO_2 plane is largely inhomogeneous regarding the doping level x. For example, one of the cleanest and simplest cuprates $HgBa_2CuO_{4+\delta}$ with a single and flat CuO_2 plane reveals a spatial variation of $\Delta x \approx 0.07$ by a nominal doping level of $x = 0.16$ [Rybicki et al., 2009]. Thus, revisiting the electronic phase diagram, different parts of the sample would locally belong to different phases. However, on the bulk scale, the material seems to behave uniquely, e.g., the transition into the superconducting state of the discussed Hg-compound is narrow ($\Delta T_\mathrm{c} = 2\,\mathrm{K}$). Furthermore, it is possible to increase disorder by co-doping of the stoichiometric material $YBa_2Cu_4O_8$ and T_c slightly increases [Williams, 2007]. Thus, one could conclude that only the bulk average value of the planar hole content is of importance and the large variations are not crucial for cuprate physics. In fact, the hole contents (x, n_p, n_d) discussed in the previous subsections are of that type.

On the other hand, it is discussed that inhomogeneities may be essential for superconductivity in the cuprates [Kivelson and Fradkin, 2007] and the occurrence of spatially ordered charge variations which are accompanied by a suppression of T_c hints to such a fundamental relation. For an overview of different methods measuring charge ordered phases including NMR see for example Kivelson et al. [2003] and more recently Comin and Damascelli [2016] as well as Grafe [2012]. Evidence for charge order has been found in various cuprates[1], but in the following the focuse will be on YBCO.

---

[1] See for example: Croft et al. [2014]; Kivelson et al. [2003] for the La-system, da Silva Neto et al. [2014]; Hoffman et al. [2002] for Bi-system , Campi et al. [2015]; Tabis et al. [2014] for Hg-system and Blanco-Canosa

Charge order as seen by x-ray is most prominent in the underdoped region [Ghiringhelli et al., 2012; Hücker et al., 2014] and since it appears in the same doping range at which superconductivity is suppressed and a dip in the upper critical field is observed, see for example Grissonnanche et al. [2014], it is assumed that charge order influences superconductivity (and vice versa). A common reasoning is the following: charge order (charge density wave) is due to a Fermi surface instability competing with superconductivity. In fact, compared to the overdoped material, quantum oscillations measure a distinctly different Fermi surface in the underdoped system [Doiron-Leyraud et al., 2007]. Also other more indirect methods observe anomalies in that particular doping range, see for example Hall measurements [LeBoeuf et al., 2007] and ultrasound [LeBoeuf et al., 2012]. In addition, it was found that magnetic fields can enhance charge order which is attributed to the suppression of superconductivity [Chang et al., 2012, 2016]. However, since the argument is rather indirect and signatures of charge order have been reported in optimally/overdoped $YBa_2Cu_3O_{6+y}$[1] as well [Pintschovius et al., 2004; Raichle et al., 2011], the relation of charge order to, for example, the superconducting pairing mechanism remains unclear and has to be investigate further. For example, the pressure response of the ordered structure has so far not been examined and magnetic field dependent measurements including different orientations of the magnetic field have not been carried out for a large doping range.

Nuclear resonance techniques are very sensitive to the local charge symmetry and do not require long coherence of order, cf. Sec. 2.2.1. Thus, NMR and NQR are ideal probes for charge ordering. However, the contribution to these fields are only minor and concerned mainly planar charge variations [Haase and Slichter, 2003; Singer et al., 2002]. The reason for this is, that besides a few exceptions, i.e., $YBa_2Cu_3O_7$ and other specially ordered phases of that material class including $YBa_2Cu_4O_8$, the quadrupolar distribution is rather big (>1 MHz) and featureless, cf. Sec. 4.1 for an overview. Since the linewidth of these “narrow” materials is strongly affected by doping [Schiefer et al., 1989; Williams, 2007] and depends on the synthesis [Zimmermann et al., 1988], the broad lines are commonly attributed to defects. Thus, they are not considered of particular importance for cuprate physics.

Surprisingly, hydrostatic pressure seems to affect the linewidth as well [Machi et al., 1995; Meissner, 2012], however, the issue was not discussed largely. Still, it indicates that also a soft mechanism could be involved in the total linewidth. In addition, the above mentioned “narrow” materials reveal a substantial O line splitting which was attributed to the orthorhombic crystal structure. However, if this interpretation fails, the splitting could

---

et al. [2014]; Ghiringhelli et al. [2012]; Hücker et al. [2014] for the Y-family, but also in electron doped materials [da Silva Neto et al., 2015].

[1] Also in other cuprate families is charge order observed in optimally doped materials [Campi et al., 2015; Tranquada et al., 1997].

also signal planar charge order of rather large amplitude [Haase and Slichter, 2003].

The investigation of the "narrow" materials must be a starting point for the study of the origin of the broad lines as well as the search of charge order. Indeed, more recently, NMR in high magnetic fields found charge ordering in ortho II structure of YBCO as a splitting of the satellite lines of planar Cu and O [Wu et al., 2011, 2013]. This observation is considerably different from prior observations since a magnetic field and temperature induced line splitting is not expected to be due to defects and should therefore signal an electronic origin. However, since NMR measures a bulk average and a phase separation may also result in a splitting, a solid prove of charge order must reflect local order.

In this thesis, the NMR and NQR linewidth is investigated to gain more information about the local charge symmetry and its spatial variation, i.e., charge ordering and the unusual broad lines. For this, overdoped $YBa_2Cu_3O_7$, underdoped $YBa_2Cu_4O_8$, as well as $YBa_2Cu_3O_{6.9}$ with a doping level close to optimal doping, were exposed to moderate stress, i.e., magnetic fields, different temperatures, and moderate pressure, which are known to affect the electronic properties but do not change crystallographic structure. Furthermore, the analysis of the local planar doping levels presented in Sec. 2.3.2 is applied to separate contribution from Cu and O.

In the next chapter, the employed experimental techniques will be described which enable NMR and NQR under pressure as well as to measure the pressure dependence of T_c in-situ. Furthermore, the investigated samples will be described.

Chapter 3

Experimental techniques and sample details

In this chapter, details of the NMR and NQR experiments will be given and important aspects of the performed measurements will be discussed. The pressure generation using a moissanite anvil cell will be presented with the focus on the preparation of the cell for single crystal measurements. The procedure of the alignment of the tiny crystallites with the external magnetic field and the insitu measurement of the critical temperature T_c will be demonstrated. Finally, the investigated samples and the performed oxygen exchange process will be presented.

3.1 Nuclear resonance experiments

This section will present the setup which was used for the NMR and NQR experiments. It will introduce the applied pulse sequences and the references used for magnetic shift measurements. Furthermore, essential parameters of the NMR/NQR resonator as well as the spectrometer will be described in the context of the performed experiments.

3.1.1 NMR experiments - Setup, Pulse sequences, Excitation

NMR setup For NMR experiments Bruker Advance III HD and Tecmag Apollo spectrometers were used in combination with a superconducting magnet generating a field of 11.7 T. The NMR coil L in which the sample was embedded was placed on a home-built probe. It was connected with a tuning (C_T) and matching (C_M) capacitor such that a simple resonator is formed as shown in Fig. 3.1. The used cryostats allow for temperature dependent measurements in the range from 400 K to liquid helium temperatures.

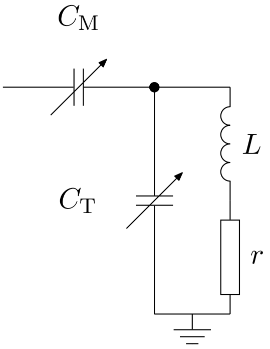

Figure 3.1: The NMR resonator consists of the NMR coil having an inductance L and losses r, the tuning capacitor C_{T} setting the resonance frequency and the matching capacitor C_{M} which couples the resonator to the spectrometer.

Powders were fixed within the NMR coil. For single crystal measurements special holders made of thermoplastics were used enabling the rotation of the sample. For pressure dependent experiments, cf. Sec. 3.2.1, the pressure cell was mounted on a two angle goniometer that was placed on the probe and enables the alignment of a small crystallite with respect to the external magnetic field.

NMR resonator The resonator illustrated in Fig. 3.1 is characterized by its resonance frequency $\omega_{\mathrm{R}} = 2\pi f_{\mathrm{R}}$ and its quality factor Q which is defined as the ratio of the stored to dissipated energy per cycle. The resonator is important for NMR since it enhances the induced voltage by $\sqrt{Q}$, limits the bandwidth $\Delta\omega = \omega_{\mathrm{R}}/Q$ and by that the accumulated noise. Since the losses of the capacitors can be neglected, the Q-factor of the resonator is determined by the Q-factor of the NMR coil Q_{coil}:

$$Q = Q_{\mathrm{coil}} = \frac{\omega_{\mathrm{R}} L}{r}. \tag{3.1}$$

Here, r denotes the losses of the NMR coil[1]. Note that Q_{coil} is an important parameter for NMR excitation and signal detection and can be determined from the bandwidth of the resonator $\Delta\omega$.

The bandwidth is defined as the difference of the frequencies at which the phase angle is ±45°. At these frequencies the reflected power from the tuned and matched circuit will be -7 dB of the input power, i.e., $\Delta\omega = \Delta\omega_{-7\mathrm{dB}}$. The resonator's Q-factor is then given by $Q = \omega_{\mathrm{R}}/\Delta\omega_{-7\mathrm{dB}}$ [Doty et al., 1988]. The obtained Q is identical to Q_{coil} for the resonator shown in Fig. 3.1. In Sec. 3.2.2, it will be shown, that additional coils hamper the determination of

---

[1] DC-losses as well as dielectric losses are captured by r.

Q_{coil} and a more advanced method has to be used.

If losses are small, i.e., $Q \gg 1$, the resonance frequency is given by

$$\omega_{\mathrm{R}} = \frac{1}{\sqrt{(C_{\mathrm{M}} + C_{\mathrm{T}})L}}. \tag{3.2}$$

While the tuning capacitor C_{T} is sufficient to tune the resonator to a desired resonance frequency, both tuning and matching capacitor C_{M} are needed to couple the resonator to the external equipment ensuring optimal power transmission:

$$Z = r \left(\frac{C_{\mathrm{T}} + C_{\mathrm{M}}}{C_{\mathrm{M}}} \right)^2 \overset{!}{=} 50\,\Omega. \tag{3.3}$$

Excitation The excitation of the spin system through the magnetic field B_1 was discussed in Sec. 2.2. The B_1-field is generated in the NMR coil and can be calculated from the coil's parameter, i.e., Q_{coil}, the coil's volume V and the power P dissipated in the NMR coil. Using the $\pi/2$-pulse condition, i.e., $\gamma B_1 t_{\pi/2} = \pi/2$, the length of a $\pi/2$-pulse can be estimated:

$$t_{\pi/2} = \sqrt{\frac{\pi^2 \omega_{\mathrm{R}} V}{2\mu_0 \gamma^2 Q P}}, \tag{3.4}$$

with the vacuum permeability μ_0. Here, various approximations have been used, e.g., a homogeneous B_1-field which is zero outside of the coil and ideal RF-components. Therefore, the estimation of $t_{\pi/2}$ can easily be off by a factor of two and the proper excitation conditions have to be found experimentally, e.g., by varying the power. However, if $t_{\pi/2}$ is found once, Eq. (3.4) predicts the pulse length for different experimental conditions, e.g., different magnetic fields, temperatures or excitation widths. Furthermore, the pulse length or power was adjusted for proper selective excitation of the different resonances of quadrupole nuclei [Man et al., 1988].

Detection width NMR spectra can be very broad and the detection width, i.e., the range of frequencies which can be detected for a given experimental setting is finite. Limitations are due to the sampling rate of the spectrometer, the resonator's bandwidth $\Delta\omega$, the shape of the pulses and the largest pulse duration t_{p} of the pulse sequence. For instance, the excitation profile of a rectangular pulse of duration t_{p} is approximately given by $\mathrm{sinc}(\omega t_{\mathrm{p}})$ with a FWHM of $\approx 1.21/t_{\mathrm{p}}$. The excitation width is set to half of the FWHM where the excitation is better than 85%, e.g., $t_{\mathrm{p}} = 0.5\,\mu\mathrm{s}$ gives a pulse excitation width of $\approx 1.2\,\mathrm{MHz}$.

Frequency stepped experiments were carried out if the detection width was too small

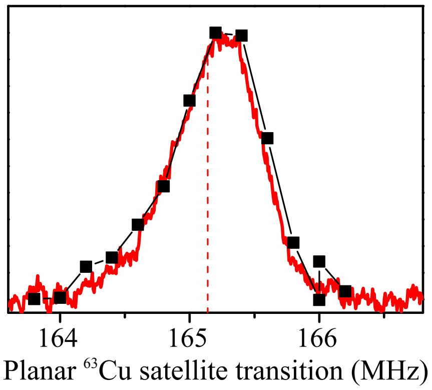

Figure 3.2: Planar ^{63}Cu satellite transition at 18 kbar and 100 K in $YBa_2Cu_3O_{6.9}$. The resonance line (FWHM ≈ 750 kHz) was measured by a broad excitation (red line, vertical dashed line indicate excitation frequency) and by frequency steps (black points).

to obtain the full spectra. If the frequency step was Δf_{step}, then the Fourier transformed signal was integrated by $\pm\Delta f_{\text{step}}/2$ around the observed frequency which maximizes the SNR without intensity double count.

NMR µ-coils possess small Q-factors of about 10-40 and narrow pulses with large excitation width are possible, cf. Sec. 3.2.1. In Fig. 3.2, a broad planar Cu satellite transition having a FWHM ≈ 750 kHz is shown which was excited with a spin echo pulse sequence with a π-pulse of 0.5 µs. The spectrometer's dwell time[1] was set to 150 ns and the bandwidth of the resonator was ≈ 6 MHz. The concurrence of the observed line with a frequency stepped experiment demonstrates the broad excitation and detection width of the µ-coil setup.

Pulse sequences For NQR measurements on Cu_2O powder and for NMR reference measurements the free induction decay experiment (FID) was used. A $\pi/2$-pulse flips the magnetization and a signal can be detected after the deadtime of the spectrometer that is due to the ring down of the RF-components after a pulse. For all NMR and NQR experiments on YBCO, the FID decays fast and the spectrometer cannot obtain a signal. The spin echo pulse sequence was then applied. Here, the initial $\pi/2$-pulse is followed by a π-pulse after a time τ which refocuses parts of the magnetization and an echo is formed after 2τ. The transversal relaxation can be tracked by varying τ in the spin echo sequence. The longitudinal relaxation is measured using the inversion recovery experiment. Varying the separation time τ_{sep} between an initial magnetization-inverting π-pulse, a spin echo reads out the magnetization. The transversal and longitudinal relaxation times can be extracted from the measured data as explained in Sec. 2.2.1. The used pulse sequences are depicted in Fig. 3.3.

---

[1] Inverse of the sampling rate

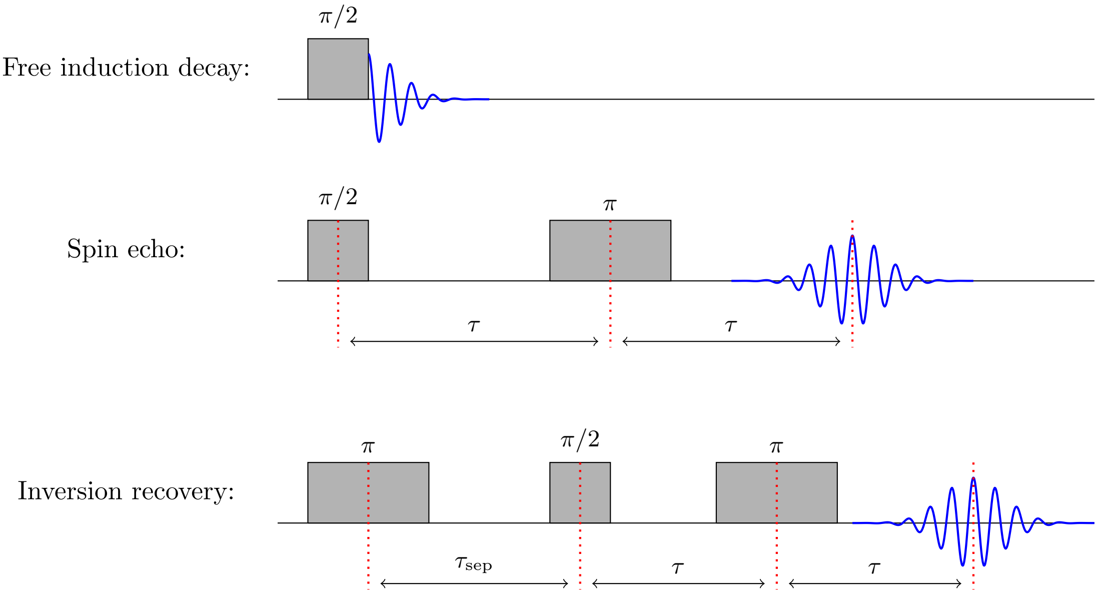

Figure 3.3: NMR pulse sequences used for this study. The free induction decay consists of a $\pi/2$-pulse which gives rise for a decaying signal. If the signal decayed faster than the dead time of the spectrometer, the spin echo pulse sequence was applied. A π-pulse follows the initial $\pi/2$-pulse after a duration τ and refocuses the transverse magnetization. An echo is obtained after 2τ. Varying τ, the decaying transversal magnetization can be obtained and T_2 can be extracted. The inversion recovery is used to track the longitudinal magnetization and T_1 can be measured. For this, a π-pulse inverts the magnetization and after a variable duration τ_{sep} the magnetization is inspected with a spin echo.

Reference For shift measurements on Cu, metallic Cu (powder in epoxy) was used as a reference having a shift of 3820 ppm [Lutz et al., 1978] which calibrates the external magnetic field:

$$\gamma B_0 = \frac{\nu_{\mathrm{ref}}}{1 + K_{\mathrm{ref}}}. \tag{3.5}$$

In the pressure cell, metallic Cu of the µ-coil was measured. Care needs to be taken since strong B_1 can lead to eddy currents in the gasket which hamper precise shift measurements. For oxygen, tap water with a shift of 0 ppm was used as a reference. In the pressure cell, the reference for O was scaled from metallic copper. For this, metallic Cu and tap water were measured in the same environment giving a ratio of ${}^{17}\gamma/{}^{63}\gamma = 0.5102462(1)$.

3.1.2 Peculiarity of NQR experiments

As described in the previous chapter, NQR is performed in zero magnetic field and no large and homogeneous magnetic fields are required. Prior to the experiment there is no magnetization, but since the nuclear quadrupole moment is coupled to the nuclear magnetic moment, transitions between the quadrupole split energy levels can be induced by an oscillating magnetic field which generates an oscillating sample magnetization, cf. Sec. 2.2.2. Therefore the standard NMR equipment, e.g., spectrometer, probe etc., can be used. For this work, Apollo spectrometers and a home-build probe which fits in a Janis cryostat have been used.

Pulse sequences introduced in the last section, cf. Fig. 3.3, are used for NQR as well, but the concept of a $\pi/2$-pulse is not adequate. Pulses disturb thermal equilibrium in such a way that a signal can be detected [Das and Hahn, 1958; Suits, 2006]. The excitation can be optimized varying the pulse length or power.

Different to NMR, both RF-field components are used to drive transitions for NQR which reduces the required power by a factor of 4 [Lee, 2002]. While for NMR the orientation of the coil axis, i.e., the axis of the linear polarized B_1-field, with respect to the external field B_0, is important for excitation and signal detection[1], for NQR the orientation of the coil axis with respect to the crystal, i.e., the principle values of the electric field gradient (EFG), is relevant. This has important consequences for experiments. For a spin $I = 3/2$ within a non-axially symmetric EFG, only components of B_1 perpendicular to the main principle axis of the EFG (Z-axis) generate magnetization and the excitation will be most efficient if B_1 is parallel to the X-axis of the EFG [Das and Hahn, 1958]. For planar Cu in $\mathrm{YBa_2Cu_3O_{6+y}}$, the crystal's c-axis needs to be perpendicular to the coil axis which is sufficiently achieved with the preparation of the pressure cell for orientation purpose, cf. Sec. 3.2.3. However, for powders this means that not all crystallites can be optimally excited. Furthermore, the signal intensity compared to a single crystal is reduced by more than a factor of two [Lee, 2002].

In this study, NQR experiments were solely made on Cu isotopes and the related NQR frequencies are much lower than for Cu NMR in a magnetic field of 11.7 T. For tuning purpose, usually the resonance frequency of the resonator is preset by a large inductance of the NQR coil, cf. Eq. (3.3). This, however, is not possible for the NMR pressure cell setup since the space for the NMR coil is limited. Therefore, in addition to the NMR coil, a large coil is used in the resonator to decrease the resonance frequency, cf. Sec. 3.2.2.

Small magnetic fields disturb the energy levels given by the crystal field which leads to erroneous NQR results. For a given setup, i.e., probe, cryostat, cables, also including the position of the equipment in the lab relative to permanent magnets, the agreement of the observed ratio of the ^{63}Cu and ^{65}Cu NQR frequencies with the corresponding ratio of quadrupole moments proves the absence of a disturbing magnetic field.

---

[1] Only components of B_1 perpendicular to B_0 can induce transitions and only components of the oscillating magnetization along the coil axis can be measured.

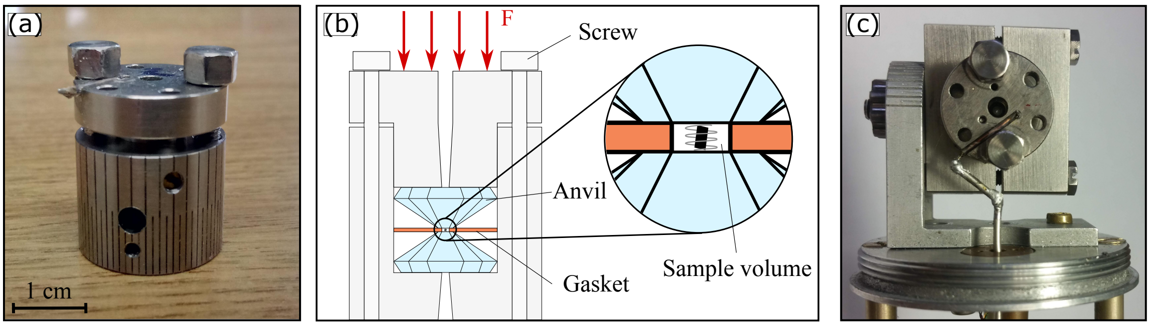

Figure 3.4: Pressure cell design and goniometer. Photograph of the pressure cell with an angle scale (a) and schematic of the pressure cell (b). Applied force F generates pressure within the sample volume enclosed by the anvils. Titanium screws maintain a stable pressure value. Enlarged sketch shows the pressurized sample volume including the NMR coil and sample. (c) Pressure cell mounted on the probe head using a two angle goniometer.

3.2 Applying pressure - NMR and the anvil cell approach

The pressure generation using moissanite anvil cells for NMR/NQR experiments with µ-coils will be presented and the tuning of the µ-coil resonator to low frequencies (10-40 MHz) will be discussed. The focus will be on the preparation of the anvil cell for single crystal measurements and their alignment with respect to the external magnetic field. Furthermore, the measurement of the critical temperature T_c within the anvil cell will be presented. The discussed methods are demonstrated exemplarily.

3.2.1 The anvil cell and the NMR µ-coil setup

There are different techniques available to generate high pressures. For an overview about NMR pressure techniques see for example Meier et al. [2015]; Meier [2016]; Meissner [2012]. Here, a short description of the setup is given and the essential points of the pressure cell preparation for single crystal measurements are discussed.

For the pressure experiments performed for this thesis, a moissanite anvil cell [Haase et al., 2009; Meier et al., 2014] was used to generate pressures up to 29 kbar. A schematic as well as a picture of the pressure cell are shown in Fig. 3.4. Two moissanite anvils with a cullet diameter of 1 mm were supported by a titanium 6-4 chassis having a comparatively high yield strength with a vanishing magnetic susceptibility. An angle scale on the chassis assisted the alignment of single crystals, cf. Sec. 3.2.3. The sample and a ruby chip were embedded in a hole within a beryllium copper (BeCu) plate serving as a gasket. The NMR coil was placed around the sample within the sample hole. Parafin oil was used as a pressure medium for hydrostatic conditions. Applying force, the anvils squeezed the sample hole and

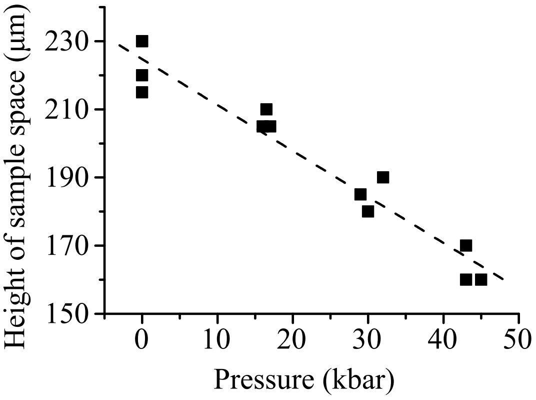

Figure 3.5: The height of the sample space as a function of the internal pressure. Gaskets were only used one-time for a pressure value. For comparison, at least three pressure values in close proximity to each other are measured.

generated pressure that was maintained by titanium screws.

The pressure was determined using the luminescence shift of the ruby R_1 line with pressure [Mao et al., 1978]:

$$p = 3808\,\mathrm{kbar}\left(\left(\frac{\lambda_p}{\lambda_0}\right)^5 - 1\right), \tag{3.6}$$

with λ_0 and λ_p the wavelength of the R_1 line at ambient conditions and under pressure, respectively.

The µ-coil is usually built from a copper wire with a diameter of about 20 µm with dimensions of the investigated sample. Typically, the µ-coil has a height of 140-160 µm and a diameter of 200 µm. The coil is placed in the sample hole, grounded by a guide pin and connected to the hot wire. A duct on the top of the cell holds the cable in place which is critical for the alignment process of single crystals, cf. Sec. 3.2.3, since it stabilizes the wiring considerably.

Clearly, the disadvantages of the µ-coil setup are the low sample volume and the inherent high DC-losses which are accompanied with a higher noise level and lower Q-factor of the resonator. However, the large filling factor of 0.5-1 gives a reasonable sensitivity. The small coil volume results in high B_1-fields per current through the coil (B_1/I_L), and thus, short pulses with a large excitation bandwidth are possible [Haase et al., 2009; Meier et al., 2014].

Pressure stability of the sample hole The gasket is a crucial part of the cell since it contains the sample as well as the NMR coil and will be deformed under pressure. For hydrostatic condition and to avoid damage to the crystal, it is essential that the sample is not touched by both anvils or the gasket itself. The pressure dependence of the gasket,

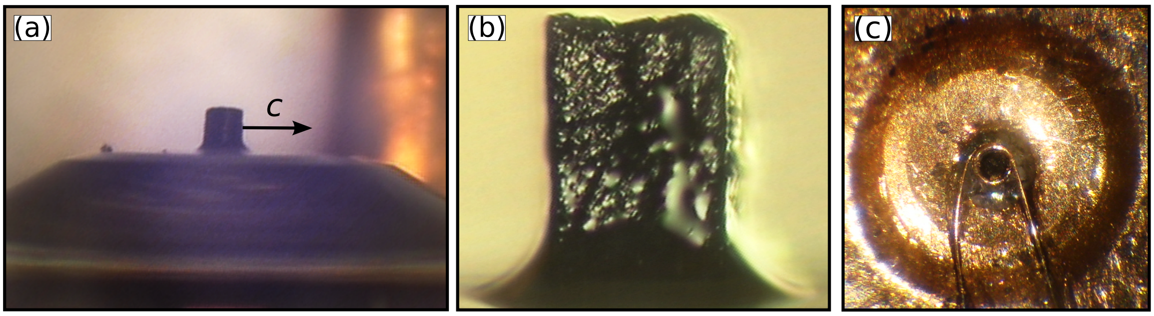

Figure 3.6: (a) Single crystal fixed on the anvil cullet with the crystal's c-axis perpendicular to the cullet face. (b) The crystal is glued on the anvil to fix its orientation. (c) NMR coil wrapped around the crystal within the sample hole of the gasket.

in particular the sample hole, is therefore of particular importance and was measured in preliminary experiments. For this, a gasket of triangular shape was cut from BeCu foil and three holes were drilled for the guide-pins supporting the gasket. After the pre-indentation to a starting height, a hole with a diameter of 0.5 mm, i.e., half of the anvil's cullet diameter, was drilled in the center of the pre-indentation. The gasket hole was then filled with ruby as well as parafin oil. The pressure cell was closed and loaded to the desired pressure. It was opened again and the height of the sample hole was measured using a micrometer[1]. Note that the gasket was not used again for another pressure point. In Fig. 3.5 the height of the sample space as a function of pressure is shown. At least three pressure values in close proximity to each other were measured for simple statistics. The initial thickness of $\gtrapprox$ 200 µm is reduced by 1.3 µm/kbar with sufficient reproducibility. The shape of the hole was only slightly deformed and does not need to be considered up to 45 kbar. The scaling sets the maximum sample and coil height, e.g., for pressures up to 29 kbar the sample and coil height must be less than 180 µm.

Fixing the crystal If powders or cubic systems are investigated, the µ-coil is placed and fixed in the sample hole of the gasket. The sample is filled into the coil afterwards. For materials with non-cubic crystal structures as the cuprates, the orientation with respect to the external magnetic field B_0 is essential. Furthermore, arbitrary rotations of the pressure cell are not possible since the coil is fixed and it's B_1-field should be at best perpendicular to B_0. Since the crystal is twinned and thus the in-plane shift and EFG components are measured simultaneously with the magnetic field within the CuO_2 plane ($c \perp B_0$), the crystallite's c-axis needs to be perpendicular to the coil axis to measure the full tensors, i.e., perpendicular

---

[1] To check uncertainties due to the drilled hole, the height was also measured using a scaled microscope with the same results.

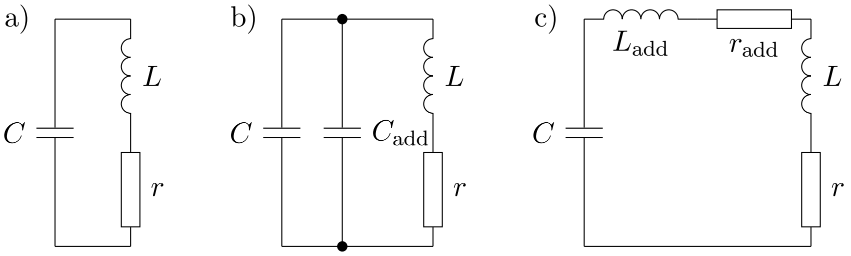

Figure 3.7: Simplified schematic of the used NMR resonator (a). For low resonance frequencies additional capacitors (b) or inductors (c) can be used. Resistors represent DC-losses as well as dielectric losses. Losses of the capacitors are neglected.

to the anvil's cullet, cf. Sec. 3.2.3 (a). The *c*-axis in $\mathrm{YBa_2Cu_3O_7}$ is found by visible reflection lines on the crystallite's *ab*-plane, cf. Fig. 3.13. The center of the sample hole is marked on the anvil and the crystal is then glued on it, cf. Fig. 3.6 (a,b). This guarantees the alignment of the crystal with a good NMR performance, i.e., $\measuredangle(B_1, B_0) \approx 90°$. In addition, it is found that the glued crystal stabilizes the alignment significantly if pressure is applied. The gasket and the µ-coil are placed and fixed afterwards, cf. Fig. 3.6 (c).

3.2.2 Additional inductor for µ-coil experiments

For feasible NMR/NQR experiments the tuning range Δf_{T} of the RF-resonator needs to be large enough to cover unavoidable changes of the resonator's capacitance or inductance, e.g., temperature dependencies. The geometry of the gasket limits the variation of the inductance of the µ-coil setup and therefore the tuning range is limited by the capacitance of the variable capacitor C of the probe with the smallest C_{min} and largest C_{max} capacitance. Due to special requirements, i.e., non-magnetic and cryogenic, the capacitance range is not arbitrary. A typical µ-coil having a diameter of 300 µm, a hight of 150 µm and 4-5 turns gives with $C \approx 1 - 20\,\mathrm{pF}$ a tuning range of 30-40 MHz at a center frequency of $\approx 130\,\mathrm{MHz}$. For a fixed NMR coil, lower frequencies are usually achieved using an additional capacitor C_{add}, cf. Fig. 3.7 (b), with the advantage that NMR excitation and signal intensity are not influenced. This approach, however, reduces Δf_{T} of the resonator considerably, cf. Tab. 3.1, and for low frequencies, e.g., NQR frequencies, it is practically zero and not suitable for experiments. An additional serial inductance L_{add}, cf. Fig. 3.7 (c), reduces the resonance frequency in the same order as C_{add} while the tuning range decreases only moderately, cf. Tab. 3.1. The added coil losses r_{add} will, however, reduce the intensity of the obtained signal and will hamper the excitation. If the Q-factor of the additional coil is larger than that of the NMR coil ($Q_{\mathrm{coil}}^{\mathrm{add}} > Q_{\mathrm{coil}}^{\mathrm{NMR}}$), the bandwidth of the resonator decreases which reduces also the excitation width. Furthermore, the modified resonator's Q-factor given in Tab. 3.1 can not

Table 3.1: Resonance frequency $f_\mathrm{R} = \omega_\mathrm{R}/2\pi$, tuning range $\Delta f_\mathrm{T} = f_\mathrm{max} - f_\mathrm{min} = \omega_\mathrm{T}/2\pi$ and Q-factor for the ordinary resonance circuit and for the resonator with an additional parallel capacitance as well as with an additional serial inductance, cf. Fig. 3.7. For simplified notation: $\Delta C_\mathrm{T} \equiv \sqrt{C_\mathrm{max}} - \sqrt{C_\mathrm{min}}$.

	ordinary setup	add capacitance	add inductance
ω_R^2	$1/LC$	$1/L(C + C_\mathrm{add})$	$1/(L + L_\mathrm{add})C$
$(\Delta\omega_\mathrm{T}/\Delta C_\mathrm{T})^2$	$1/LC_\mathrm{min}C_\mathrm{max}$	$\approx C_\mathrm{max}/LC_\mathrm{add}^3$	$1/(L + L_\mathrm{add})C_\mathrm{min}C_\mathrm{max}$
Q-factor	$\omega L/r$	$\omega L/r$	$\omega(L + L_\mathrm{add})/(r + r_\mathrm{add})$

simply be used to estimate NMR parameters with Eq. (3.4) since it does not solely represent $Q_\mathrm{coil}^\mathrm{NMR}$. Therefore, in NMR/NQR experiments additional serial coils are not used. In the µ-coil setup, however, losses r_μ and the bandwidth are comparatively high and additional coils can be advantageous if $r_\mathrm{add} \ll r_\mu$. Intensity and excitation corrections can be done with the knowledge of the loss fraction $\lambda \equiv (r_\mu + r_\mathrm{add})/r_\mu$. This fraction can be determined with the Q-factors of the setup with (Q) and without ($\tilde{Q}$) an additional coil at the desired frequency:

$$\lambda = \frac{Q}{\tilde{Q}} \cdot \frac{L_\mu + L_\mathrm{add}}{L_\mu} = \frac{Q}{\tilde{Q}} \cdot \left(\frac{f_\mathrm{R}}{\tilde{f}_\mathrm{R}}\right)^2 . \tag{3.7}$$

Tuning the resonator to an arbitrary resonance frequency f_R and adding the additional coil with fixed capacitors, the resonance frequency is changed to $\tilde{f}_\mathrm{R}$. The fraction of the obtained resonance frequencies determines the inductance fraction in Eq. (3.7). The matched resonator's B_1-field is generated by the current through the NMR coil $B_1 \propto I_\mathrm{L} = \sqrt{P/r}$ and the $\pi/2$-pulse length has to be adjusted correspondingly $t_{\pi/2} \propto B_1^{-1}$. Hence, the pulse length $\tilde{t}_{\pi/2}$ of the setup with an additional coil is increased by:

$$\tilde{t}_{\pi/2} = \sqrt{\lambda} \cdot t_{\pi/2}. \tag{3.8}$$

For the receiving case, the reduced intensity is obtained in a similar fashion:

$$\tilde{M} = 1/\sqrt{\lambda} \cdot M. \tag{3.9}$$

A large solenoid ($r = 5\,\mathrm{mm}$, $l = 6\,\mathrm{mm}$, 3 turns) and a serial resistance of $1\,\Omega$ emulated the µ-coil[1] and NQR test measurements on $^{63}\mathrm{Cu_2O}$ were performed. The scaling was tested with different additional coils having the same diameter but with 5, 10 and 20 turns which are

---

[1] Large samples can be measured in such a coil which increases the signal for test measurements.

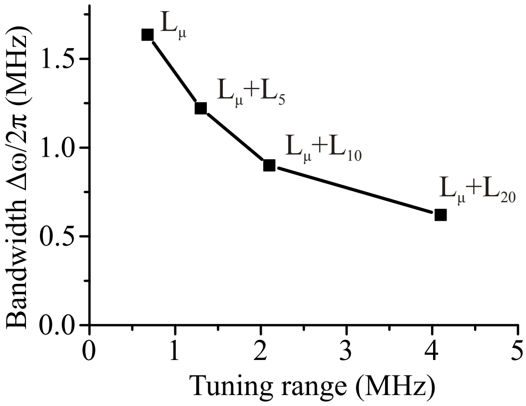

Figure 3.8: Measured bandwidth and tuning range of the emulated µ-coil resonator with different additional coils.

denoted with L_5, L_{10} and L_{20}[1], respectively. Additional capacitors were used to tune the resonance frequency to $f_{\mathrm{R}} \approx 26\,\mathrm{MHz}$. In Fig. 3.8, the obtained tuning range and bandwidth of the tuned and matched resonator are plotted. The resonator's bandwidth decreases as one adds low loss coils since the Q-factor increases (more energy is stored) which diminishes the excitation range. Less additional capacitance increases the tuning range of the setup with larger additional inductance. FID nutation experiments were performed to test the scaling behaviour. The measured as well as scaled data points are plotted in Fig. 3.9. The good scaling behaviour validate the usage of the formulas above.

To conclude, for low resonance frequencies the additional coil tunes the setup to the desired frequency with a suitable tuning range. The decreasing bandwidth is balanced by the inherent large bandwidth of the µ-coil resonator. Scaling is possible with the knowledge of $Q, \tilde{Q}$ and $f_{\mathrm{R}}, \tilde{f}_{\mathrm{R}}$. Therefore this approach is advantageous for low frequency NMR and NQR experiments with the µ-coil setup.

3.2.3 Sample alignment with the anvil cell setup

The large anisotropy of the NMR parameters of the cuprates demands precise alignment of the crystal with respect to the external magnetic field, e.g., an offset of 5° from the main principle axis of planar Cu in $\mathrm{YBa_2Cu_3O_7}$ results in an error of $\approx 350\,\mathrm{kHz}$ of the quadrupole splitting which is of the same order as modifications by pressure: $d\nu_Q/dp \approx 150\,\mathrm{kHz/GPa}$ [Müller et al., 1989]. In particular, the alignment of a single crystal within the pressure cell and to secure its stability while pressure is applied, is challenging due to sample size and

---

[1] The additional coil's diameter was 4 mm and the length of L_5, L_{10} and L_{20} were 3 mm, 5.5 mm and 12 mm, respectively.

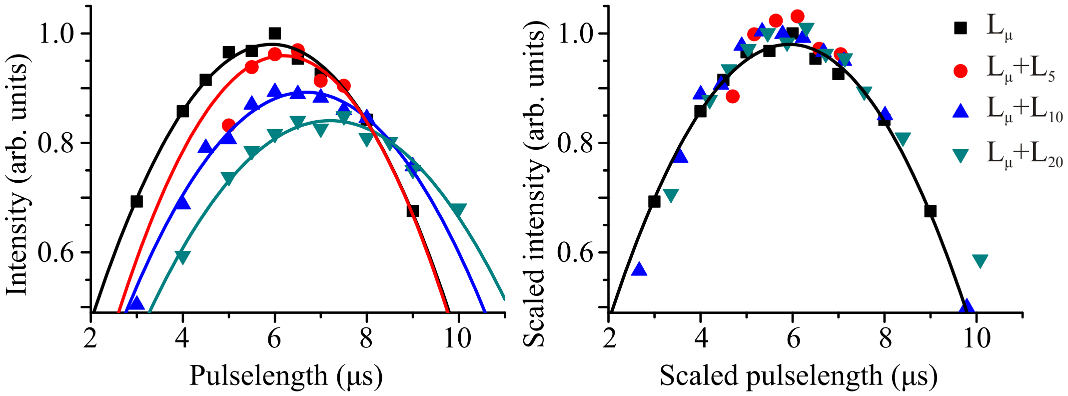

Figure 3.9: NQR FID nutation experiment of ^{63}Cu in Cu_2O with different additional coils. Raw data (left panel) and scaled data using Eq. (3.8) and (3.9) (right panel).

limited visible access. Therefore, an effective method is needed to orientate the crystal and to determine the quality of orientation and it's stability.

For this thesis, the alignment of the crystal was done using the large angular dependence of the magnetic shift and the quadrupole splitting of planar Cu and O whose principle axes coincide with the crystal axes [Pennington and Slichter, 1990], cf. the crystal structure in Fig. 2.1. The Cu satellite transitions (ST) have a much larger angular dependence than the central transition (CT), but the STs are difficult to measure in the cuprates since they are broad. On the other hand, the CT shows a significant change under rotation ($\approx 3\,\mathrm{MHz}$) and the line is narrow ($\approx 20\,\mathrm{kHz}$). The main principle values of the planar Cu shift and EFG tenors are parallel to the crystal's *c*-axis and the tenors are almost isotropic within the *ab*-plane. Therefore, the CT of planar Cu is used to find $c \parallel B_0$ and $c \perp B_0$. The shift and EFG of planar O are largest along the planar Cu-O bond direction and the ST of planar O is used to find $\sigma \parallel B_0$[1].

The planar Cu tensors are nearly axially symmetric ($\eta \approx 0$) and only β the angle between the main principle axis and B_0 is important for the orientation and as introduced in Sec. 2.2, the position of the CT is given by a sum of a magnetic and a second order quadrupole part:

$$\nu_{\mathrm{ct}}(\beta) = \nu_{\mathrm{mag}}(\beta) + \nu_q^{(2)}(\beta). \tag{3.10}$$

Using $A(\beta, \alpha, \eta_l) = (3\cos^2\beta - 1)/2 + \eta_l/2 \sin^2\beta \cos 2\alpha$ the magnetic part can be written as:

$$\nu_{\mathrm{mag}}(\beta, \alpha) = (1 + K_{\mathrm{iso}} + K_{\mathrm{ani}}\, A(\beta, \alpha, \eta_{\mathrm{m}}))\gamma B_0 \tag{3.11}$$

---

[1] The planar O CT have only a comparably small angular dependence.

Neclecting the small EFG asymmetry, the second order part of planar Cu is given by:

$$\nu_{\mathrm{q}}^{(2)}(\beta) = -\frac{3\,\nu_Q^2}{16\,\nu_{\mathrm{m}}(\beta)}\sin^2\beta(9\cos^2\beta - 1). \tag{3.12}$$

Planar O is non-axial symmetric and the azimuthal angle α is important as well. Note, that β measures the angle between the Cu-O bond and B_0 for planar O. Neglecting second order quadrupole effects ($\nu_q^{(2)}(\beta \approx 0) \approx 0.2\,\mathrm{kHz}$), the O ST can be decomposed into a magnetic and first order quadrupole part:

$$\nu_{\mathrm{sat}}(\beta,\alpha) = \nu_{\mathrm{mag}}(\beta,\alpha) + \nu_{\mathrm{q}}^{(1)}(\beta,\alpha), \tag{3.13}$$

with

$$\nu_{\mathrm{q}}^{(1)}(\beta,\alpha) = \nu_Q\,A(\beta,\alpha,\eta_{\mathrm{q}}). \tag{3.14}$$

Equation (3.10) possesses two maxima if $\nu_{\mathrm{L}} < \sqrt{5\,\nu_{\mathrm{Q}}^2/4K_{\mathrm{ani}}}$. This condition can easily be fulfilled for planar Cu in the cuprates and the maxima at $\beta = 0°$ and $\beta = 90°$ give $c \parallel B_0$ and $c \perp B_0$, respectively. The ST of planar O always has a maximum at $\beta = 0°$ reflecting $\sigma \parallel B_0$. Since the pressure dependence of K, ν_Q and η_l are assumed to be small one can use the maxima criteria to align the crystal even at high pressures.

The investigated crystals are twinned, i.e., one measures a and $b \parallel B_0$ at the same time, cf. Sec. 3.3.1, and in principle only one rotation axis perpendicular to the c-axis is needed to measure the pressure dependence of the shift and EFG tensors. Large crystals are fixed in special holders and the alignment is made by the rotation of the crystal holder around the coil axis. Crystals within the pressure cell are aligned using a two-angle goniometer shown in Fig. 3.4 (c). The first rotation is around the cell's axis that is parallel to the B_1-axis. A second rotation axis R_2 (fine alignment) is initially perpendicular to B_0 and B_1 but the rotation decreases the angle between both. This means that the second rotation needs to be small to avoid losses in NMR excitation and signal detection. For this, the crystallite's c-axis should at best be perpendicular to the main rotation axis. In preliminary experiments the crystal was loosely fixed within the µ-coil and for $c \parallel B_0$ the second rotation was 21° which further increased by ≈ 9° after pressure was applied. These large offsets reduce the signal and hence increase the measuring time. To account for both the large offsets and the instability, the crystal was glued on the anvil cullet with the c-axis at best perpendicular to the pressure cell axis, cf. Fig. 3.6 (a,b). The alignment procedure was then the following: The crystal was glued on the anvil and an unavoidable, small misalignment of the crystal with the laboratory

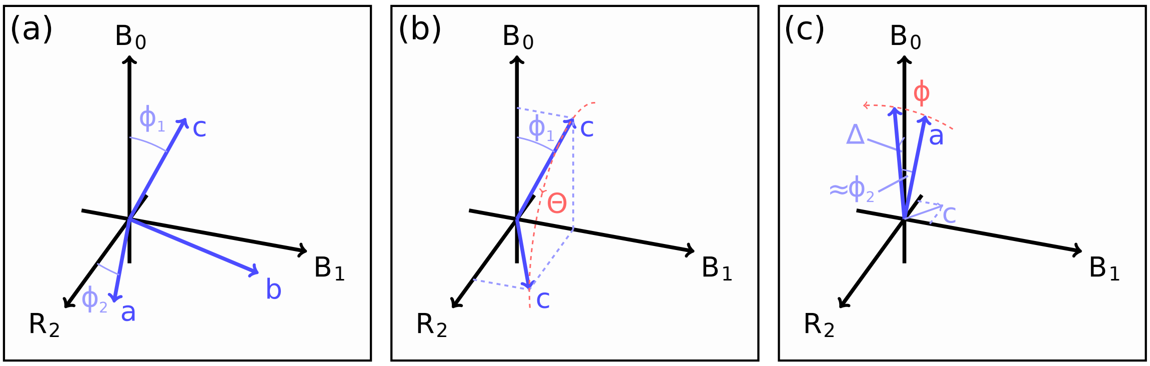

Figure 3.10: Basics of the alignment of a single crystal with unit cell axes a, b, c in the laboratory frame (R_2,B_1,B_0). Here, B_0 denotes the direction of the external magnetic field, B_1 the first rotation axis which is parallel to the NMR coil axis and R_2 the second rotation axis which is perpendicular to both B_0 and B_1. Rotations by θ about B_1 and by ϕ about R_2 ensure the alignment of the crystal axes a and c with respect to B_0. (a) The crystal is glued on the anvil, i.e., the B_0R_2-plane, and uncertainties are covered by ϕ_1 and ϕ_2. (b) The first rotation by θ gives always $c \perp B_0$, but for $c \parallel B_0$, θ must be found such that the c-axis is within the B_0B_1-plane while the second rotation by ϕ compensates for ϕ_1 (Perfect alignment for $c \parallel B_0$ is in principle possible). (c) For $a \parallel B_0$, θ is set such that $c \perp B_0$ and the second rotation is given by $\phi \approx \phi_2$. There is a principle error Δ for this orientation procedure which is negligible for small offset angles ϕ_1, ϕ_2 (see text for details).

frame is mathematically covered by small offset angles[1] ϕ_1 and ϕ_2, cf. Fig. 3.10 (a). The rough direction of the c-axis was marked on the pressure cell and set as $\theta = 0$. Rotating the pressure cell by θ about the B_1-axis[2], allows to orientate the crystal's c-axis such that $c \perp B_0$, i.e., the magnetic field lies within CuO_2 plane. For $c \parallel B_0$ the cell was first rotated as close to the B_0-axis as possible, cf. Fig. 3.10 (b), which is revealed by a maximum of the position of the ^{63}Cu CT. The second rotation by ϕ then compensates the small tilt angle ϕ_1 revealed by another maximum in position of the ^{63}Cu CT which corresponds to $c \parallel B_0$. For $ab \parallel B_0$, one could proceed in the same manner just with the ^{17}O ST. However, depending on the abundance of ^{17}O after the oxygen exchange, cf. Sec. 3.3.2, this can be time consuming (one point requires at least 2 hours). For small offset angles ϕ_1 and ϕ_2, one can avoid ^{17}O measurements for the first rotation and take a loss in accuracy by Δ starting at $c \perp B_0$. The fine alignment compensates a small tilt angle $\approx \phi_2$ given by a maximum of the position of the ^{17}O ST, cf. Fig. 3.10 (c). The principle error of the method can be estimated by $\Delta = (1 + \sin^2\phi_2 \tan^2\phi_1)^{-1/2}$. Exemplary, in Fig. 3.11 the alignment of a single crystal of $YBa_2Cu_3O_{6.9}$ at ambient pressure is shown. The measured orientation dependence of $^{63}\nu_{ct}$

---

[1] Two offset angles are needed to cover the general case which was mathematical generated as follows: Beginning with the crystal frame parallel to the lab frame, the crystal frame was first rotated by ϕ_2 around B_0-axis and then by ϕ_1 around R_2-axis.

[2] α, β are not used since the rotation is not along the principle axis of the shift and EFG tensors.

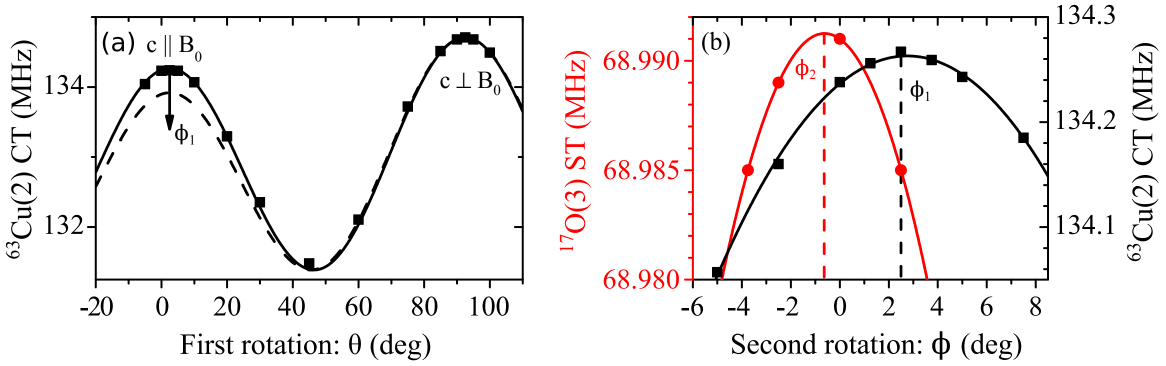

Figure 3.11: Alignment of the crystal via NMR using a two angle goniometer. (a) ^{63}Cu CT as a function of the first rotation angle θ (rotation around B_1) exhibits two maxima. While one rotation ensures always $c \perp B_0$, only if $c \perp B_1$, the alignment $c \parallel B_0$ is possible (solid line). An offset $\phi_1 = 10°$ is shown by the dashed line demonstrating the good pre-orientation of the crystal. (b) Fine alignment using a second rotation axis which is perpendicular to B_0 and B_1. For $c \parallel B_0$, another maximum appears for ^{63}Cu CT at ϕ_1 (black). Starting at $c \perp B_0$, the maximum in the ST of O(3) at ϕ_2 is used to find $ab \parallel B_0$ (red). The solid lines in (b) are parabolic fits.

reveals two maxima near 0° and 90°, cf. Fig. 3.11 (a). The solid line represents Eq. (3.10) assuming perfect pre-alignment on the anvil, i.e., $\phi_1 = \phi_2 = 0$ ($c \perp B_1$), whereas the dashed line includes a tilt angle of the crystal of $\phi_1 = 10°$. This demonstrates the excellent pre-alignment of the glued crystal within the pressure cell. The rotation about the first rotation axis by θ gives $c \perp B_0$ (here θ=92.5°), but the second rotation by ϕ needs to compensate an offset angle to reach $c \parallel B_0$. Figure 3.11 (b) (black squares) shows the second rotation for $c \parallel B_0$ at θ=2.5° which increases the position of the CT by 30 kHz (ΔK=0.023%) and the maximum is located at ϕ_1=2.5°. For $ab \parallel B_0$, the second rotation starts at $c \perp B_0$ and compensates another offset angle, this time by measuring the ST of O(3). The orientation dependence in Fig. 3.11 (b) (red points) shows a maximum at $\phi_2 \approx -0.6°$. The principle error of the method is $\Delta \approx 0.03°$ which is much smaller than the error of the manual rotation of about 1°. Applying pressure, the crystal only slightly changes the orientation ($\approx$ 2.5°) which demonstrates that the glued crystal is stable. The principle error can be neglected ($\Delta \ll 1°$) and the error in rotation ($\approx$ 1°) contributes to the errors of the NMR parameters.

3.2.4 Insitu measurement of T_c

It was shown in Sec. 2.3 that the critical temperature T_c is strongly influenced by doping but also by the application of pressure. Clearly, for the separation of both, T_c and the local doping need to be measured at the same pressure. Furthermore, measuring T_c gives information about the sample quality and doping level at ambient conditions and high pressures. On the other hand, if the pressure dependence of T_c is known from literature, the insitu measurement of T_c can also pose an independent pressure gauge. The self-resonance method based on the sharp change of the resonator's resonance frequency at T_c is a simple and practical tool for the determination of T_c within the pressure cell. The method was also successfully used by other groups [Kitagawa et al., 2009; Machi et al., 1998; Nakano et al., 2011].

The transition to the superconducting phase is accompanied with a sharp change of the real part of the magnetic susceptibility $\chi'(T)$ of the sample. This will influence the inductance L of the NMR coil according to $L \approx L_0(1 + \rho\chi'(T))$, with the inductance of the empty coil L_0. The factor ρ is crucial for the sensitivity of the method and captures the effective volume due to the filling factor of the coil as well as the penetration depth of the RF-field which is anisotropic in the cuprates. Measuring the resonator's resonance frequency f_R, the temperature dependence of the susceptibility $\chi'(T) \propto f_\mathrm{R}^{-2}$ is tracked, cf. Eq. (3.3). The actual curve of $f_\mathrm{R}^{-2}(T)$ depends on the sample and details of the resonator. However, from the drop in $f_\mathrm{R}^{-2}(T)$, the critical temperature can be determined and the transition width ΔT_c can be estimated.

The measuring procedure was the following: Mounted on a home-built probe within a Janis cryostat, the pressure cell was cooled down close to the expected critical temperature. The resonator was tuned and matched and for comparison the same initial resonance frequency was used for a given pressure series. Using a Hameg spectrum analyzer, the resonance curve was obtained and a defined temperature sweep was programmed using a Lakeshore 332. A python program was used for automatization of the measurement which extracts from the obtained resonance curve the resonance frequency f_R and the width of resonance line Δf. The program displays and saves the most relevant data, e.g., temperature, temperature drift, resonance frequency and the width of the resonance line.

In Fig. 3.12 the procedure to obtain T_c and ΔT_c is illustrated exemplary for $\mathrm{YBa_2Cu_3O_{6.9}}$ at ambient pressure. The critical temperature was extracted from the intersection of the linear parts of $f_\mathrm{R}^{-2}(T)$. The transition width ΔT_c was defined as the difference between the two intersection temperatures T_c and T_0, cf. Fig. 3.12 (a). For NMR, especially in the pressure cell, the temperature sensor cannot be placed on the sample and hence the measured temperature can be slightly different to the actual sample temperature. The effect depends crucially on the heat capacity of the system and the temperature sweep rate. In Fig. 3.12 (b), the cooling and heating curves with a rate of 0.3 K/min are shown and a difference in T_c of 0.5 K is obtained. In this case, the mean value is taken for T_c and the deviation contributes to the error. For 18 kbar, the rate was decreased to 0.2 K/min and the obtained difference was only 0.1 K. In general, the error of T_c was set to 10% of ΔT_c or given by the deviation in cooling and heating. The method was also successfully used within the magnet and reveals

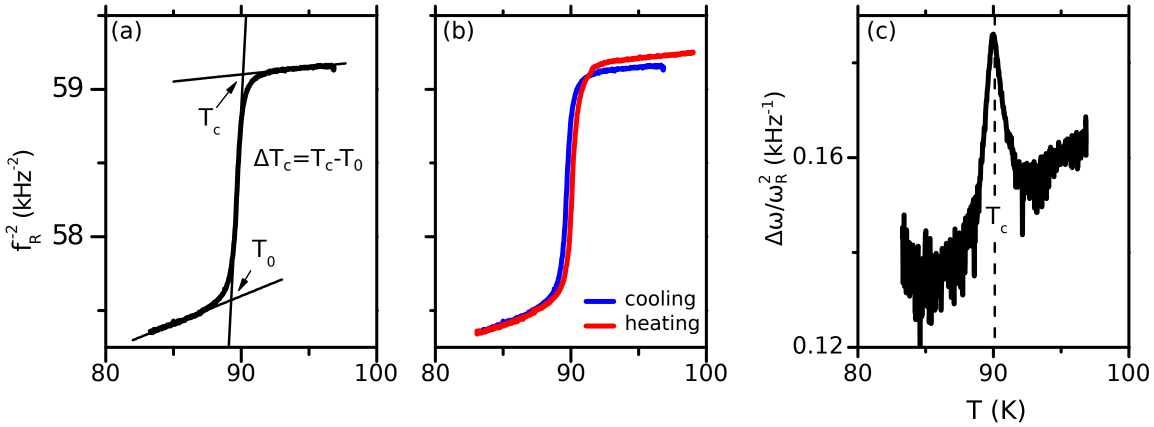

Figure 3.12: (a) Temperature dependence of f_{R}^{-2} reveals a distinct drop ($\Delta f_{\mathrm{R}} \approx 2\,\mathrm{MHz}$). From the intersections of the linear parts of the curve, T_{c} and the transition width ΔT_{c} are extracted. (b) For non-equilibrium measurements (sweep rate here 0.3 K/min) the cooling and heating curves can be different. (c) Temperature dependence of the ratio $(\Delta\omega/\omega_{\mathrm{R}}^2) \propto r$ reveals a pronounced peak in the vicinity of T_{c}. Data are from $\mathrm{YBa_2Cu_3O_{6.9}}$ at ambient pressure.

the field dependence of T_{c}.

Besides the real part of the susceptibility χ' representing the screening of the sample, ac-susceptibility measurements have also access to the imaginary part χ'' as a measure for dissipation. An analogous to χ'' can be found by the ratio $(\Delta\omega/\omega_{\mathrm{R}}^2) = (C_{\mathrm{T}} + C_{\mathrm{M}})r$ which is independent of L and represents solely dissipation. In Fig. 3.12 (c), the temperature dependence of the ratio is shown which exhibits a peak close to T_{c} typically observed in $\chi''(T)$ in cuprates due to dissipative vortex motion. Whether this method can be used to measure properties of the superconducting state such as the critical current density is beyond the scope of this thesis.

3.3 Samples

In this section, the investigated samples with their characteristics will be presented. An overview of the ^{17}O exchange process in $\mathrm{YBa_2Cu_3O_{6+y}}$ will be given and different exchange attemps will be discussed.

3.3.1 Details of the investigated samples

In this thesis, three different cuprates of the Y-family were investigated which are listed with their characteristics in Tab. 3.2. The critical temperature T_{c} scales with the oxygen content y. However, close to optimally doping (y_{opt}=0.92) where $T_{\mathrm{c}}(y)$ possesses a maximum, the pressure dependence dT_c/dp is needed to decide whether the material is underdoped or overdoped, i.e., dT_c/dp is positive below and negative above y_{opt} [Neumeier and Zimmermann, 1993]. The transition width ΔT_c gives information about strain and whether the material is single phase. The striven experiments of this thesis are only reasonable with materials having narrow lines, a property found for the stoichiometric compounds $YBa_2Cu_3O_7$ and $YBa_2Cu_4O_8$ as well as for some ordered phases[1]. Deviation from the particular oxygen content leads to tremendous increase of the planar Cu quadrupole linewidth Λ_Q [Schiefer et al., 1989; Zimmermann et al., 1988] which can also be used as a sample characteristic. Single crystal micro-samples (µS) of $YBa_2Cu_3O_7$ with a size of $\approx 0.15\times0.1\times0.1\,\text{mm}^3$ for NMR pressure experiments, cf. Fig. 3.13 (a), and large samples (LS) with a size of $\approx 2\times2\times0.7\,\text{mm}^3$ for ordinary NMR experiments were provided to our group by Prof. Dr. Andreas Erb from the Walther-Meißner-Institute for Low Temperature Research in Munich, Germany. The preparation of the samples is described elsewhere [Erb et al., 1996]. For oxygen NMR, the highly abundant isotope ^{16}O which does not posses a nuclear spin has to be exchanged by the NMR active isotope ^{17}O. Samples of $YBa_2Cu_3O_7$ were used for the oxygen exchange and it turned out that it is difficult to obtain the fully doped material ($y = 1$). For details see Sec. 3.3.2. From the doping dependence of T_c [Conder, 2001; Liang et al., 2006] and the positive pressure dependence [Neumeier and Zimmermann, 1993; Schilling, 2007], the oxygen content of the investigated sample was set to $y = 0.9$.

Table 3.2: Investigated samples and their characteristics. The quadrupolar linewidth $^{63}\Lambda_Q$ (FWHM) was measured at room temperature using NQR. The oxygen content y of $YBa_2Cu_3O_{6.9}$ was determined by T_c and dT_c/dp.

	T_c (K)	ΔT_c (K)	dT_c/dp (K/kbar)	$^{63}\Lambda_Q$ (kHz)
$YBa_2Cu_3O_7$	88	1	-0.1	115
$YBa_2Cu_3O_{6.9}$	90.3	1	0.2	300
$YBa_2Cu_4O_8$	81	4	0.5	240

The used single crystals are twinned, i.e., while the crystallite c-axis is well defined, the a and b-axis alternate over the whole crystal with a period of 1-3 µm. Twinning lines occur as angle bisectors due to tensions at the boundaries, cf. inset of Fig. 3.13 (b). These lines can be observed with the unaided eye but are more pronounced using a polarization filter, cf. Fig. 3.13 (b), and help to identify the crystal's c-axis. The alternating phases are homogeneously distributed even for the micro samples which are represented by a square

---

[1] The so called ortho-phases of $YBa_2Cu_3O_{6+y}$, i.e., underdoped materials which consist of alternating phases with full and empty chains.

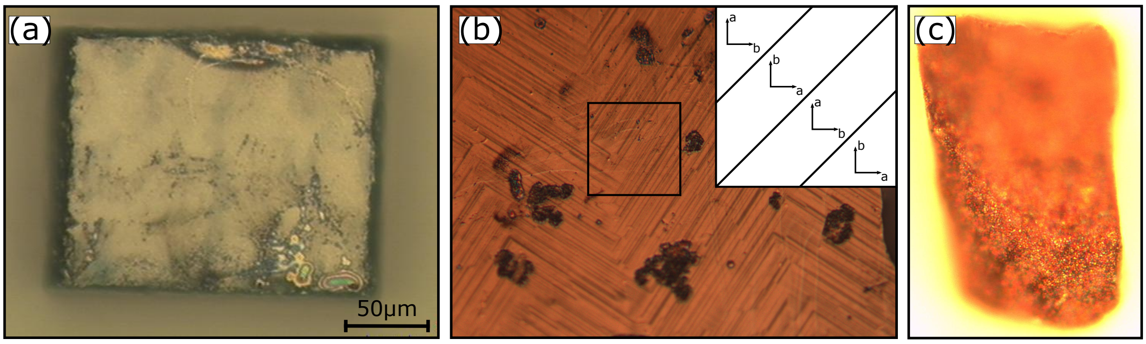

Figure 3.13: (a) Micro sample of $YBa_2Cu_3O_7$ for NMR in the pressure cell. (b) Photograph of the twinning lines which occur at the twin boundaries on the *ab*-plane using a polarization filter. The inset is a pictogram of the twinning lines (thick lines) and the corresponding orientation of the alternating crystal axes. A square of 150 µm in the main panel illustrates the micro sample dimensions. (c) Tempering the crystal at temperatures >600°C turns the crystal surface from shiny to dull and no twining is visible.

of 150 µm in Fig. 3.13 (b). Uniaxial pressure at hight temperature is needed to detwin the crystal - a thermodynamically unstable phase.

Powder pellets of $YBa_2Cu_4O_8$ were provided by G.V.M. Williams from Victoria University of Wellington, New Zealand. Details of the preparation can be found in Williams [2007]. It was found that the Q-factor of the resonator was drastically reduced if the pellet was inserted into the resonator's coil. The ground pellet did not lead to a decreasing Q and was therefore used for NQR experiments.

3.3.2 Oxygen exchange

^{17}O enriched cuprates can be obtained either by using enriched starting materials for the preparation of the samples or by ^{17}O exchange of the prepared samples on the basis of a ^{17}O gradient. In case of $YBa_2Cu_3O_{6+y}$, the former is not efficient due to the high losses of the expensive ^{17}O isotope during the thermal treatment. Therefore, the provided single crystals of $YBa_2Cu_3O_7$ were exchanged placing them in an oxygen atmosphere with partial pressure p_{O_2} at a temperature T.

While the doping level of other cuprates were set by substitution of elements, e.g., La is substituted by Sr in $La_{2-x}Sr_xCuO_4$, in $YBa_2Cu_3O_{6+y}$ the oxygen content y of the CuO_y chains controls the doping level. Clearly, a thermal treatment of the sample is necessary for the ^{17}O exchange to overcome the activation energy of different crystallographic oxygen sites, but it also changes y as can be seen in Fig. 3.14. Based on the fundamental equation of chemical reactions, a vacancy model describes $y(T, p_{O_2})$ in equilibrium [Conder, 2001].

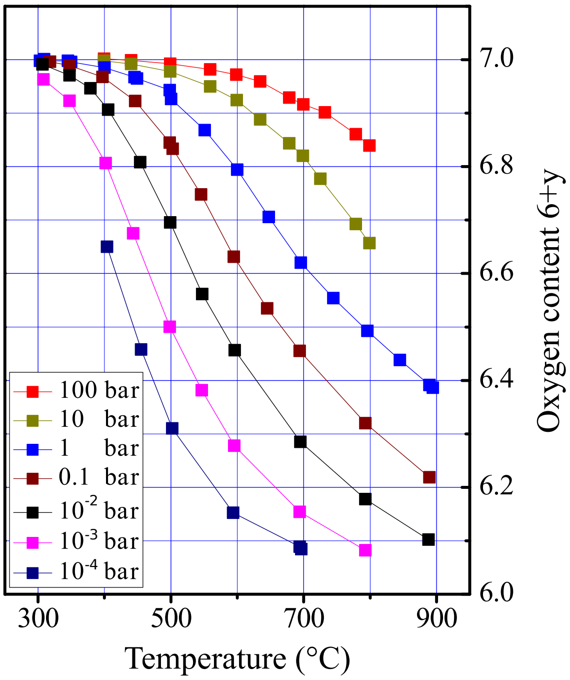

Figure 3.14: Equilibrium oxygen content $6{+}y$ of $YBa_2Cu_3O_{6+y}$ as a function of temperature and oxygen partial pressure. Data reproduced from [Erb, 1999].

For 300 °C at 1 bar, the oxygen content is close to $y = 1$. However, the exchange is not effective due to the slow diffusion of ^{17}O within the solid (tracer diffusion). Therefore, the procedure for a fully doped material ($y \approx 1$) is to exchange ^{17}O at temperatures of 500-700 °C (annealing) to increase the diffusion, followed by a stepwise cooling period (quasi-equilibrium) to 300 °C. High oxygen pressure (100 bar) would be desirable, but cannot be achieved due to the amount of ^{17}O needed. Tempering temperature, time as well as the molar ratio of ^{17}O to ^{16}O which are present in the exchange system, control the amount of ^{17}O within the sample. The duration of the cooling period sets y as well as the oxygen homogeneity of the sample.

For a sufficient high amount of ^{17}O in the sample, enough enriched gas must be provided. From the ideal gas equation and the number of oxygen atoms in the sample having a volume V_{sample}, the corresponding oxygen gas volume V_{O_2} can be estimated:

$$V_{O_2} = \frac{7N_A\rho k_B T}{2M p_{O_2}} V_{\text{sample}}, \tag{3.15}$$

with the mass density ρ and the molar mass M of $YBa_2Cu_3O_7$. The formula does neither take into account the amount of ^{17}O in the enriched oxygen gas which is used for the exchange, nor the statistic nature of the process, i.e., using Eq. (3.15) at best 50% of the oxygen sites are occupied by ^{17}O isotopes. Therefore, either the actual gas volume should be larger than V_{O_2}, or p_{O_2} should be larger than assumed in Eq. (3.15). The actual amount of planar ^{17}O (n_O) can roughly be estimated by comparing the signal intensities ^{63}S and ^{17}S of the central transitions[1] of planar ^{63}Cu and ^{17}O, respectively, at the same temperature and in the same magnetic field:

$$n_O = n_{Cu} \frac{^{63}A\,{}^{63}s\,({}^{63}\gamma)^2}{^{17}A\,{}^{17}s\,({}^{17}\gamma)^2} \left(\frac{^{17}S}{^{63}S}\right), \tag{3.16}$$

---

[1] Scaled by the respective number of scans, Q-factor and T_2.

with the number of sites per unit cell s and the line intensity scaling A due to selective excitation [Man et al., 1988].

It is well known that water and CO_2 can be incorporated in the YBCO lattice affecting the material properties strongly, e.g., incorporation of CO_2 decreases T_c [Conder, 2001]. Also residues in the exchange system, e.g., pump oil, can degrade the material's quality which could result in a dull surface in contrast to a shiny surface observed for a homogeneous and clean crystal.

Although the oxygen exchange process is well understood and successfully used by other groups [Conder, 2001; Erb et al., 1996; Schleger et al., 1991], it turned out that it is challenging to achieve a homogeneous sample close to $y = 1$ *and* a high ^{17}O content in our setup. Various attempts have been made which are listed in Tab. 3.4 and labeled from OE1 to OE10. The samples were characterized afterwards using different criteria. The critical temperature T_c was measured since it is influenced by the oxygen content and the incorporation of molecules. Also the quadrupole frequencies ν_Q of planar Cu and O are set by y. The surface conditions are markers for contamination and the planar Cu quadrupole distribution $^{63}\Lambda_\mathrm{Q}$ can give information about the homogeneity. The obtained characteristics of attempts OE1 to OE10 are given in Tab. 3.3.

Parameters for the exchange process, i.e., tempering temperature, tempering time and cooling rate, were obtained by private communications[1]. The first four sets (OE1-OE4) are similar and show that independent of the size of the crystallites and the cooling rate, ^{17}O could be incorporated. However, T_c and ν_Q of planar Cu and O indicate an oxygen content of $y = 0.6$. Due to the dull surface contamination is likely. Subsequently, the oven's temperature and temperature gradient were tested as well as the tightness of the exchange system. The first successful attempt giving the desired oxygen content and sample quality was OE5 using a much smaller tempering temperature and a cooling process which takes one month. For this, the sample and ^{16}O gas were sealed within a tube of quartz glass. The identical process with ^{17}O (OE6) was again successful regarding the sample quality, but the abundance of planar ^{17}O was quite low (0.5%). However, a defect sample remains bad even under the new conditions of OE6 which implies that not the oxygen content was wrong but the sample was contaminated. Furthermore, in attempt OE7, it was ruled out that the success of OE5 is solely due to the sealing within a quartz tube. And with OE8/9, it was shown that the tempering temperature can be increased, but a slow cooling rate is needed for a homogeneous material as can be seen by $^{63}\Lambda_\mathrm{Q}$. The samples obtained from OE10 which is a combination of OE1 and OE5, possess sufficient amount of planar ^{17}O ($\approx 25\%$). As mentioned before,

---

[1] Prof. Dr. Andreas Erb works successfully with the conditions of OE1 and from Dr. Ruixing Liang, University of British Columbia are the conditions of OE5.

Table 3.3: Sample characteristics of the different oxygen exchange attempts listed in Tab. 3.4. The critical temperature T_c, the planar ^{63}Cu quadrupole distribution $^{63}\Lambda_Q$ and the surface condition were used to characterize the samples. Listed is also whether planar ^{17}O was observed (obs.), and, if measured, the quadrupole splittings $^{17}\nu_{Q,c}$ of O(2) and O(3) in $c \parallel B_0$ (in square brackets). The '-' sign indicates not measured.

no	$T_c(K)$	$^{63}\Lambda_Q$ (kHz)	surface	^{17}O(2,3) obs.? [$^{17}\nu_{Q,c}$ (MHz)]	notes
OE1	-	> 1000	dull	yes [-]	
OE2	-	> 1000	dull	yes [0.347/not obs.]	
OE3	≈ 60	-	dull	yes [-]	
OE4	≈ 60	-	dull	-	
OE5	≈ 90(µS)	160	shiny	-	LS dull
OE6	≈ 90	190	shiny	yes [0.381/0.365]	twinning visible; ^{17}O abu.$\approx 0.5\%$; 60 K samples remain bad
OE7	64	-	dull	-	
OE8	93	no signal	shiny	-	no twinning
OE9	92	> 400	shiny	-	no twinning
OE10	90.3	300	shiny	yes [0.383/0.365]	no twinning

the oxygen content of that sample ($y = 0.9$) was estimated from T_c and the positive slope of $T_c(p)$. From NMR, the samples show the expected parameter from literature, i.e., shift, quadrupole splitting and linewidth correspond to a sample close to optimal doping.

To conclude, it was possible to exchange ^{17}O in single crystals of YBCO with a doping level close to optimal doping. From the comparison of the different attempts, it is suspected that for temperature > 600 °C molecules are incorporated which degrade the sample quality and that a slow cooling process (> 1 month) is needed to obtain a homogeneous system as seen by NMR.

Table 3.4: Process protocol of different oxygen exchange attempts. Large samples (LS) and/or micro-samples (µS) were washed with isopropanol (Iso) in some cases and sealed in a tube of quartz glass. The sample space was evacuated at room temperature, then filled with $^{16/17}$O gas and in some cases the tube was sealed by the glassblower. The samples were tempered for oxygen exchange and slowly cooled down to achieve the desired doping level. Temperatures T, durations t and ramp rates are given in °C, h and °C/h, respectively. The sample characteristics after the oxygen exchange attempts are listed in Tab. 3.3.

no.	samples	process				
		$^{16/17}$O gas pressure / remarks	tempering at T for [t]	ramp to T with [rate]	hold at T for [t]	ramp to RT with rate
OE1	1×LS	1 bar ^{17}O	650 [70]	300 [2.1]	300 [48]	50
OE2	tempering LS(16.01.)	1 bar ^{17}O	500 [1]	300 [0.6]	300 [1]	50
OE3	3×µS	1 bar ^{17}O	650 [64]	300 [1.8]	300 [27]	16
OE4	1×LS; 3×µS; 1×µS (06.06.)	1 bar ^{17}O	650 [96]	300 [0.42]	300 [72]	16
OE5	1×LS; 1×µS	Iso; 1 bar ^{16}O; glass tube sealed	510 [168]	360 [0.2]	360 [24]	14
OE6	6×µS; 3×µS ($T_c \approx 60$K)	Iso; 3 bar ^{17}O; glass tube sealed	−‖−			
OE7	1×LS	Iso; 1.1 bar ^{17}O; glass tube sealed	650 [72]	300 [2.1]	300 [48]	15
OE8	1×µS	Iso; 1 bar ^{16}O	510 [72]	300 [2.1]	300 [72]	15
OE9	1×µS	Iso; 1 bar ^{16}O	600 [72]	350 [1.5]	350 [72]	19
OE10	6×µS	Iso; 2.2 bar ^{17}O gas, glass tube sealed	tempering at 600 °C for 72 h; ramp to 510 °C with 0.4 °C/h; hold at 510 °C for 168 h; ramp to 410 °C with 0.2 °C/h; ramp to 350 °C with 0.1 °C/h; ramp to RT with 10 °C/h[a]			

---

[a] The process took 65 days. At the end of the first run it started unintentionally again and the temperature was too large to remove the samples. Therefore, a full second run was performed. However, with a failure of the furnace which stops heating at the ramp to 350 °C at a temperature of < 380 °C.

Chapter 4

Pressure and magnetic field induced variations of the planar hole contents

The complex electronics of the cuprates is still not well understood and the issue of electronic inhomogeneities are essential for the understanding of experiments and theory. Most cuprates reveal broad quadrupolar lines which are commonly believed to be due to chemical disorder, e.g., by impurities. Since the linewidths are in no clear relation to, for instance, the critical temperature T_c, it is often assumed that they are not essential for theory. On the other hand, there is evidence that also low energy perturbation as temperature, pressure and magnetic fields can affect the electric field gradient in these materials. In particular, the observation that a magnetic field can alter the quadrupolar lineshape [Wu et al., 2011, 2013] shows that the broad quadrupolar lines might be of importance for the understanding of the cuprates.

In this chapter, typical planar Cu and O spectra of the cuprates collected from literature will be presented and the most striking features will be mentioned. The variation of the planar Cu and O charge in the cuprates is estimated using the approach introduced in Sec. 2.3.2. Furthermore, the planar Cu EFG, especially its spatial variation, was investigated for this thesis in comparably homogeneous systems by applying pressure and magnetic field. The corresponding experimental results on planar Cu will be presented and discussed.

4.1 Quadrupolar linewidth in the cuprates as from planar charge variations

NMR of planar Cu and O measure the local electronic properties of the respective nuclei and the corresponding spectra represent a histogram of the Cu and O nuclei in the CuO_2 plane.

While the mean value (first moment) of the different transitions is used to quantify the shift **K** and the electric field gradient (EFG) tensor **V**, the linewidth and shape of the different transitions give information about the spatial distribution of the respective properties.

In Fig. 4.1 (left panel), planar Cu NMR satellite transitions as well as NQR lines are shown for various cuprates. The average value of the quadrupolar splitting in the depicted spectra vary over a large range and are determined by the different planar Cu and O average hole contents, cf. Sec. 2.3.2. However, most of the cuprates reveal broad quadrupolar lines, e.g., in $La_{2-x}Sr_xCuO_4$ the satellite linewidth is typically 2 MHz. Thus, the EFG varies across the CuO_2 plane which is suspected to be due to the variation of the planar hole contents. The length scale of this variation is unclear, but a macroscopic unbalance of charges in that sense that only parts of the sample become superconducting at T_c can be excluded, since no changes in the lineshape are observed [Zimmermann et al., 1989].

There are only a few exceptions which show narrow quadrupolar lines, i.e., specially ordered phases in $YBa_2Cu_3O_{6+y}$ including the fully doped material ($y = 7$), as well as $YBa_2Cu_4O_8$, reveal a quadrupolar distribution which is about one order of magnitude smaller compared to other cuprates. These systems are viewed as chemically clean systems and since

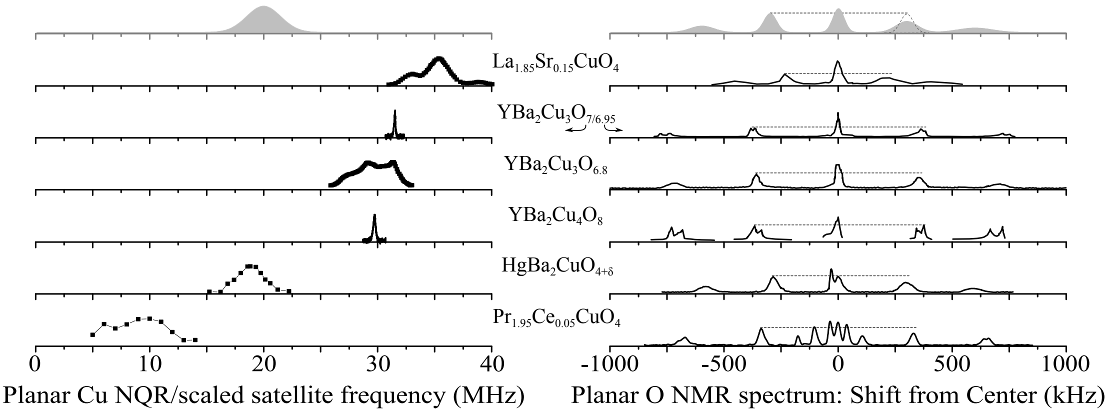

Figure 4.1: NMR and NQR linewidths of planar ^{63}Cu and ^{17}O for various cuprates. (left panel): Planar Cu data measured by NQR for the La- and Y-based systems as well as by NMR for Hg-, and Pr-based systems (for the NMR spectra, the CT frequency was subtracted for comparison with NQR). Note that some lineshapes are influenced by ^{65}Cu or resonances from inequivalent sites. Even so, almost all cuprates show linewidths of a few MHz. Exceptions are the stoichiometric compounds, $YBa_2Cu_3O_7$ and $YBa_2Cu_4O_8$, with an order of magnitude smaller widths. (right panel): Full spectra of planar O measured by NMR for various cuprates in $c \parallel B_0$ orientation. For better comparison, the shift from the central transition is shown. The asymmetry in linewidths and different peak intensities for the lower and upper satellite transitions (marked with gray dashed lines) signal a correlation of charge and spin density variations. Literature data from Refs. [Haase and Slichter, 2003; Haase et al., 2002; Jurkutat et al., 2014; Lee et al., 2017; Mangelschots et al., 1992; Ohsugi et al., 1994; Rybicki et al., 2012; Yoshinari et al., 1990].

they broaden fast by doping or element substitution [Williams, 2007; Williams et al., 2001; Yoshinari et al., 1990] and the observed lines are rather featureless, the variation of the planar Cu EFG in the cuprates was attributed to chemically induced disorder, i.e., an issue of the sample quality or caused by symmetry-breaking doping of these materials.

In Fig. 4.1 (right panel) the full set of five NMR resonance lines of planar ^{17}O ($I = 5/2$) is shown for various cuprates in $c \parallel B_0$. The quadrupole interaction measured by the splitting between the lines is much smaller compared to ^{63}Cu since the two nuclei differ in their electric quadrupole moment eQ by a factor of about 8 and experience different charge environments. The average splitting for the different materials is described by the planar O hole content n_p, cf. Sec. 2.3.2. As expected, the O linewidth is much more narrow than the observed width for Cu, however, for most cuprates a clear asymmetry is present which is most easily seen by the different height between the STs, cf. first upper and lower O satellite transition in Fig. 4.1. This was interpreted as due to a correlation between the magnetic and quadrupolar distribution which disappears below T_c indicating that the spin susceptibility is involved [Haase et al., 2000]. Furthermore, the satellite transitions of the stoichiometric compounds $\mathrm{YBa_2Cu_3O_7}$ and $\mathrm{YBa_2Cu_4O_8}$ reveal a special feature, i.e., an additional quadrupolar line splitting. This was attributed to the orthorhombicity of the crystal early on [Takigawa et al., 1989], however, it was also argued, that the two peaks could signal planar oxygen charge order [Haase and Slichter, 2003]. In Ch. 5, the origin of the splitting will be closer investigated.

To estimate the size of the planar charge variations in the cuprates, one is tempted to use Eq. (2.14) and (2.15) to calculate the variation of the planar Cu (Δn_d) and O (Δn_p) hole contents [Reichardt et al., 2016]. The quadrupolar distributions in $c \parallel B_0$ measured as the full width at half maximum (FWHM): $^{63}\Lambda_{\mathrm{Q},c}$ and $^{17}\Lambda_{\mathrm{Q},c}$ of planar Cu and O, respectively, are calculated using Eq. (2.13)[1]. Assuming for simplicity no correlations ($\langle \Delta n_\mathrm{d} \Delta n_\mathrm{p} \rangle$=0) rather than a specific scenario, as well as that the quadrupolar distribution is determined for the most part by the planar charge variation, the quadrupolar linewidth is given by:

$$^{17}\Lambda_{\mathrm{Q},c} = \frac{1}{2} \cdot 2.45\,\mathrm{MHz} \cdot \Delta n_\mathrm{p} \tag{4.1}$$

$$^{63}\Lambda_{\mathrm{Q},c} = \sqrt{(94.3\,\mathrm{MHz})^2 \cdot \Delta n_\mathrm{d}^2 + (22.7\,\mathrm{MHz})^2 \cdot \Delta n_\mathrm{p}^2}. \tag{4.2}$$

The factor 1/2 in Eq. (4.1) accounts for O EFG's main principle axis along the planar Cu-O bond direction.

Typical planar Cu and O spectra, some of them shown in Fig. 4.1, were analyzed using

---

[1] While σ_Q^2 is the second moment of a Gaussian distribution used for the analysis in Eq. (2.13), $\Lambda_\mathrm{Q} = 2\sqrt{2\ln 2}\,\sigma_\mathrm{Q}$ is the respective FWHM.

Table 4.1: Quadrupolar linewidths and estimated resulting planar charge variations, assuming negligible correlations for different cuprate families (details in text). Literature data are from [Haase et al., 2002; Jurkutat et al., 2014; Lee et al., 2017; Ohsugi et al., 1994; Rybicki et al., 2012; Yoshinari et al., 1990; Zheng et al., 1996]

Compound	$^{17}\Lambda_{\mathrm{Q},c}$ (kHz)	$^{63}\Lambda_{\mathrm{Q},c}$ (MHz)	Δn_p (10^{-2})	Δn_d (10^{-2})
$La_{1.85}Sr_{0.15}CuO_4$	37	2.09	3.1	2.1
$YBa_2Cu_3O_{6.9}$	10	0.28	0.8	0.2
$YBa_2Cu_3O_{6.8}$	34	2.9	2.8	3.0
$HgBa_2CuO_{4+\delta}$	29	2,67	2.4	2.8
$Tl_2Ba_2Ca_2Cu_3O_{10}$	62	2.82	5.1	2.7
$Pr_{1.95}Ce_{0.05}CuO_4$	16	6.48	1.3	6.9

(4.1) and (4.2) with the result summarized in Tab. 4.1[1]. In the presumed picture, the variation of the local charge at both Cu ($0.002 \leq \delta n_\mathrm{d} \leq 0.07$) and O ($0.008 \leq \delta n_\mathrm{p} \leq 0.05$) are significant.

That these rather large planar charge variation are due to chemically (high energy) induced disorder has not been proven yet and there are some experiments which indicate that a more soft mechanism contribute to the linewidth. For example, the doping dependence of the quadrupolar linewidth is unusual. One would expect that increasing chemical disorder would continuously broaden the line. In fact, it was shown that the planar Cu quadrupolar linewidth of the undoped materials is negligible and increases fast for low doping levels and saturates by further doping [Gippius et al., 1997; Imai et al., 1993; Jurkutat, 2015; Ohsugi et al., 1994]. In addition, high quality single crystals of $HgBa_2CuO_{4+\delta}$ show two narrow ^{199}Hg NMR ($I = 1/2$) lines which originates from Hg atoms far away and close by the chemical dopant (interstitial O) with an intensity ratio providing a measure for the doping δ [Rybicki et al., 2012]. This is what one would expect for a homogeneous system. The planar Cu quadrupole distribution on the other hand is very large, cf. Fig. 4.1. Thus, the CuO_2 plane seems to have a very fragile electronic homogeneity. Very recently, it was shown that the planar Cu and O quadrupolar linewidth and shape are influenced by high magnetic fields and temperature [Wu et al., 2011, 2013, 2015]. This was interpreted as a planar charge density wave which signals that the planar EFG can be influenced by low energy perturbations.

Clearly, the NMR and NQR linewidth measures static properties and dynamic charge

---

[1] It was accounted for spectral contribution from other isotope's transitions or resonances from inequivalent sites in the unit cell.

inhomogeneities, ordered or not, may be omnipresent in the cuprates and need to be pinned to become visible in the NMR spectrum, e.g., by chemical impurities or other perturbing interactions. Thus, the investigation of the planar Cu and O EFG by any external perturbation which does not change the crystallographic structure may help to clarify the origin of the linewidth. For this, the chemically clean (stoichiometric) $YBa_2Cu_4O_8$ and $YBa_2Cu_3O_7$ as well as the slighly underdoped material $YBa_2Cu_3O_{6.9}$ were investigated for this thesis by varying the pressure and magnetic field, and the results will be presented in the following sections.

4.2 Pressure induced variations of the Cu EFG

It is well known that pressure affects the planar Cu EFG, i.e., in different cuprates it was found that the quadrupole frequency ${}^{63}\nu_{\mathrm{Q}}$ which is proportional to the largest EFG component V_{ZZ} changes with pressure [Machi et al., 1995; Zheng et al., 1995; Zimmermann et al., 1990]. The pressure response $(d\nu_{\mathrm{Q}}/dp)$ has been measured by NQR and was found to be positive in $YBa_2Cu_3O_7$ and $YBa_2Cu_4O_8$ but negative in $La_{1.85}Sr_{0.15}CuO_4$. Furthermore, it was argued that ${}^{63}\nu_{\mathrm{Q}}(p)$ cannot be explained by a simple lattice compression and the changes were attributed to a pressure induced doping of the plane. [Zheng et al., 1995] However, whether the pressure induced changes of the EFG vary spatially has not been discussed largely.

The NQR linewidth of planar Cu measures the spatial variation of the main principle value ΔV_{ZZ}. An increasing linewidth under pressure has been observed [Machi et al., 1995; Meissner, 2012], but has not been investigated closer. Since the quadrupole splitting depends on pressure, a variation of ${}^{63}\nu_{\mathrm{Q}}$ could always hint to an inhomogeneous pressure distribution. Thus, care needs to be taken for the investigation of the linewidth since non-hydrostatic strains and more excotic phenomena as oxygen migration [Sadewasser et al., 2000] may influence the width.

In this regard the investigation of the stoichiometric compounds of YBCO is of advantage: First of all, the lines at ambient conditions are narrow and thus easy to obtain. Furthermore, there is no structural phase transition in the observed pressure range [Calamiotou et al., 2009] and due to the full chains, oxygen migration can be excluded.

4.2.1 Pressure dependence of T_{c}

The pressure dependence of the critical temperature T_{c} was measured with the self-resonance method introduced in Sec. 3.2.4 and is shown in Fig. 4.2 for the two investigated stoichiometric materials as well as the oxygen exchanged sample. While T_{c} decreases for the slightly overdoped material $YBa_2Cu_3O_7$, it increases with a much larger slope in the underdoped

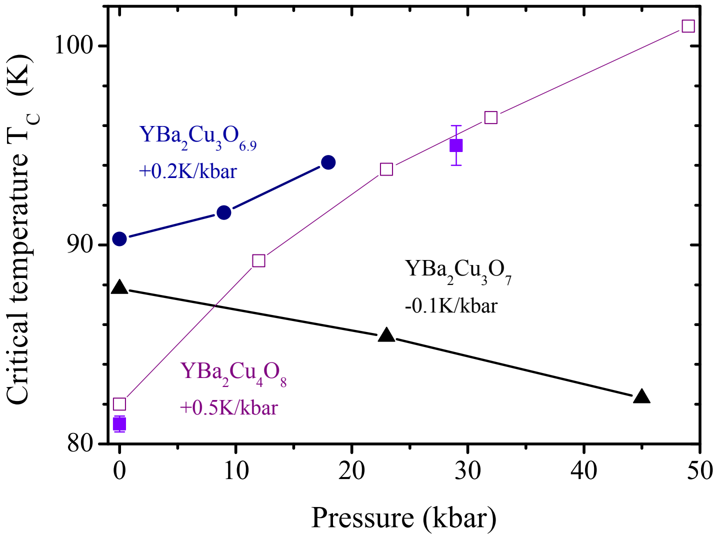

Figure 4.2: Pressure dependence of the critical temperature of superconductivity T_c of the investigated samples. The underdoped material $YBa_2Cu_4O_8$ shows a large increase of T_c with pressure (full purple symbols). The pressure dependence of a previous study (open symbols) [Meissner, 2012] is shown for comparison. While the overdoped $YBa_2Cu_3O_7$ (black) reveals a decreasing $T_c(p)$, the critical temperature of the oxygen exchanged sample $YBa_2Cu_3O_{6.9}$ (blue) increases with pressure. The initial slope of each sample can be found below the chemical formula.

$YBa_2Cu_4O_8$. This behavior is known from literature [Braithwaite et al., 1991; Sadewasser et al., 2000] and was attributed to the different positions in the phase diagram, i.e., the slope (dT_c/dp) is believed to be proportional to (dT_c/dx). Under these assumptions, the doping level of the oxygen exchanged sample $YBa_2Cu_3O_{6.9}$ were set, i.e., while the ambient pressure T_c is not sufficient to set y, the positive slope of $T_c(p)$ hints at underdoped behavior, cf. Sec. 3.3.1.

4.2.2 Pressure NQR on $YBa_2Cu_4O_8$

In this paragraph the pressure response of the quadrupolar frequency as well as the quadrupolar linewidth of planar Cu in powder $YBa_2Cu_4O_8$ up to 29 kbar is presented which was measured with NQR. There is a single transition for Cu having a spin $I = 3/2$ in NQR and the pressure evolution of the obtained planar ^{63}Cu spectrum at 300 K is shown in Fig. 4.3. Beside a shift to higher frequencies, there is a large line broadening under pressure apparent, i.e., the width increases from 240 kHz at ambient conditions to 1500 kHz at 29 kbar. Since the EFG asymmetry parameter is negligible for planar ^{63}Cu, the change of the NQR frequency measures directly the change of the quadrupolar frequency $^{63}\nu_Q$, cf. Eq. (2.12). Furthermore, single crystal NMR experiments on planar Cu for $c \parallel B_0$ revealed a narrow CT

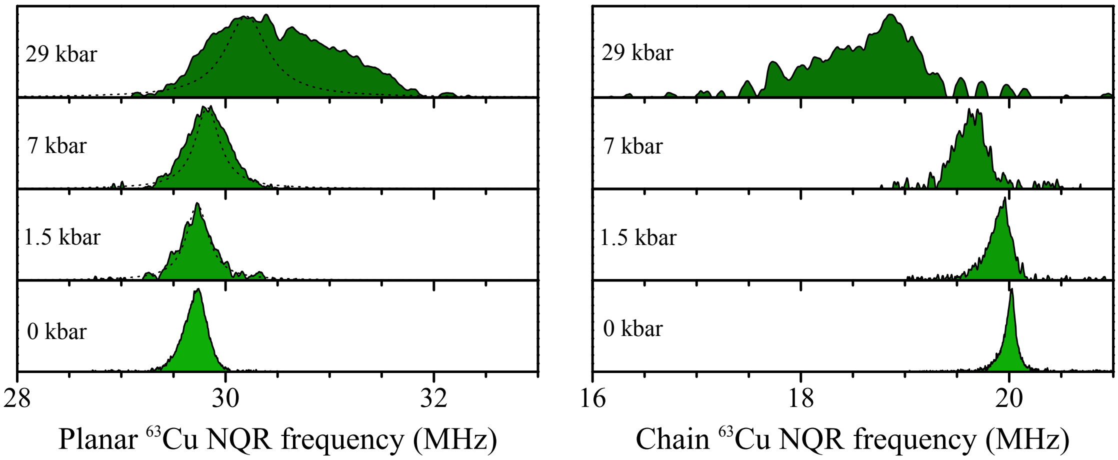

Figure 4.3: Pressure dependence of the NQR spectra of planar ^{63}Cu (left) and chain ^{63}Cu (right) at 300 K. The dashed lines in the spectra of planar ^{63}Cu indicate the expectation of the linewidth from a worst case scenario, i.e., they represent the ambient pressure spectrum broadened by a pressure gradient obtained from the linewidth of the chain ^{63}Cu. See text for details.

(≈35 kHz) [Sambala, 2010] which gives an upper boundary for the field independent dipole-dipole broadening. Since this upper boundary is small compared to the measured NQR linewidth of > 240 kHz, dipole-dipole broadening can be neglected and the NQR linewidth of planar Cu reveals the distribution of the quadrupole frequency $^{63}\Lambda_{\mathrm{Q}}$ measured as the full width at half maximum (FWHM).

For each pressure value, the NQR spectrum of the chain ^{63}Cu was measured which is also shown in Fig. 4.3. The line shifts to lower frequencies with pressure, however, a similar large broadening appears. Unlike planar Cu, the EFG asymmetry is substantial for the chain site and thus, the spectra does not simply reveal a single EFG parameter. The change of the NQR frequencies of both Cu sites are depicted in Fig. 4.4. The slope $d(^{63}\nu_{\mathrm{NQR}})/dp$ of 22 kHz/kbar (-49 kHz/kbar) for planar (chain) ^{63}Cu have been measured before and were interpreted as the alteration of the respective Cu valence states with pressure [Zimmermann et al., 1990].

In the following the large increase of the planar Cu quadrupole linewidth will be discussed. Since the NQR line shifts with pressure, pressure inhomogeneities could induce line broadening in addition to any intrinsic broadening $\Lambda_{\mathrm{int}}(p)$. For simplicity, one can assume that the experimentally observed linewidth is given by:

$$\Lambda^2_{\mathrm{exp}}(p) = \Lambda^2(0) + \Lambda^2(\Delta p) + \Lambda^2_{\mathrm{int}}(p), \tag{4.3}$$

with $\Lambda(0)$ and $\Lambda(\Delta p)$ the 0 kbar NQR linewidth and the width induced by pressure inho-

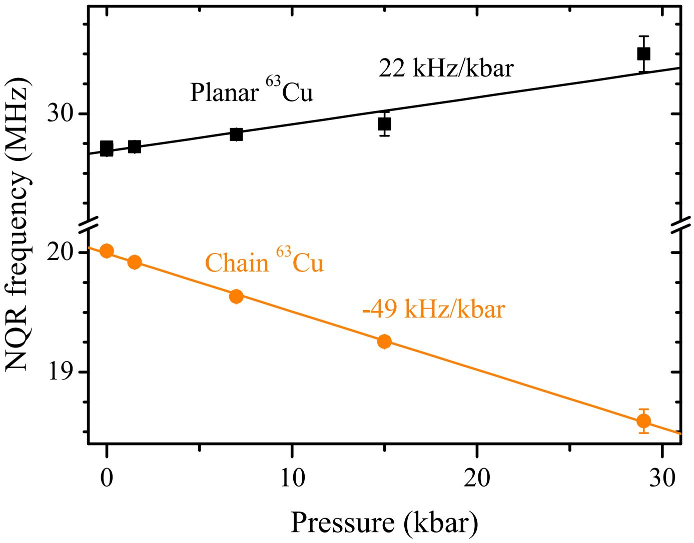

Figure 4.4: Pressure dependence of the measured NQR frequency for planar (black) and chain (orange) ^{63}Cu at 300 K. For planar Cu, the EFG anisotropy is negligible, and thus the obtained frequencies are identical with the quadrupolar frequency $^{63}\nu_{\mathrm{Q}}$. However, for the chain Cu, the anisotropy is substantial and the respective $^{63}\nu_{\mathrm{Q}}$ cannot be measured with NQR.

mogeneities Δp, respectively. The former is given by the width of the unperturbed system and the latter can be calculated in a linear approach by: $\Lambda(\Delta p) = d(^{63}\nu_{\mathrm{Q}})/dp \cdot \Delta p$. Since $d(^{63}\nu_{\mathrm{Q}})/dp$ is known, cf. Fig. 4.4, one has to estimate Δp. In the following different methods are used to estimate Δp and it is discussed whether they are sufficient to account for the observed linewidth or an intrinsic broadening $\Lambda_{\mathrm{int}}(p)$ is present.

The pressure within the cell is measured by the shift of the ruby luminescence spectrum, cf. Sec. 3.2.1, and thus, pressure gradients experienced by the ruby chip in the sample chamber will broaden the ruby lines. In Fig. 4.5, the spectra corresponding to the NQR measurements are shown and since the shifted ambient spectrum (dashed line) is identical to the high pressure spectrum, local pressure gradients can be excluded. However, ruby chips at different positions in the pressure cell reveal an uncertainty of $\Delta p \approx 1\,\mathrm{kbar}$. Clearly, the corresponding pressure induced broadening $^{63}\Lambda(\Delta p) = 22\,\mathrm{kHz}$ cannot explain the data. A large increase of the planar and chain Cu linewidth has also been reported by Machi et al. [1995]. In this paper, pressure inhomogeneities were ruled out by the unaffected superconducting transition width of metallic Pb. However, in a later paper it was claimed that the usage of epoxy resin for sample fixing can cause inhomogeneous pressure distributions [Machi et al., 1998]. Indeed, any added medium for pressure calibration is not sufficient to rule totally out that the sample is exposed to pressure inhomogeneities. Thus, the pressure response of different parameters

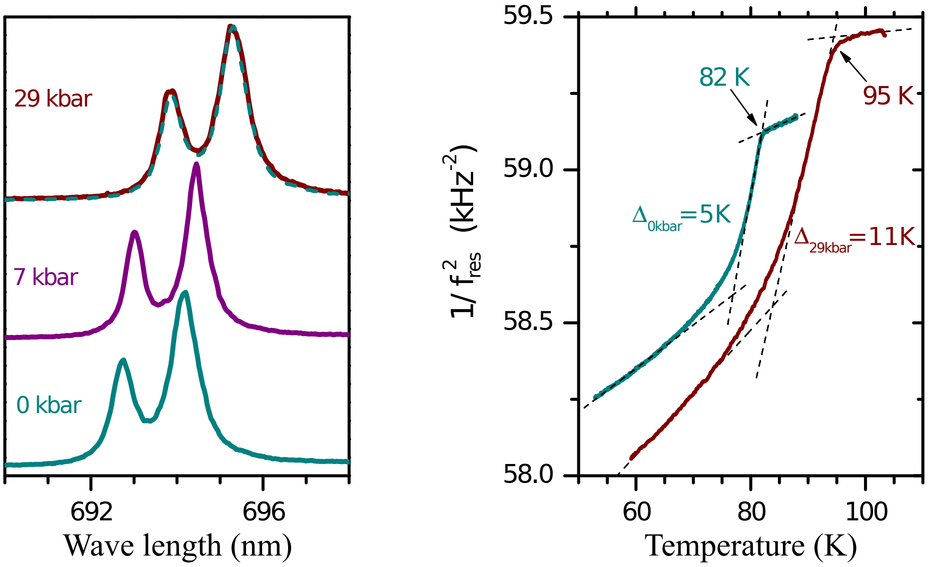

Figure 4.5: Ruby luminescence spectrum (left) and superconducting transition (right) of the corresponding pressure dependent NQR measurements on $YBa_2Cu_4O_8$. (left) The shift of the ruby lines is due to increasing pressure. The dashed cyan line in the 29 kbar spectrum is the shifted 0 kbar spectrum revealing no significant pressure gradient across the ruby chip. (right) Pressure increases T_c as well as the transition width which was measured by the difference of the intersection points of the linear parts of the $f_{res}^{-2}(T)$-curve (dashed lines).

of the investigated sample must be evaluated[1].

One parameter which can be used for this purpose is the critical temperature T_c which increases with a initial slope of about 0.5 K/kbar, cf. Fig. 4.2. The measured transitions for 0 kbar and 29 kbar[2] are shown in Fig. 4.5. Although a clear transition into the superconducting phase is revealed, the transition width defined as the difference of the intersection points of the linear parts of the measured curve increases by 6 K. If the increase of the width is solely given by pressure inhomogeneities, it would correspond to $\Delta p = 12\,$kbar, a rather large variation compared to the pressure determined with ruby luminescence (29 kbar). Since a clear edge at the transition is visible and the measured $T_c(p)$ agree with the values obtained using different methods [Braithwaite et al., 1991; Van Eenige et al., 1990], the pressure variation would have a substantial negative skewness. Thus, in the linear approach, the large and asymmetric pressure distribution would result in a asymmetric broadening with $\Lambda(\Delta p) = 264\,$kHz which still cannot explain the observed planar Cu linewidth of 1500 kHz at 29 kbar.

---

[1] However, as long as the underlying mechanisms are not understood, the comparison of different parameters will only give an estimated upper boundary for the effect of pressure inhomogeneities.

[2] The measurements were performed in different pressure cells, i.e., the amount of sample could vary and was not measured.

Another worst case scenario to obtain an upper boundary for Δp can be drawn by comparing the linewidth of planar and chain Cu. Since the NQR frequencies of both sites change with pressure, a pressure distribution will broaden both lines. Using the ratio of the slopes of the pressure dependent NQR frequencies of the two Cu sites, i.e., $|(d(^{63}\nu_{\mathrm{NQR}})/dp)_{\mathrm{plane}} : (d(^{63}\nu_{\mathrm{NQR}})/dp)_{\mathrm{chain}}| = 0.45$, the obtained pressure induced linewidth $\Lambda(\Delta p)$ can be scaled from chain Cu to planar Cu. The expected planar Cu linewidth Λ_{exp} is calculated using Eq. (4.3) with $\Lambda_{\mathrm{int}}(p) = 0$, and is illustrated as a Lorentz line for the different pressure values in Fig. 4.3. A significant discrepancy becomes apparent already at low pressure (7 kbar) which become more pronounced in the spectrum at 29 kbar, i.e., the expected linewidth is only about 500 kHz.

To conclude, sample internal as well as external estimates of pressure inhomogeneities do not allow to measure the precise pressure inhomogeneities quantitatively within the sample chamber of the pressure cell, however, the estimated upper boundaries for pressure variations (worst case) cannot account for the large increase of the planar Cu linewidth. Thus, a substantial contribution of intrinsic inhomogeneities to the planar ^{63}Cu linewidth must be present which is larger than 1400 kHz at 29 kbar.

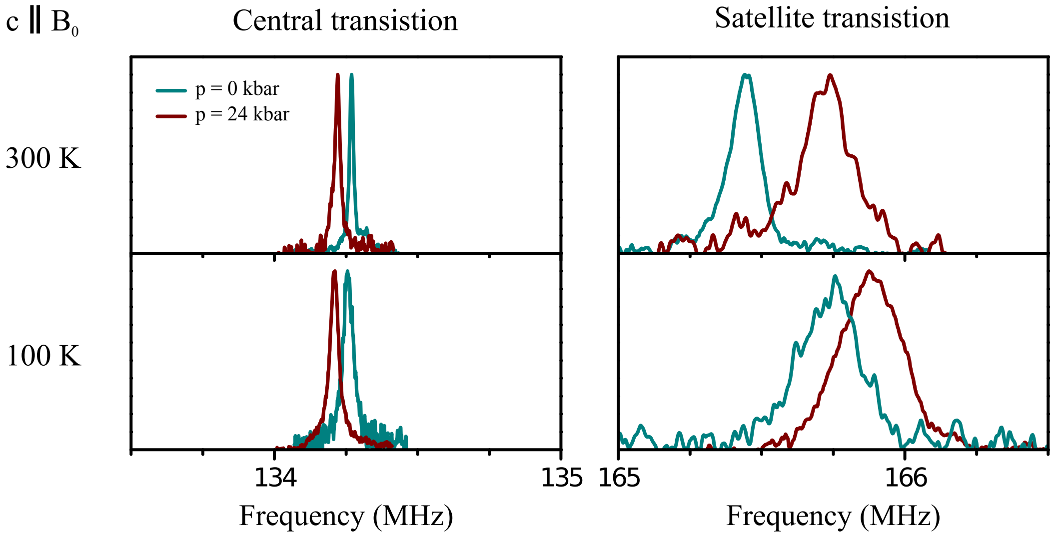

Figure 4.6: Pressure dependence of the planar ^{63}Cu central transition (left) and high frequency ($-1/2 \longleftrightarrow -3/2$) satellite transition (right) of $YBa_2Cu_3O_7$ for 300 K (upper panel) and 100 K (lower panel) for $c \parallel B_0$. Pressure and lower temperatures shift the CT and ST to lower and higher frequencies, respectively. The linewidth of the ST is much broader than the width of the CT and pressure but also lower temperatures increase the width of both transitions.

4.2.3 Pressure NMR on $YBa_2Cu_3O_7$

Using NMR, the pressure and temperature dependence of the quadrupolar frequency as well as the quadrupolar linewidth of planar Cu was investigated in a single crystal of $YBa_2Cu_3O_7$ up to 24 kbar. For this purpose, the crystal's c-axis was aligned with the magnetic field ($c \parallel B_0$). In this section, the obtained spectra and their analysis will be presented.

The pressure and temperature evolution of the planar ^{63}Cu spectra is exemplary shown for the CT and high frequency ST for 0 and 24 kbar in Fig. 4.6. While the CT in this orientation is solely determined by the magnetic shift $K_\parallel$, the position of the ST is given by the sum of a magnetic and first order quadrupole part. Pressure but also temperature decreases the magnetic shift slightly, while the ST is shifted to higher frequencies. The quadrupolar frequency $^{63}\nu_\mathrm{Q}$ is simply given by the distance between the three planar Cu transitions and the pressure and temperature modifications are shown in Fig. 4.7 (a). The quadrupolar frequency increases with pressure linearly with a slope of 14 kHz/kbar at 300 K which was observed before [Müller et al., 1989]. In this material, temperature appears to be similarly efficient in changing $^{63}\nu_\mathrm{Q}$, in fact, in comparison to ambient conditions (0 kbar, 300 K) cooling down to 100K at 0 kbar changes $^{63}\nu_\mathrm{Q}$ in the same manner as squeezing the sample with 24 kbar at 300 K. Note, that at high pressure, the modification of $^{63}\nu_\mathrm{Q}$ by temperature is less than at low pressures.

From Fig. 4.6 it is obvious that the CT is much more narrow than the ST. This is typical for planar Cu NMR in the cuprates where in addition to magnetic broadening (measured by the width of the CT), a large quadrupole distribution broadens the ST. In Tab. 4.2, the linewidth (FWHM) for all transitions is collected, and using Eq. (2.13) the quadrupolar contribution $^{63}\Lambda_\mathrm{Q}$ was calculated and is listed in the last column.

Clearly, the satellite linewidth is dominated by the quadrupolar distribution and thus, the satellite linewidth is a direct measure for $^{63}\Lambda_\mathrm{Q}$. Both, the magnetic and quadrupolar distribution increases substantially by pressure and temperature in $YBa_2Cu_3O_7$, e.g., $^{63}\Lambda_\mathrm{Q}$

Table 4.2: Pressure and temperature dependent linewidth of planar ^{63}Cu central transition (CT) as well as low (LF) and high (HF) frequency satellite transition (ST) in $YBa_2Cu_3O_7$. The linewidths are measured as the FWHM. $\Lambda_\mathrm{Q} = 2\sqrt{2\ln 2}\sigma_\mathrm{Q}$ is the corresponding quadrupolar linewidth calculated using Eq. (2.13).

T (K)	p (kbar)	LF ST (kHz)	CT (kHz)	HF ST (kHz)	$^{63}\Lambda_\mathrm{Q}$ (kHz)
300	0	130	15	115	120
300	24	235	24	210	220
100	0	230	42	210	220
100	24	325	36	320	320

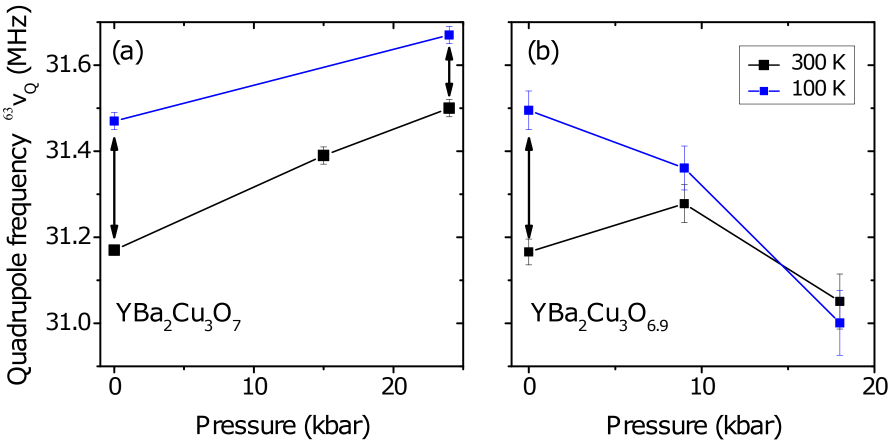

Figure 4.7: Pressure dependence of the planar ^{63}Cu quadrupole frequency $^{63}\nu_Q$ in $YBa_2Cu_3O_7$ (a) and $YBa_2Cu_3O_{6.9}$ (b) for 300 K (black) and 100 K (blue).

increases by almost a factor of three from ambient conditions to 24 kbar 100 K. Similar to the discussed pressure inhomogeneities in $YBa_2Cu_4O_8$, the change of the CT with pressure and its increasing linewidth at 300 K can be use to estimate an upper boundary[1] which yield $\Delta p = 9$ kbar and corresponds to $\Lambda(\Delta p) = 125$ kHz. Using Eq. (4.3), this worst case scenario leads to a broadening of 175 kHz, which is significantly smaller than the observed with at 24 kbar, cf. Tab. 4.2. Similar to $^{63}\nu_Q$, pressure and temperature modify the quadrupolar variation $^{63}\Lambda_Q$ to the same extent. The unusual temperature modification of the planar Cu satellite linewidth at ambient pressure will be closer investigated in Sec. 4.3.

4.2.4 Pressure NMR and NQR on $YBa_2Cu_3O_{6.9}$

The pressure and temperature dependence of the quadrupolar frequency as well as the quadrupolar linewidth of planar Cu of the oxygen exchanged single crystal $YBa_2Cu_3O_{6.9}$ was measured with NMR in $c \parallel B_0$ and with NQR up to 18 kbar. The results will be presented in this section. NMR on planar oxygen allows to align the magnetic field along the Cu-O-Cu bond direction of the CuO_2 plane ($B_0 \parallel \sigma \perp c$), cf. Sec. 3.2.3, and the corresponding experimental data of planar Cu and O as well as their analysis can be found in Ch. 5.

In Fig. 4.8, the spectra of the ^{63}Cu CT and high frequency ST at 0 kbar and 18 kbar can be found. Note, that the frequency range is by a factor of two larger than in Fig. 4.6, i.e., the ST but also the CT are broader in the slightly underdoped material compared to stoichiometric $YBa_2Cu_3O_7$. This broadening is usually attributed to planar inhomogeneities

---

[1] The critical temperature was not measured for this set of experiments.

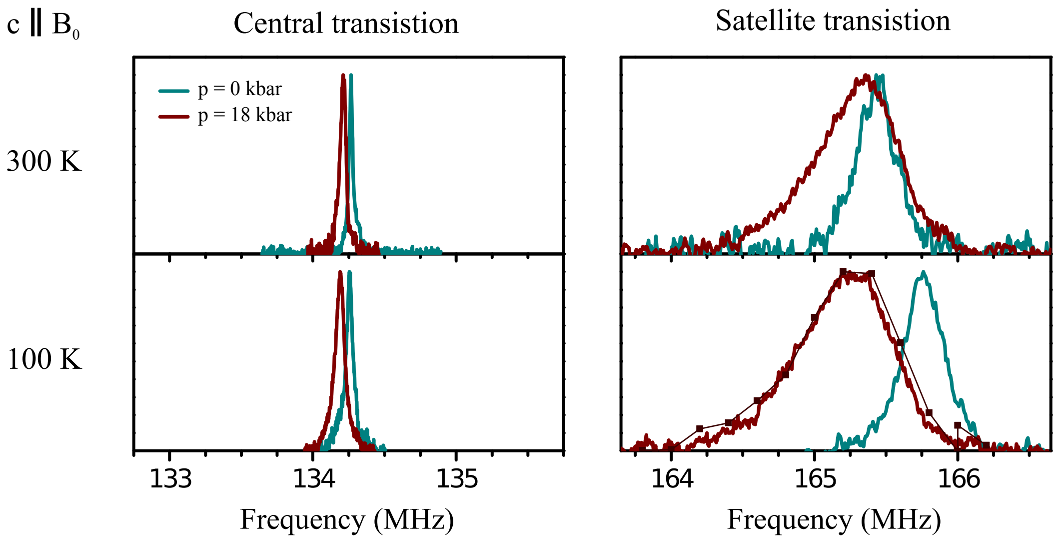

Figure 4.8: Pressure dependence of the planar ^{63}Cu central transition (left) and high frequency ($-1/2 \longleftrightarrow -3/2$) satellite transition (right) of $YBa_2Cu_3O_{6.9}$ for 300 K (upper panel) and 100 K (lower panel) for $c \parallel B_0$. Pressure and lower temperatures shift the CT to lower frequencies. While at 300 K, the shift of the ST is not uniform, at 100 K, pressure shifts the ST to lower frequencies. Also shown is a frequency stepped experiment at 100 K (braun squares). The linewidth of the ST is much broader than the width of the CT, and pressure but also lower temperatures increase the width of both transitions. Note that the frequency scale is by a factor of two larger than in Fig. 4.6.

introduced by vacant oxygen sites in the CuO chain layers[1]. As for $YBa_2Cu_3O_7$, the CT which measures the magnetic shift $K_{\|}$, decreases slightly with pressure and temperature and is much more narrow than the ST. Thus, as discussed before, the splitting between the different transitions measures $^{63}\nu_Q$ and the satellite linewidth measures the quadrupole distribution $^{63}\Lambda_Q$. The pressure dependence of the quadrupole frequency $^{63}\nu_Q$ is shown in Fig. 4.7 (b) for 300 K and 100 K. While the ambient pressure quadrupole splitting is identical to the observed splitting in $YBa_2Cu_3O_7$, the pressure response is different. At 300 K, $^{63}\nu_Q(p)$ increases initially with approximately the same slope as found in the fully doped material, but than decreases. Opposite to $YBa_2Cu_3O_7$, $^{63}\nu_Q(p)$ solely decreases at 100 K with a much larger rate (-27 kHz/kbar) compared to the stoichiometric compound $YBa_2Cu_3O_7$. Pressure reduces the temperature dependence of $^{63}\nu_Q$, i.e., $^{63}\nu_Q(300\,K) \approx {}^{63}\nu_Q(100\,K)$ at 18 kbar. As it can be seen in Fig. 4.8 the quadrupole distribution $^{63}\Lambda_Q$ increases by a factor of two from ambient pressure to 18 kbar. Lowering the temperature broadens the line considerably, but not as much as observed for $YBa_2Cu_3O_7$. From the increase of the superconducting

---

[1] Vacant oxygen sites allow for oxygen migration under pressure, however, the effect of oxygen migration on the planar doping level x and its variation Δx is expected to be small for materials close to optimal doping [Schilling, 2007].

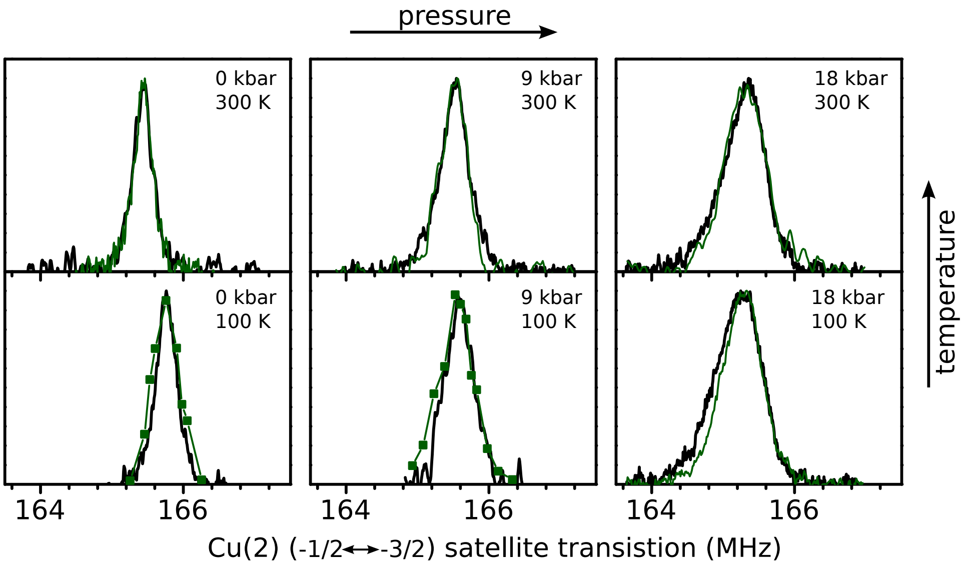

Figure 4.9: Comparison of the pressure and temperature dependence of the planar ^{63}Cu NMR satellite transition in $c \parallel B_0$ with the NQR spectrum. The pressure dependence of the high frequency ST in $c \parallel B_0$ for 300 K (upper panel) and 100 K (lower panel) are shown in black. In green are the spectra which were simulated with an exact diagonalization program of the spin and quadrupole Hamiltonian using the quadrupolar distribution measured by NQR and the magnetic shift obtained from the CT.

transition's width by 1 K[1] an upper bound for pressure inhomogeneities $\Delta p = 5$ kbar is found which would result in a linewidth at 100 K of about 330 kHz which is less than half of what is observed. A similar result is obtained using the change of the CT and its linewidth to estimate an upper boundary for pressure inhomogeneities.

For this compound, the quadrupolar frequency and its distribution was also measured by NQR. For comparison, the quadrupolar distribution measured without a magnetic field (NQR), as well as the magnetic shift obtained from the NMR CT, were used to calculate the expected NMR transitions, cf. Sec. 2.2. Note that no additional magnetic distribution was used. The results are illustrated in Fig. 4.9 for the high frequency ST in $c \parallel B_0$. The simulated line positions agree with the measured ST. Furthermore, the spectral distribution of the ST is given by the quadrupolar distribution, as expected for a negligible small magnetic variation. The comparison of the NMR with the NQR spectra underpin the unusual pressure dependence of the quadrupolar splitting, cf. Fig. 4.7, as well as its large variation at high pressures and it will be used in Sec. 4.3 to identify magnetic field dependent properties of the EFG.

---

[1] The superconducting transitions width increases from 1 K at 0 kbar to 2 K at 18 kbar.

4.2.5 Discussion of the planar Cu EFG modifications

In the last three subsections it was shown that the planar Cu quadrupole frequency ν_{Q} and its variation measured by Λ_{Q} depend on pressure and temperature. Since the quadrupole frequency is a direct measure of the largest principle value of the planar Cu EFG V_{ZZ} ($\nu_{\mathrm{Q}} = eQV_{ZZ}/2h$) and the asymmetry parameter η is small, the changes of $\nu_{\mathrm{Q}}(p,T)$ and $\Lambda_{\mathrm{Q}}(p,T)$ measure the pressure and temperature modifications of the planar Cu average EFG and its spatial variation.

Modifications of the planar Cu average EFG In Fig. 4.10 (a) the changes of ${}^{63}\nu_{\mathrm{Q}}$ with pressure and temperature are shown for the investigated samples which are compared with literature data. Clearly, there is a significant modification of ν_{Q} present.

The EFG which determines ν_{Q} depends on the local charge content and its symmetry. Pressure solely compress the lattice [Calamiotou et al., 2009] and one expects a monotonic behavior[1] in $\nu_{\mathrm{Q}}(p)$ from the lattice compression. Therefore, any non-monotonic curve signals additional effects. For example, it was argued that the different sign of the slopes ($d\nu_{\mathrm{Q}}/dp$) for $\mathrm{YBa_2Cu_4O_8}$ and optimally doped $\mathrm{La_{1.85}Sr_{0.15}CuO_4}$ cannot be related to a lattice compression by pressure [Zheng et al., 1991].

It is well known that holes are added to the $\mathrm{CuO_2}$ plane in YBCO, for instance, by increasing the chain O content and thereby both the planar and chain Cu quadrupole frequencies increase. Whereas, pressure was found to decrease the chain but to increase the planar Cu quadrupolar splitting, cf. Fig. 4.4, which was interpreted as a pressure induced charge transfer between the chain layer and the $\mathrm{CuO_2}$ plane [Zheng et al., 1991; Zimmermann et al., 1990]. That pressure effectively dopes the $\mathrm{CuO_2}$ plane was also found by other methods, cf. Sec. 2.3.3.

The cuprates differ largely in their structure and composition, however, as shown in Sec. 2.3.2, the large difference of the planar quadrupole splittings can be determined by the hole contents of planar Cu (n_{d}) and O (n_{p}), i.e., there is no material specific constant involved [Jurkutat et al., 2014]. Therefore, one expects that small modifications of the system as due to pressure or temperature will in first order affect the EFG through the change of the planar hole content and lattice effects can be neglected.

Compared to chemical modifications (chemical doping), the variation of ${}^{63}\nu_{\mathrm{Q}}$ with pressure is small ($< 3\%$ up 30 kbar), cf. Fig. 4.10 (b) and Tab. 4.3. However, the corresponding change of the hole contents are significant. For example, the change of ${}^{63}\nu_{\mathrm{Q}}$ by 0.8 MHz up to 29 kbar

---

[1] The EFG changes with the inverse volume for isotropic compression in a point ion model, however, depending on the specific model the lattice contribution to the EFG can either increase or decrease [Shimizu, 1993; Zheng et al., 1991; Zimmermann et al., 1990].

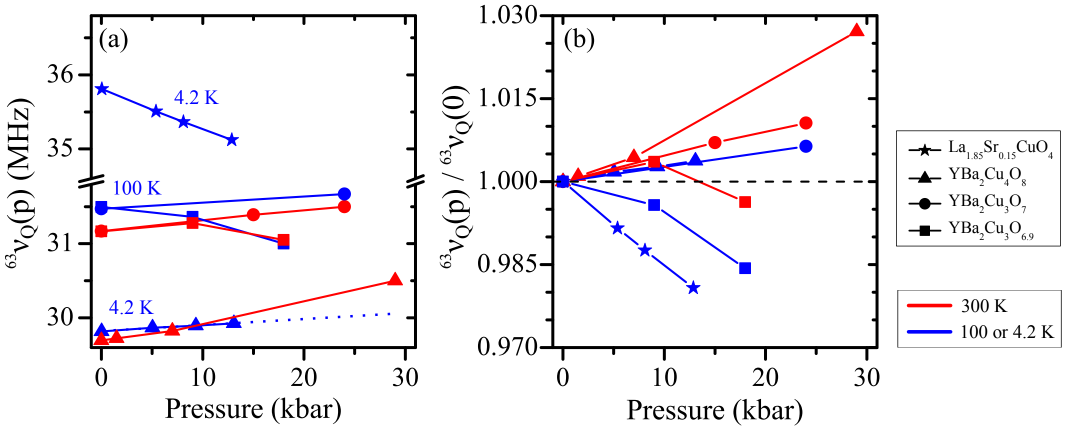

Figure 4.10: (a) Pressure dependence of the quadrupole frequency ${}^{63}\nu_\mathrm{Q}$ at high (red) and low temperatures (blue) for various cuprates. While at 0 kbar, ${}^{63}\nu_\mathrm{Q}$ is larger at low temperatures, pressure reduces and is even capable to inverse the difference in temperature. Dotted line is an linear extension of the measured data. (b) Pressure dependence of the quadrupole frequency scaled to ${}^{63}\nu_\mathrm{Q}$(p=0). While the slope is positive for $\mathrm{YBa_2Cu_3O_7}$ and $\mathrm{YBa_2Cu_4O_8}$, and larger at high temperatures, the slope is negative at low temperatures for the La-system and $\mathrm{YBa_2Cu_3O_{6.9}}$. The latter compound changes the sign of the slope at high temperatures. Low temperature data for $\mathrm{La_{1.85}Sr_{0.15}CuO_4}$ and $\mathrm{YBa_2Cu_4O_8}$ are from Zheng et al. [1991].

in $\mathrm{YBa_2Cu_4O_8}$ could originate from an increase of either the hole content of Cu ($\delta n_\mathrm{d} \approx 0.01$) or O ($\delta n_\mathrm{p} \approx 0.04$), but also a charge redistribution between the planar orbitals may be possible, cf. Eq. (2.15). That pressure does not alter the planar hole contents uniformly, i.e., only adds or removes holes, is revealed by the observation that $(d\nu_\mathrm{Q}/dp)$ changes the sign in $\mathrm{YBa_2Cu_3O_{6.9}}$ at 300 K. Furthermore, although the modifications of the lattice are minor between nearby doping levels[1], i.e., $y = 6.9$ and 7, the sign of the slope at 100 K differ between both samples. These observations hint to a more soft mechanism behind the distribution of charges which may also be affected by temperature.

Table 4.3: Pressure derivative of the planar ^{63}Cu quadrupole frequency and linewidth of the investigated samples at 300 K. To account for the changing sign, $(d({}^{63}\nu_\mathrm{Q})/dp)$ was estimated by a parabolic fit of the experimental data ${}^{63}\nu_\mathrm{Q}(p)$ for $\mathrm{YBa_2Cu_3O_{6.9}}$, i.e., $(d({}^{63}\nu_\mathrm{Q})/dp)$ is explicitly pressure dependent.

Compound	${}^{63}\nu_\mathrm{Q}(p=0)$ (MHz)	${}^{63}\Lambda_\mathrm{Q}(p=0)$ (kHz)	$d({}^{63}\nu_\mathrm{Q})/dp$ (kHz/kbar)	$d({}^{63}\Lambda_\mathrm{Q})/dp$ (kHz/kbar)
$\mathrm{YBa_2Cu_4O_8}$	29.70	240	22	44
$\mathrm{YBa_2Cu_3O_7}$	31.17	115	14	4
$\mathrm{YBa_2Cu_3O_{6.9}}$	31.17	300	$31 - 4p/\mathrm{kbar}$	19

---

[1] And also ${}^{63}\nu_\mathrm{Q}$ does not differ between the different chemical doping levels at ambient pressure.

Compared to chemical doping, the temperature dependence of the EFG is small, e.g., $^{63}\nu_{\mathrm{Q}}$ in $\mathrm{YBa_2Cu_4O_8}$ varies by about 200 kHz between 4.2 and 700 K [Zimmermann et al., 1989]. This was previously attributed to the thermal expansion of the lattice. However, it was shown that $^{63}\nu_{\mathrm{Q}}$ has a minimum at about 180 K in this material and since no structural phase transition occurs, the unusual effect was attributed to a change of the electronic system [Suter et al., 1997]. In Sec. 4.2.3 it was shown for $\mathrm{YBa_2Cu_3O_7}$, that pressure but also lowering the temperature can modify $^{63}\nu_{\mathrm{Q}}$ to the same extent. Furthermore, the slope $(d\nu_{\mathrm{Q}}/dp)$ is affected by temperature, i.e., for $\mathrm{YBa_2Cu_3O_7}$ and $\mathrm{YBa_2Cu_4O_8}$, it is positive and larger at higher temperatures, but for $\mathrm{YBa_2Cu_3O_{6.9}}$, $(d\nu_{\mathrm{Q}}/dp)$ changes between 300 K and 100 K, cf. Fig. 4.10 (b). Again, modifications of the lattice by temperature are not expected to change the sign of $(d\nu_{\mathrm{Q}}/dp)$. Thus, it is plausible that the planar orbital doping levels are affected by temperature as well.

Modifications of the spatial variation of the planar Cu EFG It was shown, that pressure increases the quadrupolar linewidth $^{63}\Lambda_{\mathrm{Q}}$ strongly and that pressure gradients, if present, cannot explain the observed linewidth. As discussed before, the quadrupole splitting is determined by the hole contents of planar Cu (n_{d}) and O (n_{p}) and is sensitive to pressure and even temperature. Thus, the quadrupolar linewidth is interpreted as a spatial distribution of planar charges which has been done before, cf. for instance Machi et al. [1995]; Rybicki et al. [2009].

In Fig. 4.11, the pressure dependence of the quadrupolar linewidth $^{63}\Lambda_{\mathrm{Q}}(p)$ of the investigated samples is shown. Although, they have all a small quadrupolar linewidth compared to other cuprates at ambient pressure, cf. Sec. 4.1, $^{63}\Lambda_{\mathrm{Q}}(p = 0)$ differs largely among the samples. In fact, $\mathrm{YBa_2Cu_3O_7}$ reveals the smallest planar Cu linewidth known for all cuprates of about 115 kHz, the linewidth of stoichiometric (chemically clean) $\mathrm{YBa_2Cu_4O_8}$ is twice as large[1]. In addition, chemical disorder in the chain layer as in $\mathrm{YBa_2Cu_3O_{6.9}}$ results in an increase of the quadrupolar linewidth by almost a factor of three compared to the fully doped material. Further reduction of the chain oxygen content increases the width even to a few MHz [Yoshinari et al., 1990]. The linewidth is also known to vary depending on the sample preparation [Zimmermann et al., 1988] and thus, the quadrupolar width is commonly interpreted as due to chemically induced planar disorder, cf. Sec. 4.1.

As it can be seen in Fig. 4.11, the linewidths of the investigated compounds increase strongly with pressure but to a different extent. The difference of the slopes shows no simple trend to neither $^{63}\nu_{\mathrm{Q}}$ nor to $(d\nu_{\mathrm{Q}}/dp)$, cf. Tab. 4.3. Since the initial linewidth $^{63}\Lambda_{\mathrm{Q}}(p =$

---

[1] A smaller linewidth of about 180 kHz at 300 K in $\mathrm{YBa_2Cu_4O_8}$ has been reported by Zimmermann et al. [1989].

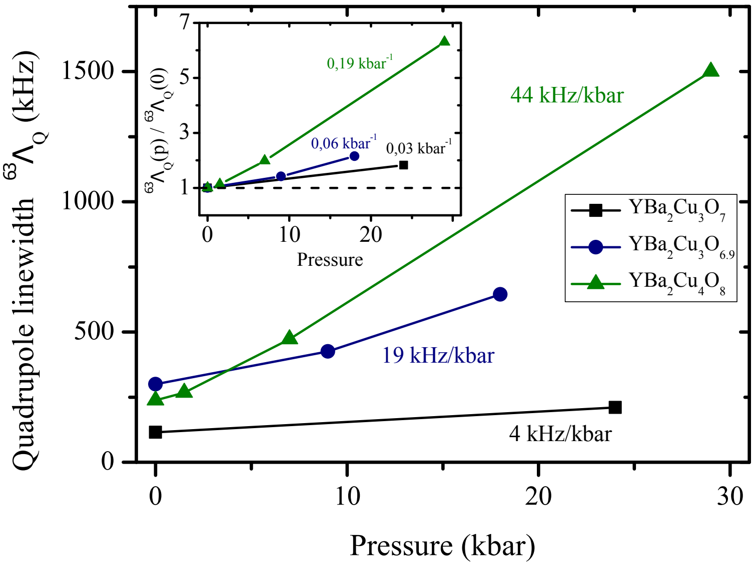

Figure 4.11: Comparison of the pressure dependence of the quadrupolar linewidth $^{63}\Lambda_{\rm Q}$ of planar ^{63}Cu of the investigated samples at 300 K. The inset shows the pressure dependent linewidth scaled to ambient conditions.

0) differ largely among the investigated samples, one may ask whether the slope is simply proportional to the width at ambient pressure. Than the quadrupolar linewidth scaled to the ambient pressure value $^{63}\Lambda_{\rm Q}(p)/^{63}\Lambda_{\rm Q}(0) = 1 + m_p \cdot p$ for different materials must fall on a single line with slope m_p. Such a scenario cannot be excluded for $YBa_2Cu_3O_{6+y}$, but $YBa_2Cu_4O_8$ behaves differently, cf. inset of Fig. 4.11.

The broadening by pressure is denoted by $\Lambda_{\rm int}(p)$ and can be calculated using Eq. (4.3) assuming that $\Lambda(\Delta p)$ are negligible. In Fig. 4.12, the pressure dependence of $\Lambda_{\rm int}$ is plotted which shows qualitatively the same behavior as the observed linewidth. Also plotted is the quadrupolar broadening $\Lambda_{\rm int}(y)$ due to chemically induced disorder by substitution y, e.g., Y and Ba can be substituted by Ca and La. The observed planar charge variation by pressure is of the same size as the variation due to chemical disorder. This is surprising since pressure is not expected to induce large planar charge inhomogeneities. Using Eq. (2.15) and assuming that only the planar hole content at either Cu or O varies (but not both simultaneously), the observed broadening due to pressure and chemical substitution correspond to a variation of $\Delta n_{\rm d} = 0.015$ and $\Delta n_{\rm p} = 0.06$, which is close to the variation observed in other cuprates, cf. Sec. 4.1. Still, the critical temperature $T_{\rm c}$ is almost independent or even increases by pressure, cf. Fig. 4.2, as well as by chemical disorder Williams [2007].

To conclude, the Cu EFG average value is determined by the hole contents at planar Cu and O, but on a smaller scale, it can be affected by low energy electronic excitations which

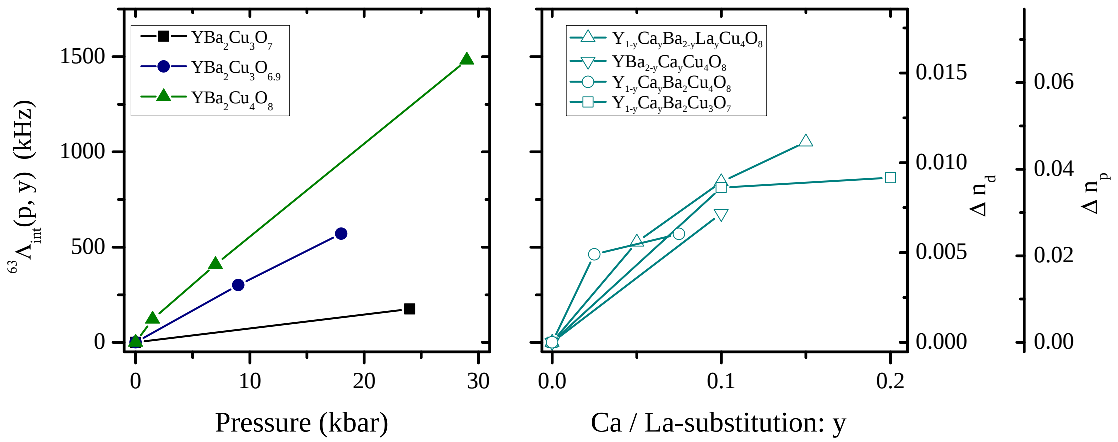

Figure 4.12: Planar ^{63}Cu quadrupolar broadening $\Lambda_{\text{int}}(p, y)$ (left axis) as a function of pressure p (left panel) and chemical substitution y (right panel) for different compounds. Also shown (righ axes) are the corresponding variation of the planar Cu (Δn_{d}) and O (Δn_{p}) hole contents assuming that the broadening is due to either Cu or O charge variations. Data shown in the right panel are from literature [Machi et al., 1992; Mangelschots et al., 1990; Williams, 2007; Williams et al., 2001].

are influenced by pressure and temperature. The spatial distribution of the EFG increases strongly with pressure and is comparable to the effect of chemically induced disorder. This is unusual as pressure is expected to perturb the system homogeneously and the line broadening rather signals an electronic instability.

The stoichiometric system YBa$_2$Cu$_3$O$_7$ exhibits the smallest width obtained in the cuprates. It was shown, that the quadrupolar width at ambient conditions (0 kbar, 300 K) is similarly increased by applying pressure or lowering the temperature, cf. Fig. 4.6. The possible origin of the temperature effect on the linewidth will be discussed in the next section.

4.3 Magnetic field induced variations of the Cu EFG

The planar charge density variation observed in underdoped YBa$_2$Cu$_3$O$_{6+\text{y}}$ are influenced by a magnetic field. For example, the charge order peak observed in x-ray experiments is enhanced by applying a magnetic field [Chang et al., 2012, 2016; Hücker et al., 2014]. In addition, NMR experiments found that the planar Cu and O satellites are split in a high magnetic fields which was interpreted as a field induced charge density wave [Wu et al., 2011, 2013]. Up to date, it is unclear whether all cuprates reveal this feature or whether it is exclusive for underdoped materials.

In this section, the magnetic field dependence of the planar Cu EFG in *overdoped* YBa$_2$Cu$_3$O$_7$ is investigated at ambient pressure. For this, a single crystal of YBa$_2$Cu$_3$O$_7$ with a size of about $\approx 2{\times}2{\times}0.7\,\text{mm}^3$ was investigated without a magnetic field using NQR and in a mag-

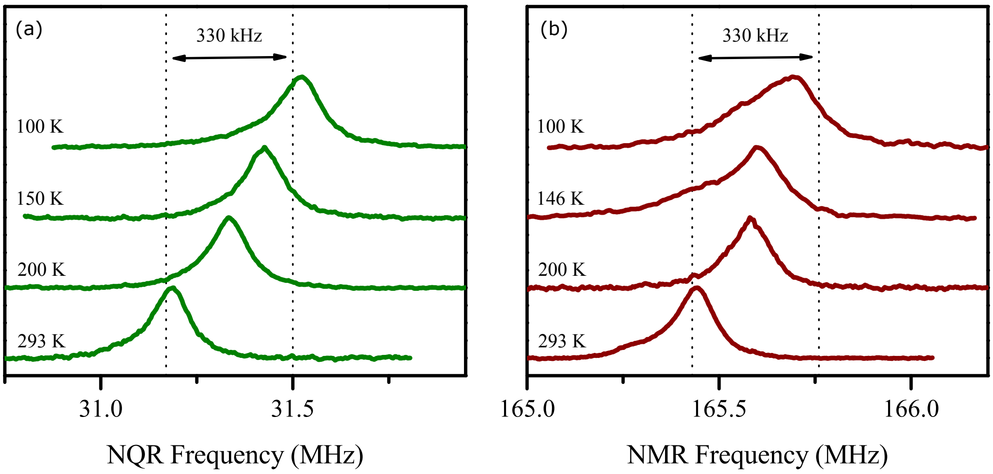

Figure 4.13: Temperature dependence of the NQR (a) and NMR high frequency satellite spectra (b) of planar ^{63}Cu in $YBa_2Cu_3O_7$.

netic field of about 11.7 T using NMR.

4.3.1 NQR measurements

The electric field gradient of planar Cu is almost axial symmetric ($\eta \approx 0.01$), thus, the position of the NQR spectrum measures directly the quadrupole frequency $^{63}\nu_{\mathrm{Q}}$ which is determined by the largest EFG principle value V_{ZZ}, cf. Eq. (2.12). The width of the observed line measures $^{63}\Lambda_{\mathrm{Q}}$[1], i.e., the variation of the largest EFG principle value ΔV_{ZZ}.

In Fig. 4.13 (a) the temperature dependence of the NQR spectrum is shown. The line shifts linearly to lower frequencies by increasing the temperature and the corresponding quadrupole splitting $^{63}\nu_{\mathrm{Q}}$ decreases by about 330 kHz from 300 K to 100 K, cf. Fig. 4.14 (a). A point ion model was previously used to account for the temperature dependence[2] [Brinkmann, 1992; Mali et al., 1987]. The NQR lineshape is described by a Lorentzian line and the corresponding FWHM $^{63}\Lambda_{\mathrm{Q}}$ increases linearly by about 17 kHz from 300 K to 100 K, cf. Fig. 4.14 (b).

4.3.2 Magnetic field B_0 parallel to the crystal c-axis

The same sample was also investigated with NMR with the magnetic field along the crystal's c-axis ($c \parallel B_0$). In this direction, three lines ($n = -1, 0, 1$) are obtained for planar ^{63}Cu

---

[1] The magnetic linewidth observed with NMR which includes the magnetic field independent dipole-dipole broadening is negligibly small in comparison to the quadrupole distribution $^{63}\Lambda_{\mathrm{Q}}$.

[2] The analysis is, however, questionable, since a point ion model is rather crude since even with sophisticated ab-initio calculations, concurring results were not easily obtained for the planar Cu EFG [Hüsser et al., 1998; Renold et al., 2001].

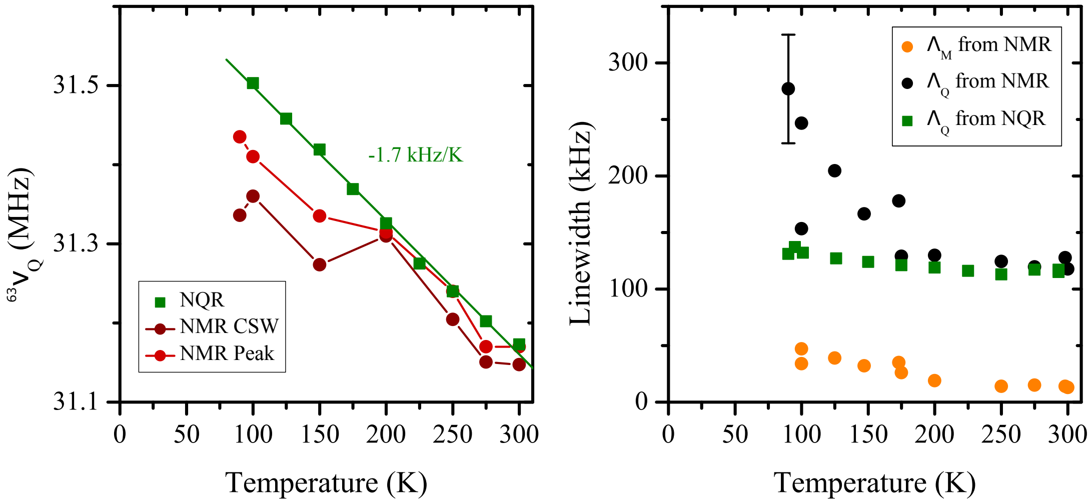

Figure 4.14: Comparison of the temperature dependent quadrupole frequency $^{63}\nu_Q$ and its distribution $^{63}\Lambda_Q$ of planar ^{63}Cu in $YBa_2Cu_3O_7$ with and without an external magnetic field. (a) Planar ^{63}Cu quadrupole frequency as obtained by NQR and NMR. For NMR, $^{63}\nu_Q$ was determined by the center of spectral weight (CSW) as well as the peak position of the respective lower and upper satellite transitions. (b) Planar ^{63}Cu quadrupolar linewidth $^{63}\Lambda_Q$ (FWHM) obtained by NQR (green) and NMR (black). Also shown is the width of the NMR CT which measures the magnetic distribution Λ_M (orange). The large error bar at 90 K represents the lower and upper bound due to a large plateau of the lower ST.

which are described by a sum of a magnetic and quadrupolar contribution: $^{63}\nu_{\text{mag}} + n \cdot {}^{63}\nu_Q$, cf. Sec. 2.2.1. The change of the magnetic part with temperature is only minor, i.e., by about 20 kHz from 300 to 100 K, and the magnetic broadening $^{63}\Lambda_M$ is much smaller than the quadrupolar distribution, cf. Fig. 4.14 (b), and can be neglected. Thus, the satellite position and width is expected to change with temperature in the same way as the NQR line.

In Fig. 4.13 (b), the temperature dependence of the high frequency satellite spectrum is shown and reveal that first the temperature dependent shift of the line is smaller than for NQR, cf. Fig. 4.13 (a), and second, a large line broadening occurs at low temperatures. The quadrupole frequency $^{63}\nu_Q$ obtained by the difference of the center of spectral weight (first moment) of the upper and lower satellite is compared with NQR[1] in Fig. 4.14 (a). Below 200 K, there is a substantial deviation of $^{63}\nu_Q$ measured without and with an external magnetic field. Note, that the discrepancy is smaller but still significant if the peak value is taken. Such a behavior can simply be due to a misalignment of the sample, i.e., an offset by 3° would explain the lowering of $^{63}\nu_Q$. However, the mechanism which rotates the

---

[1] There is no significant deviation between the peak position and the center of spectral weight for the NQR spectra.

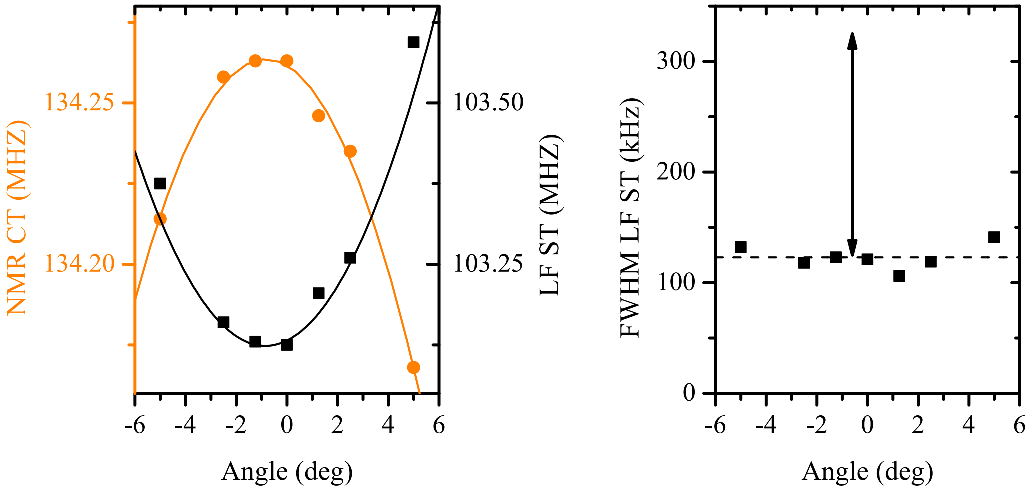

Figure 4.15: Angular (polar angle) dependence of the planar ^{63}Cu CT (orange) and lower ST (black) in (a) as well as satellite linewidth in (b) at 300 K. A parabolic fit describes the CT (orange line) which is used with the angular dependence of the first order quadrupole part, cf. Eq. (2.6), to describe the lower ST (black line) with the parameters $^{63}\nu_{\mathrm{Q}} = 31.14$, $\eta = 0$ and an offset angle $\theta_0 = 1°$. The plot in (b) has the same scale as in Fig. 4.14 (b) and the arrow indicates the changes of the NMR quadrupole linewidth with temperature. The dashed line is a guide to the eye.

sample would have to be temperature dependent. The materials magnetic susceptibility is temperature dependent, but can be excluded since it is largest along the chosen orientation ($c \parallel B_0$). Thus, there is no associate torque which would rotate the sample. Unfortunately, the alignment cannot be checked at low temperatures and thus, it cannot be proven that the measurements are performed along the main principle axis of the Cu EFG (Z-axis) below 200 K[1]. Clearly, the observed discrepancy could also be explained by a temperature and field dependent EFG, i.e., V_{ZZ} changes below 200 K in a magnetic field. Consulting Eq. (2.15), $^{63}\nu_{\mathrm{Q}}$ is expected to decrease either if holes are removed from the Cu or O orbitals, or if charges between the orbitals redistribute, i.e., holes migrate from Cu to O. However, whether the magnetic field is able to reorganize charges have to be seen. Nevertheless, if such a charge redistribution varies spatially, the quadrupolar linewidth will be affected.

At high temperatures, the obtained satellite linewidth agrees with the observed spectral distribution obtain by NQR, cf. Fig. 4.14 (b). However, below 200 K, the linewidth starts to deviate from the NQR linewidth, e.g., at 90 K the quadrupolar width measured without and with a magnetic field is 130 kHz and 275 kHz, respectively [Reichardt et al., 2016]. Note, that the discrepancy was also obtained in experiments with a (different) micro-sample of $YBa_2Cu_3O_7$ for the pressure cell experiments, cf. Sec. 4.2, and there are some scatters in

---

[1] This can either be caused by a misalignment of the sample with the field or by a small rotation of the EFG.

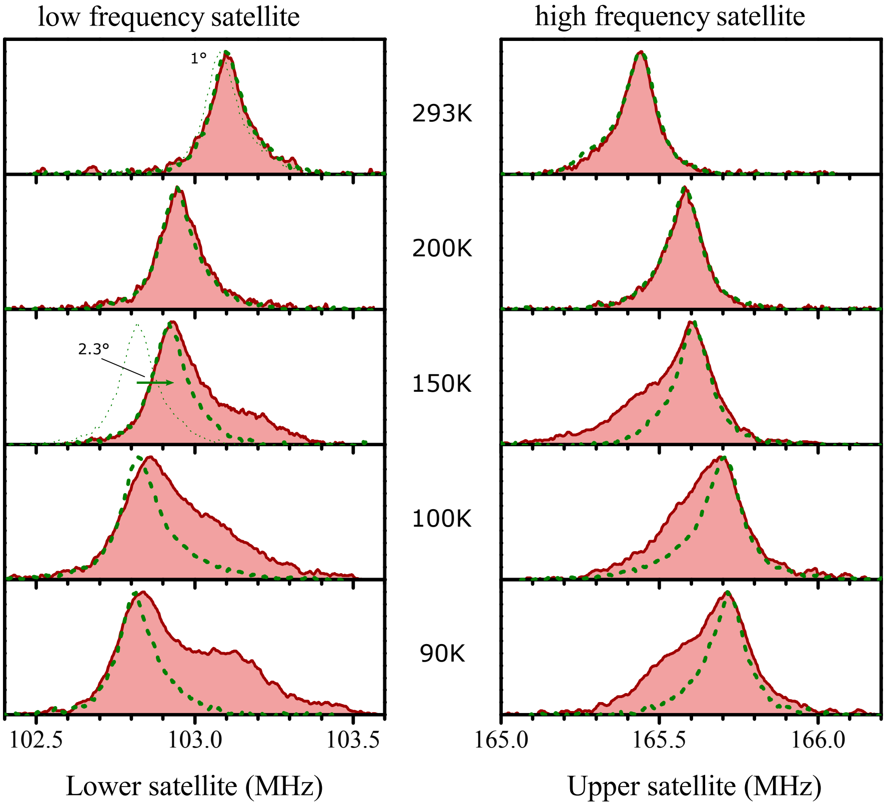

Figure 4.16: Comparison of the temperature dependence of the low (left) and high (right) frequency NMR satellite transitions (red) of planar ^{63}Cu in $YBa_2Cu_3O_7$ for $c \parallel B_0$ with the simulated spectrum based on the quadrupolar distribution measured with NQR (thick green lines). For improved comparison, it was corrected for the observed deviation of the quadrupole frequencies by a polar offset angle β_0 such that the high quadrupole frequencies fit. Above 200 K the deviation is small (thin green line at 293 K) and was corrected by $\beta_0 = 1°$. Below 200 K, $\beta_0 = 2.3°$ was used to lift the offset, cf. low frequency satellite at 150 K.

repeated experiments. Magnetic impurities cannot account for the increasing linewidth since they would affect the CT as well which is not observed. Furthermore, in Fig. 4.15, the position of the CT and low frequency ST as well as the linewidth of the ST are shown as a function of a small (polar) offset angle. In comparison to the CT, the ST changes largely under rotation which as mentioned before could correct the observed discrepancy of $^{63}\nu_Q$ at low temperatures. However, the corresponding quadrupolar linewidth does not change significantly and the low temperature broadening must be due to the presence of a magnetic field.

In Fig. 4.16, the temperature dependence of the low and high frequency ST are shown in comparison to the simulated spectrum based on the quadrupolar distribution observed with NQR and the magnetic shift measured by the NMR CT, cf. Sec. 2.2. Note, that the discrepancy between the quadrupolar frequencies was corrected for improved comparison of the patterns by introducing a polar offset angle β_0. The angle was set such that the spectral contribution corresponding to large quadrupole frequencies (sharp NMR edges) agree with the data observed by NQR, i.e., above and below 200 K, the angle β_0 was set to 1° and 2.3°, respectively, cf. Fig. 4.16.

At high temperatures, the satellite spectra measured in an external magnetic field agree with the spectra observed without a magnetic field as expected. Below 200 K, the pattern of the STs reveal a dramatic discrepancy with the almost unchanged NQR line. While the spectral weight corresponding to high quadrupole frequencies[1] remains similar to the NQR line, an additional spectral feature appears towards low quadrupole frequencies. Note, that two lines with a quadrupolar distribution given by NQR cannot explain the pattern, rather a distribution is encountered.

The pattern at low temperatures is similar to what has been predicted for incommensurate charge density wave systems of short coherence [Blinc, 1981] which has also been measured, for instance, in the charge density wave system $NbSe_3$ [Ross et al., 1986]. In fact, the observed large modification of the planar Cu quadrupolar pattern is similar to what has been observed in underdoped $YBa_2Cu_3O_{6.54}$ (ortho II) in very high magnetic fields [Wu et al., 2011] which was interpreted as a unidirectional modulation of the planar charge density, however, at much lower temperatures (< 60 K).

Although the effect is large, i.e., a factor of two in the quadrupolar width, it can only be observed due to the high quality of the crystal which gives a very narrow quadrupole distribution at 300 K (≈ 115 kHz) and was not recognized in samples with a width larger than 250 kHz. In fact, such a initial linewidth conceal the magnetic field induced broadening of about 160 kHz at 100 K. For instance, an field induced broadening of that size would increase the width by only 38 kHz in the slightly underdoped material $YBa_2Cu_3O_{6.9}$ with a room temperature linewidth of about 300 kHz which is, however, in good agreement to what has been found at 100 K (330 kHz), cf. Fig. 4.8. Furthermore, compared to 300 K, a small discrepancy between NQR and NMR at 18 kbar and low temperature is observed in that compound, cf. Fig. 4.9 which may indicate that pressure enhance field induced broadening effect.

To conclude, it was shown that the magnetic field induces spatial variations in V_{ZZ} the largest component of the planar Cu EFG . The EFG variation can be interpreted as a spatial variation of planar charges and constitute the first observation of a relation between magnetic field and planar charge variation in slightly overdoped $YBa_2Cu_3O_7$. Whether, the magnetic field changes the average orbital hole contents cannot be determined conclusively.

---

[1] The lower and upper edge of the low and high frequency ST, respectively.

4.3.3 Magnetic field B_0 perpendicular to the crystal c-axis

In the last section, the largest Cu EFG component V_{ZZ} was measured with the magnetic field along the c-axis of the crystal. For an axially symmetric EFG tensor ($\eta = 0$), the two other EFG compontents are determined by Laplace equation, i.e., $V_{XX} = V_{YY} = -V_{ZZ}/2$, and are measured with the magnetic field perpendicular to the c-axis ($c \perp B_0$) . Clearly, a spatial variation of the largest EFG component ΔV_{ZZ} will result in a distribution $\Delta V_{XX} = \Delta V_{YY} = \Delta V_{ZZ}/2$ of the other two components. Thus, in first approximation, the observed quadrupolar splitting between the three Cu lines in $c \perp B_0$ will be $\nu_{\mathrm{Q}}/2$ and the satellite linewidth will be half of the width observed by NQR or NMR in $c \parallel B_0$. However, the CT and ST are not described satisfactorily by first order corrections in this orientation. In fact, in a magnetic field of 11.7 T, the planar ^{63}Cu CT will be shifted due to second order quadrupolar effects (≈ 1.4 MHz) and the STs are significantly affected in third order (≈ 80 kHz), cf. Tab. 2.1.

A small planar Cu EFG asymmetry η ($V_{XX} \lessapprox V_{YY}$) has been measured in $YBa_2Cu_3O_{7-\delta}$ [Pennington and Slichter, 1990] which lifts the degeneration within the plane and defines the directions of V_{XX} and V_{YY}. Thus, depending on the orientation of the magnetic field in respect to the EFG's X-axis measured by the azimuthal angle α, the central and satellite transitions encounter another shift of $\eta(2\nu_{\mathrm{Q}}^2/3\nu_{\mathrm{mag}})\cos 2\alpha$ and $\eta(\nu_{\mathrm{Q}}/2)\cos 2\alpha$, respectively. The orientation of the principle axis system of the planar Cu EFG is given by the symmetry axis (c-axis) and the direction of the planar Cu-O bonding orbitals, i.e., along the crystal's a and b-axis. The planar Cu EFG asymmetry was thus interpreted as due to the (small) orthorhombicity of the crystal, i.e., the distance between planar Cu and O is larger along the b than along the a-axis. Since the crystal is twinned, i.e., both unit cell axis a and b are equally encountered along a particular planar Cu-O bond direction, both (in-plane) EFG components can be simultaneously measured, see also Sec. 5.1 for details. The investigated sample $YBa_2Cu_3O_7$ is cut such that the crystal's a and b-axis are parallel to the sample edges, thus, α is experimentally measured with respect to one of the sample edges. However, due to twinning the determined angle α is only valid for half of the Cu EFG's, the other half is rotated by 90°.

In Fig. 4.17 (b), the high frequency ST with the magnetic field along one of the sample edges ($\alpha = 0$) is shown. A spectral distribution is revealed with two peaks which are symmetric about the position of the satellite for an axially symmetric EFG ($\eta = 0$)[1]. As mentioned before, the two peaks are expected for an asymmetric planar Cu EFG in a twinnned crystal and from the distance of the peaks and the quadrupole frequency obtained by NQR, η can be

---

[1] The position of the high frequency ST for an axially symmetric EFG is given by the sum of the magnetic as well as the first and third order quadrupole part: $\nu_{(3/2\leftrightarrow 1/2)} = \nu_{\mathrm{mag}} + \nu_{\mathrm{Q}}/2 - 3\nu_{\mathrm{Q}}^3/64\nu_{\mathrm{mag}}^2$.

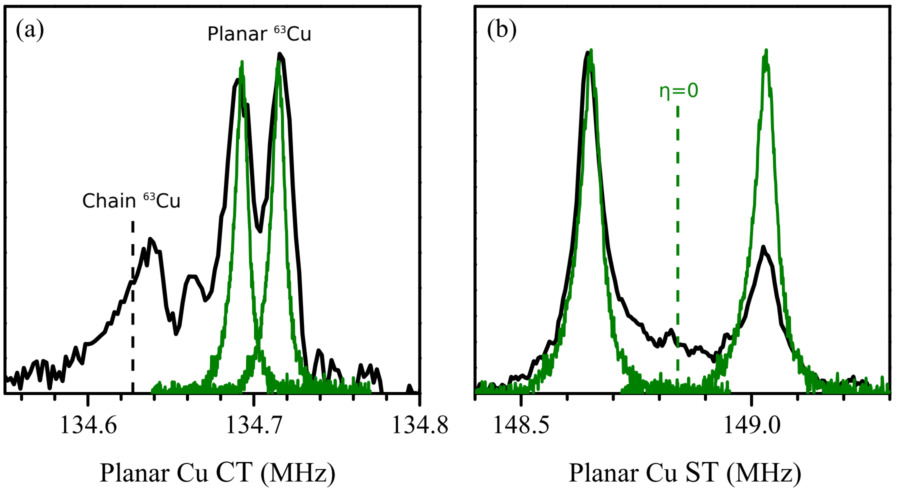

Figure 4.17: Planar ^{63}Cu central (a) and high frequency satellite transition (b) in $\sigma \parallel B_0$ at 300 K. Also shown are the simulated spectra (green lines) based on the quadrupolar distribution measured with NQR with $\eta = 0.0123$ and $K_\perp = 0.733\%$ and an offset angle $\beta_0 = 1°$ for an equally twinned sample. The dashed line in (a) corresponds to the expected position of the chain ^{63}Cu CT. The dashed green line in (b) represents the satellite position for an axially symmetric EFG.

calculated. The obtained EFG asymmetry $\eta = 0.012$ agrees with what has been determined before [Pennington and Slichter, 1990].

The corresponding CT in this field direction is shown in Fig. 4.17 (a) and reveals a complex pattern. Using the quadrupolar distribution obtained by NQR (Sec. 4.3.2), the calculated asymmetry $\eta = 0.012$ and the magnetic shift from literature ($K = 0.73\%$) [Pennington and Slichter, 1990], the NMR spectra can be calculated, cf. Sec. 2.2. The two pronounced peaks of the CT as well as the peaks of the STs can be explained by an EFG asymmetry in a twinned sample, cf. green lines in Fig. 4.17. The additional spectral distribution to lower frequencies in Fig. 4.17 (a) is likely due to the CT of the chain ^{63}Cu which expected position [Pennington and Slichter, 1990] is indicated.

It is apparent in Fig. 4.17 (b), that the two satellite peaks have different intensities, i.e., the ratio of the peak integrals is about 1.8. This is not simply explained since twinning occurs equally, i.e., along the magnetic field direction the a and b axis are encountered with equal likelihood, cf. Sec. 3.3.1. Revisiting an early literature spectrum [Pennington, 1989], an analog intensity mismatch is found which was not further discussed probably due to the rough resolution of the spectrum, cf. Fig. 4.18 (b). Furthermore, the simulated ST spectrum in Fig. 4.17 (b) do not cover the observed one, i.e., there is substantial intensity between the peaks. This means that a distribution of planer Cu EFG's is present. Both findings are not in agreement with the interpretation of the EFG asymmetry as due to orthorhombicity and

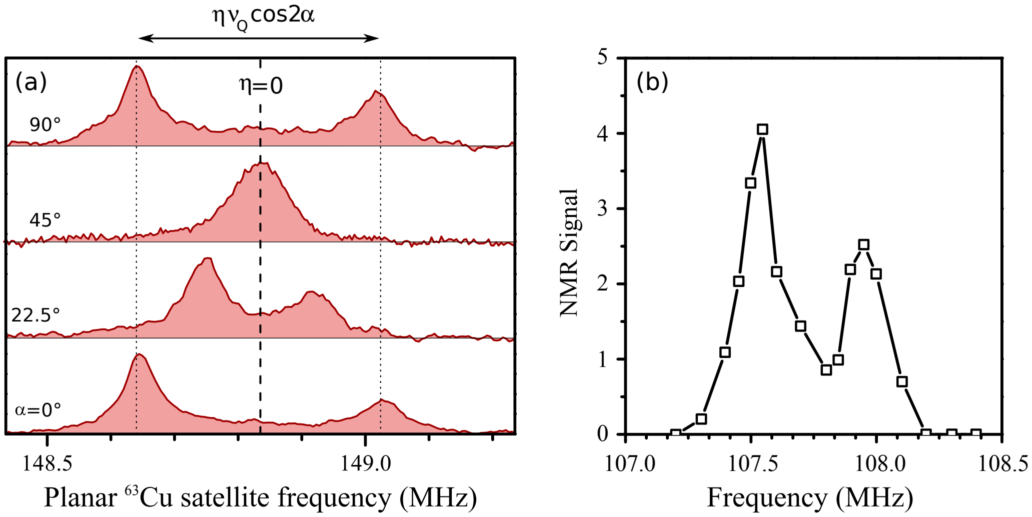

Figure 4.18: (a) Planar ^{63}Cu high frequency satellite transition for various in-plane angles α ($c \perp B_0$). The dashed line represent the position of the satellite for an axially symmetric EFG and the dotted line mark the maxima for $\eta = 0.012$ and $^{63}\nu_\mathrm{Q} = 31.17\,\mathrm{MHz}$, i.e., for $\alpha = 0$ and 90°. (b) ^{63}Cu high frequency satellite transition measured in a lower magnetic field ($B_0 = 8.12\,\mathrm{T}$) reproduced from [Pennington, 1989].

thus must be questioned.

In Fig. 4.18 (a), the planar Cu ST is shown for different (in-plane) angles α. The observed spectrum for $\alpha = 0°$ could also be regarded as a powder pattern, however, under rotation α the peaks become closer, in particular, the peaks overlap at $\alpha = 45°$ and are at the same position at $\alpha = 90°$ as expected for a well defined EFG principle axis system. Thus, the spectrum for $\alpha = 0°$ cannot be due to a random (in-plane) distribution of Cu EFG's with fixed principle components[1]. Since the distribution ΔV_{ZZ} measured with NQR or NMR with $c \parallel B_0$ is symmetric and do not show any anomalies at 300 K, the satellite pattern for $c \perp B_0$ reveal a distribution of the planar Cu EFG asymmetry parameter η, i.e., in addition to the most often encountered Cu EFGs (peaks) there are also Cu EFGs with a smaller and even vanishing asymmetry.

Most unusual is the observation that the spectrum for $\alpha = 0°$ and 90° are similar regarding their intensities. Spectral weight below and above the symmetry line (position of the satellite for $\eta = 0$) represent in good approximation the number of planar Cu nuclei experiencing the EFG's X-axis and Y-axis along the magnetic field direction, respectively. Thus, the different peak intensities at $\alpha = 0°$ allow to distinguish planar Cu nuclei by their orientation of the EFG principle axis system. Since the EFG is supposed to be fixed to the local crystal structure, a rotation of the magnetic field by 90° must exchange the intensities, i.e., it is expected to

---

[1] Still a special distribution of angles is possible but unlikely.

encounter more planar Cu nuclei with their Y-axis in the new field direction. However, the ratio of the peak intensities[1] is only slightly smaller for $\alpha = 90°$ (≈ 1.6) than for $\alpha = 0°$ (≈ 1.8), but far from inverse (0.6) as expected[2]. From this, it must be concluded that the EFG asymmetry is not solely given by the crystal structure and thus, the orthorhombic model used to explain the planar Cu EFG asymmetry is at least not complete. Rather the external magnetic field direction seems to affect the EFG asymmetry. In the previous subsection it was shown that the magnetic field is capable to vary the spatial planar charge distribution. The observation that the planar Cu EFG asymmetry is also affected by a magnetic field reveals that the arrangement of planar charges changes with the direction of the magnetic field. Since a charge variation in the planar Cu $d_{x^2-y^2}$ orbital do not generate an EFG asymmetry at the Cu site, the planar O orbitals could be involved. Clearly, the intensity ratios of both orientations are not equal, thus, there is an contribution to the EFG which is tied to the lattice and might be due to the orthorhombic structure.

In summary, the magnetic field affects the spatial distribution of the largest Cu EFG component V_{ZZ}, but also the Cu EFG asymmetry is influenced. Thus, the planar charge density variation is affected by a magnetic field and at least partly involve the planar O orbitals. These findings demonstrate that the magnetic field couples to the planar Cu EFG via the distribution of planar charges. Furthermore, it supports the previous finding, cf. Sec. 4.2, that the Cu EFG in YBCO is affected by low energy excitations, i.e., by pressure and temperature.

4.4 Conclusion

To conclude, ^{63}Cu NMR and NQR experiments were performed on the stoichiometric systems $YBa_2Cu_4O_8$ and $YBa_2Cu_3O_7$ as well as on the slightly disordered material $YBa_2Cu_3O_{6.9}$ up to 29 kbar. Pressure, but also temperature affect the average planar Cu EFG in these materials. The spatial variation of the Cu EFG increases dramatically with pressure and is comparably to chemically induced planar charge disorder. These modifications of the planar Cu EFG with pressure are interpreted as a charge redistribution accompanied with a large spatial distribution of planar charges.

Furthermore, the planar Cu EFG was investigated without and with a magnetic field in the overdoped $YBa_2Cu_3O_7$ and it was found that the magnetic field influences the planar Cu EFG, i.e., the spatial variation of the largest Cu EFG component V_{ZZ} and the EFG's asymmetry parameter η. These findings indicate a field induced planar oxygen charge variation and they

---

[1] The ratio of the intensities below and above the symmetry ($\eta = 0$) line was used, but also the ratio of the intensities of the sharp peak edges avoiding the uncertainties between the peaks.

[2] On going efforts proved that the spin echo decay cannot account for the discrepancy.

constitute the first direct observation of a relation between planar charges and an external magnetic field in *overdoped* $\mathrm{YBa_2Cu_3O_{6+y}}$. Since superconductivity is not suppressed in this doping range and the observed relation becomes apparent far above T_c, a direct interaction between the planar charge distribution and the magnetic field is supported rather than an indirect competing mechanism as often assumed.

Clearly, with the performed experiments, the origin of the broad quadrupolar linewidth of the planar nuclei in the cuprates cannot be proven. However, if such small perturbations of the system as from moderate pressures and magnetic field can induce static charge variations, chemically induced disorder will also trigger large static charge variations. Thus, the cuprates may have a rather fragile planar electronics which can be disturbed, e.g., by pressure, temperature, magnetic fields and chemical doping, leading to the large observed planar Cu quadrupole distributions.

Chapter 5

Pressure induced charge ordering at planar oxygen

5.1 Planar Cu and O satellite line splitting and the role of the crystal's orthorhombicity

For some doping levels in YBCO, the planar Cu and O satellite spectra reveal a double peak pattern which are exemplary illustrated in Fig. 5.1. The investigation of this feature in a single crystal of $\mathrm{YBa_2Cu_3O_{6.9}}$ is the main object of this chapter. The pattern is commonly interpreted as from two lines due to the crystal's orthorhombicity. In the following, the characteristic of NMR measurements on a twinned orthorhombic single crystal will be introduced and important aspects will be highlighted.

The $\mathrm{CuO_2}$ plane is doped in $\mathrm{YBa_2Cu_3O_{6+y}}$ by introducing oxygen into the CuO_y chain layers and by this the symmetry of the crystal structure changes from tetragonal ($y < 0.4$) to orthorhombic ($y > 0.4$) [Conder, 2001]. As a consequence, the planar Cu-O bond length is larger along the CuO chain direction (b-axis) than along the direction with empty chain O sites (a-axis), cf. the crystal structure in Fig. 2.1 (a). As mentioned before, crystals of orthorhombic YBCO[1] are twinned, i.e., the a and b-axis alter periodically along a chosen planar Cu-O bond direction. A representative domain of the $\mathrm{CuO_2}$-plane is illustrated in Fig. 5.2 where the orthorhombicity $\epsilon = (b-a)/(b+a)$ is exaggerated by a factor of about 20 for better visualization. For the reasoning in this chapter, it is important to emphasize that orthorhombicity as well as crystal twinning are determined by chemistry, i.e., high energies are required to change these structural features substantially. For instance, the difference in

---

[1] Also $\mathrm{YBa_2Cu_4O_8}$ exhibit a orthorhombic crystal structure, although the material consists of double CuO chain layers which are perpendicular to each other.

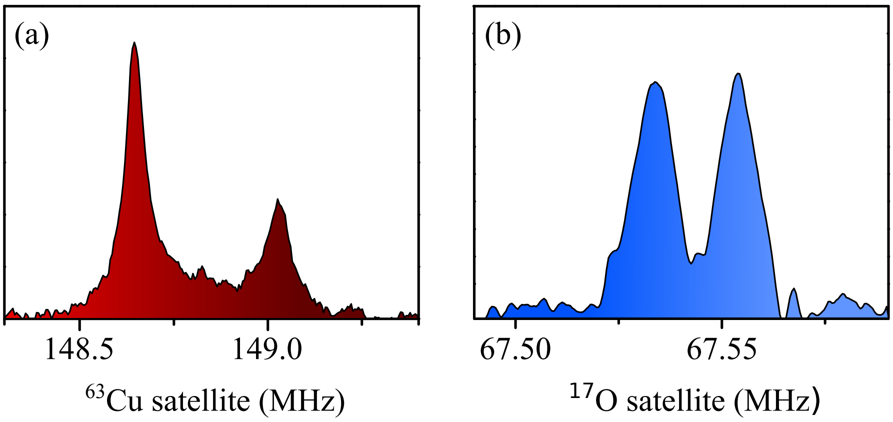

Figure 5.1: Planar Cu and O satellite line splitting at ambient pressure. (a) Planar ^{63}Cu ST ($3/2 \leftrightarrow 1/2$) in $\sigma \parallel B_0$ reveals two differently intense peaks with a distance of about 300 kHz. (b) Planar ^{17}O ST ($-1/2 \leftrightarrow -3/2$) in $c \parallel B_0$ shows two equaly intense lines with a distance of about 20 kHz. Spectra in (a) and (b) were obtained in $YBa_2Cu_3O_7$ and $YBa_2Cu_3O_{6.9}$, respectively.

the axis lengths is rather constant for the applied pressure in this thesis [Calamiotou et al., 2009], cf. Fig. 5.3 (a), and twinning is only removed by applying uniaxial pressure at high temperatures [Liang et al., 2000] - a thermodynamically instable phase.

From the NMR perspective there is only one planar Cu site which is customarily denoted as Cu(2). The 4-fold rotational symmetry in respect to the crystal's c-axis of the planar Cu position is broken by the crystal's small orthorhombicity. Thus, the orthorhombic contribution to, for instance, the planar Cu EFG will be different along the a or b-axis. Indeed, a small EFG asymmetry ($\eta = 0.012$) has been found experimentally in these materials with the corresponding principle axis along the planar Cu-O bond direction [Pennington and Slichter, 1990]. Thus, in a twinned crystal there are two types of planar Cu EFGs present which are switched by 90° to each other, cf. Fig. 5.2. For $c \parallel B_0$, these two EFG orientations cannot be distinguished, but with the magnetic field along either one planar Cu-O bond direction ($\sigma \parallel B_0$), NMR can measure both EFG components V_{XX} and V_{YY} simultaneously.

For planar O the situation is different. The largest EFG principle value is found along the Cu-O bond direction and since the crystal lacks rotational symmetry about this axis, the EFG asymmetry is substantial $\eta \approx 0.23$. The smallest principle value is found along the crystal's c-axis and the intermediate principle value is found within the CuO_2 plane but perpendicular to the respective Cu-O bond direction. Due to the crystal's orthorhombicity, there are two chemical sites: O(2) with the Cu-O bond along the a-axis and O(3) with the bond along the b-axis. Note, that with the magnetic field along any of the O EFG principle axis, NMR can measure both sites simultaneously in a twinned crystal, cf. Fig. 5.2. Indeed, two distinct planar O EFGs have been measured which were interpreted as due to

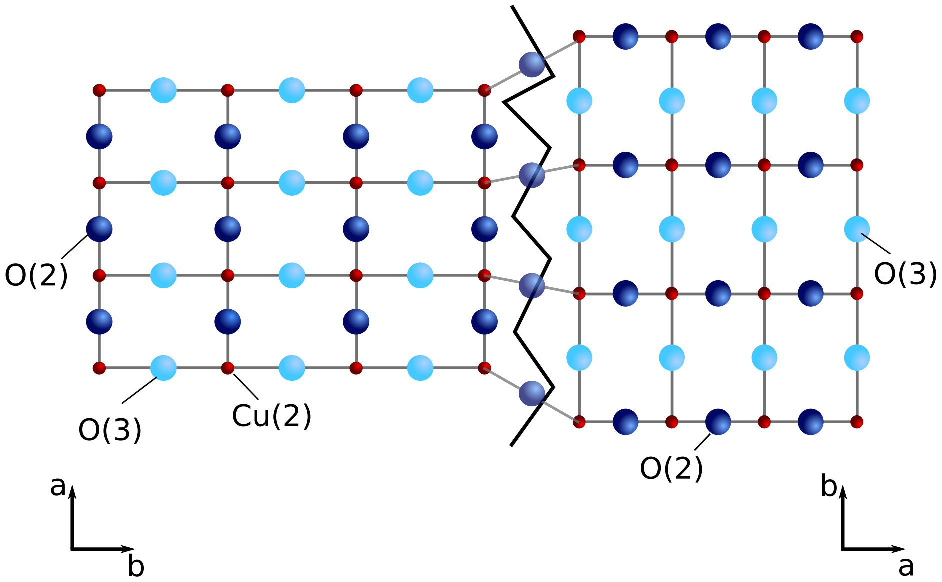

Figure 5.2: Twinned, orthorhombic CuO_2 plane and its implications for the planar Cu and O EFG. There is one planar Cu site - Cu(2) - and the EFG at that nuclear site is almost axially symmetric and the largest principle value V_{ZZ} is obtained in $c \parallel B_0$. The crystal's orthorhombicity breaks the planar symmetry and due to twinning, both related planar Cu EFG components $V_{YY} \geq V_{XX}$ can be simultaneously measured with the magnetic field along either one Cu-O bond direction ($\sigma \parallel B_0$), e.g., left of the twinning boundary along the a-axis. The asymmetry of the planar O EFG is substantial and the largest EFG component is measured with the magnetic field along the Cu-O bond, the smallest component is obtained for $c \parallel B_0$ and the intermediate one is obtained with the field perpendicular to both, the crystal's c-axis and the Cu-O bond direction. Two O sites - O(2) and O(3) - can be distinguished due to the orthorhombicity, and the EFG components of both O sites are measured simultaneously for each field orientation in a twinned crystal. For improved visualization the orthorhombicity is exaggerated by a factor of about 20. Also indicated by different colors is a charge variation at planar O which lead to the same planar Cu and O EFG symmetries as that of a orthorhombic CuO_2 plane.

orthorhombicity [Pennington and Slichter, 1990].

On the other hand, it has not been proven that the observed spectral features obtained for planar Cu and O are directly related to the orthorhombicity of the crystal, i.e., a result from the geometric arrangement of the atoms. For instance, while first principle calculations of the EFG for the chain Cu agree well with experiment, concurring results for the planar Cu EFG are not easily obtained and more sophisticated models are required [Hüsser et al., 1998; Renold et al., 2001]. There are also some indications that orthorhombicity does not play such a major role as expected. In Sec. 4.3.3 it was shown that the planar Cu asymmetry η is only partly related to the lattice and largely affected by the magnetic field direction. Furthermore, it was speculated, that the planar O double peak pattern observed for $c \parallel B_0$ are due a commensurate charge density variation [Haase and Slichter, 2003], cf. differently

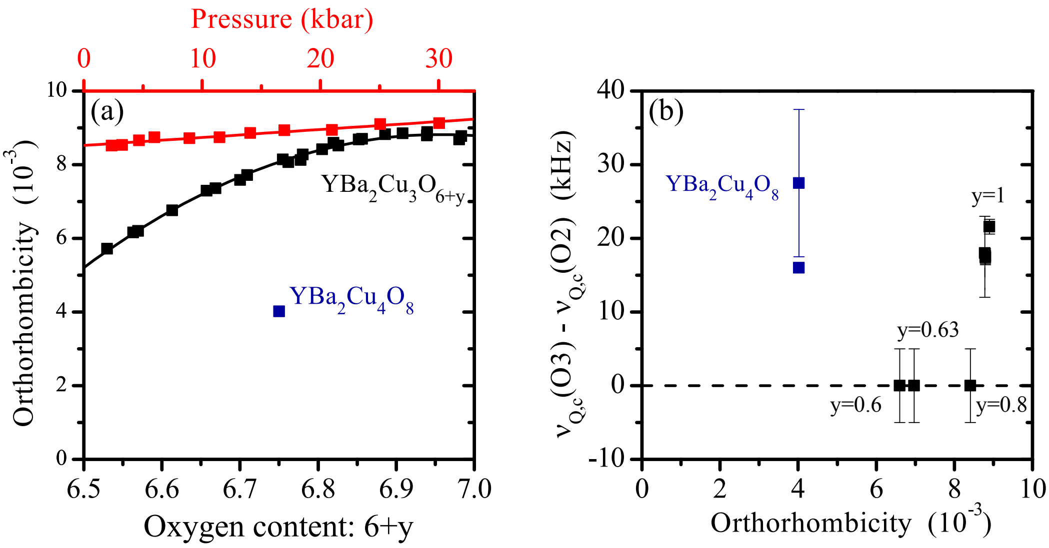

Figure 5.3: (a) Crystal's orthorhombicity $\epsilon = (b-a)/(b+a)$ as a function of the oxygen content $6+y$ in $YBa_2Cu_3O_{6+y}$ (black), as well as of pressure in $YBa_2Cu_3O_{7-\delta}$ (red). Also shown is ϵ of $YBa_2Cu_4O_8$ (blue). The lines are guide to the eye. Data taken from Calamiotou et al. [2009]; Conder [2001]; Karpinski et al. [1988]. (b) Planar ^{17}O satellite line splitting measured in $c \parallel B_0$ as a function of the crystals orthorhombicity. Data from Mangelschots et al. [1992]; Takigawa et al. [1989, 1991]; Yoshinari et al. [1990]; Zheng et al. [1992].

colored O sites in Fig. 5.2. In both cases, the orthorhombicity may be affecting the charge density variation but need not to be the origin of the observed features. The two chemical sites O(2) and O(3) differ only in their bond length and the related quadrupole frequencies should thus be a measure for the orthorhombicity. In this sense it is suspicious, that O satellite double peak patterns have only been observed with the magnetic field along the Cu-O bond as well as along the crystal's c-axis where the largest and smallest EFG comment is measured, but not along the third principle axis, i.e., in this direction O(2) and O(3) are not distinguishable. Furthermore, in Fig. 5.3 (b), the difference of the quadrupole frequencies of O(2) and O(3) observed from the NMR satellite line splitting is plotted for various compounds as a function of the respective orthorhombicity $\epsilon = (b-a)/(b+a)$. The difference between O(2) and O(3) obtained for the stoichiometric materials $YBa_2Cu_3O_7$ and $YBa_2Cu_4O_8$ is of the same size, although the respective orthorhombicities ϵ differ by a factor of two. In addition, the satellite line splitting is absent for the intermediate doping levels. Note, that this is not an issue of resolution as the O satellite linewidth for the doping $y = 0.63$ is only slightly larger than for the fully doped material [Takigawa et al., 1991]. Clearly, a relation between the difference of the quadrupole frequencies and the orthorhombicity is missing. The splitting rather seems to be a feature of the well ordered materials[1]. These findings indicate that the orthorhombicity plays a subordinate role for the planar EFG.

To clarify the origin of the planar satellite pattern, the oxygen exchanged sample $YBa_2Cu_3O_{6.9}$ which reveals all features commonly attributed to the orthorhombicity was investigated by applying moderate pressures, i.e., pressures high enough to affect the electronic properties but low enough to leave the crystallographic structure and crystal twinning unchanged. The obtained results will be presented in the following sections.

5.2 Charge order from planar Cu NMR

The pressure and temperature dependence of the three planar ^{63}Cu transitions in a single crystal of $YBa_2Cu_3O_{6.9}$ have been measured with the magnetic field along either one Cu-O bond direction ($\sigma \parallel B_0$). The alignment of the Cu-O bond with the external magnetic field was achieved using the angular dependence of the planar O ST, cf. Sec. 3.2.3 for details. In this section the results of the NMR measurements will be presented and discussed. The respective planar Cu NQR as well as NMR measurements in $c \parallel B_0$ will be used for the interpretation of the data and can be found in Sec. 4.2.4.

The two compounds $YBa_2Cu_3O_7$ and $YBa_2Cu_3O_{6.9}$ are similar, i.e., the observed lines are found at the same positions, but they are considerably broader in the latter compound. In the particular orientation and magnetic field (11.7 T), it was shown in $YBa_2Cu_3O_7$, that the spectrum related to the planar ^{63}Cu CT is compost of the CT of the chain ^{63}Cu and two peaks which were attributed to the planar ^{63}Cu CT that is affected by two characteristic EFG orientations, cf. Fig. 4.17 (a). In Fig. 5.4, the pressure and temperature dependence of the corresponding spectrum in $YBa_2Cu_3O_{6.9}$ is presented (black). The tail to lower frequencies of the shown spectra can similarly be attributed to the CT of the chain ^{63}Cu and the peak corresponds to planar ^{63}Cu, however, the two characteristic EFG orientations are not resolved[2]. Pressure and temperature do not shift the peak position largely, i.e., the shift by pressure (temperature) is smaller than 10 kHz (40 kHz). The CT in this orientation is given by a sum of a magnetic and a second order quadrupole part. From the quadrupole frequency obtained by NQR and the EFG asymmetry parameter η which is estimated below, the second order part can be calculated and the magnetic shift $K_\perp$ can be extracted from the position of the CT, cf. Sec. 2.2.1.

In Fig. 5.5, the pressure and temperature dependence of the planar ^{63}Cu high frequency

---

[1] Planar satellite line splittings are also observed in the ortho-phases of $YBa_2Cu_3O_{6+y}$ [Horvatić et al., 1993; Wu et al., 2015]. Unfortunately, the splittings for $c \parallel B_0$ are not shown and thus the materials are not found in Fig. 5.3.

[2] For the analysis of planar ^{63}Cu, the peak of the spectra rather than the first moment is used.

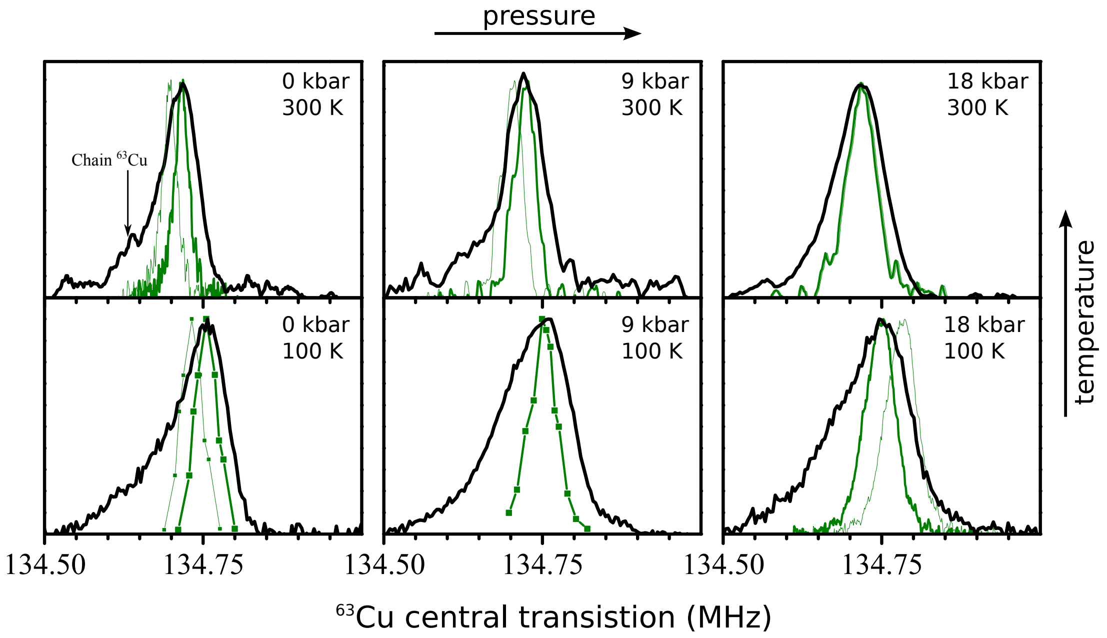

Figure 5.4: Pressure and temperature dependence of the ^{63}Cu CT in $YBa_2Cu_3O_{6.9}$ obtained for $\sigma \parallel B_0$. There is an overlap with the chain ^{63}Cu CT and its position is indicated by an arrow in the plot of 0 kbar and 300 K. Also shown are the simulated spectra (green) based on the assumptions of an orthorhombic, homogeneously twinned crystal. For the simulation the quadrupolar distribution obtained by NQR and the NMR parameters summarized in Tab. 5.1 were used. While the thick green line corresponds to the most often encountered EFG asymmetries, the thin line corresponds to the same EFG but rotated by 90° about the c-axis. See text for details.

ST is shown. From the magnetic part obtained from the CT and the quadrupole frequency determined by NQR, the position of the satellite for an axially symmetric planar Cu EFG ($\eta = 0$) is obtained[1] which is indicated in Fig. 5.5 by dashed vertical lines. Note that uncertainties in the measured shift are covered by the width of the dashed line. At ambient conditions (0 kbar 300 K), the satellite is similar to what was found for $YBa_2Cu_3O_7$, i.e., there is spectral weight below and above the symmetry line with substantially more intensity below. By increasing the pressure to 9 kbar the pattern broadens slightly, but remains similar. At 18 kbar, however, the satellite is symmetric with the peak value close to the expectation of a symmetric EFG. Beside a slight broadening, lowering the temperature at ambient pressure does not change the pattern largely. At 9 kbar 100 K, the line is almost symmetric and the peak is close to the dashed line, similar to what is obtained at 18 kbar 300 K. Eventually, a symmetric line which is clearly shifted above the symmetry line is encountered at 18 kbar 100 K.

---

[1] The position of the high frequency ST for an axially symmetric EFG is given by the sum of the magnetic as well as the first and third order quadrupole part: $\nu_{(3/2\leftrightarrow 1/2)} = \nu_{\mathrm{mag}} + \nu_{\mathrm{Q}}/2 - 3\nu_{\mathrm{Q}}^3/64\nu_{\mathrm{mag}}^2$.

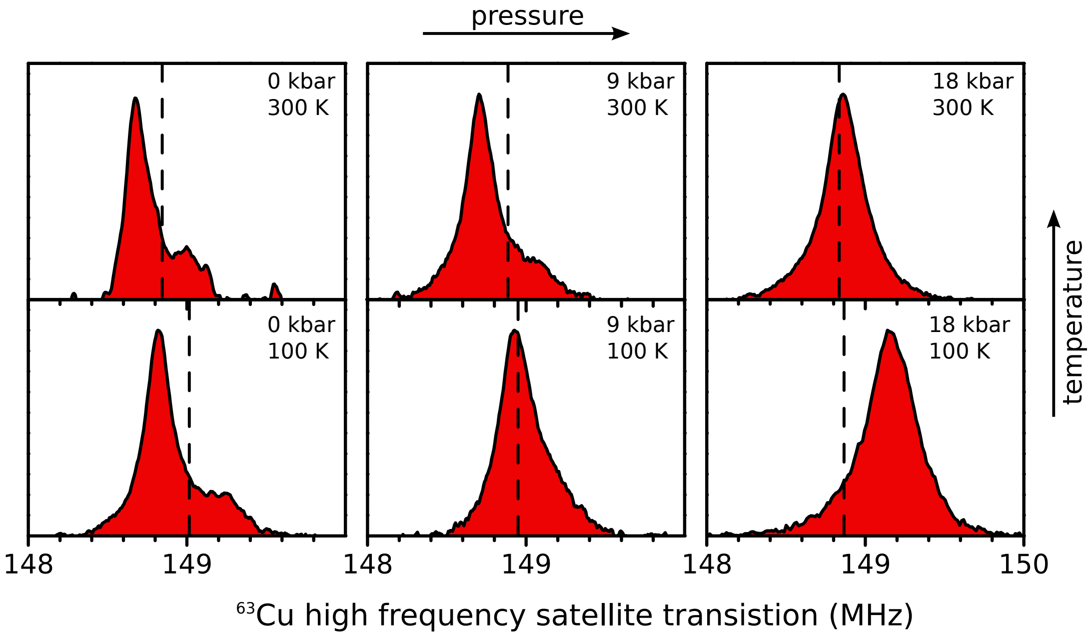

Figure 5.5: Pressure and temperature dependence of the ^{63}Cu ST in $YBa_2Cu_3O_{6.9}$ obtained for $\sigma \parallel B_0$. The dashed line indicate the position of the satellite for an axially symmetric Cu EFG.

To understand the origin of these modifications, the satellite pattern shall be compared with the observed variation of the largest EFG principle value ΔV_{ZZ} measured by NQR. For this, the EFG asymmetry parameter η was estimated from the most intense line of the high and low frequency satellites, cf. Sec. 2.2.1 for details. Using the quadrupole distribution obtained by NQR, the estimated η and magnetic shift $K_\perp$, the three planar ^{63}Cu quadrupolar broadened transitions were calculated, cf. Sec. 2.2. In fact, the fine adjustment of $K_\perp$ and η has been done by matching the three observed planar ^{63}Cu transitions with the simulation[1]. The obtained parameters are summarized in Tab. 5.1 and at ambient pressure they agree well with literature data [Pennington and Slichter, 1990].

In Fig. 5.4 and Fig. 5.6 the obtained spectra are compared with the simulations (thick green lines). Also plotted are the respective lines by a rotation of the EFG by 90° around the c-axis (thin green lines) which is expected for a homogeneous twinned orthorhombic crystal, cf. Sec. 5.1. Note, that the simulation takes only a variation of V_{ZZ} into account, i.e., there is neither an additional magnetic variation nor a variation of η involved. Clearly the CTs shown in in Fig. 5.4 are substantially broadened by second order effects. The depicted STs at ambient pressure as well as the ST at 9 kbar 300 K, cf. Fig. 5.6, are similar to the pattern

---

[1] There is an uncertainty in the shift $K_\perp$ since the distribution of η encountered in the STs is not resolved in the CT spectra which, however, will not change any conclusions drawn below.

Table 5.1: Pressure and temperature dependent NMR parameters used for the simulation of the three planar ^{63}Cu transitions in $YBa_2Cu_3O_{6.9}$. The quadrupole frequency $^{63}\nu_Q$ was obtained by NQR. The shift $K_\perp$ and EFG asymmetry η were estimated from the spectrum and were fine adjusted by the simulated spectra. The azimuthal angle α denotes the orientation of the most often encountered EFG orientations (thick green lines in Fig. 5.4 and 5.6).

T (K)	p (kbar)	$K_\perp$ (%)	$^{63}\nu_Q$ (MHz)	η	α (deg)
300	0	0.733(2)	31.17	0.011(1)	0
300	9	0.731(2)	31.26	0.011(2)	0
300	18	0.746(2)	31.11	0.001(1)	90
100	0	0.739(2)	31.5	0.012(1)	0
100	9	0.757(2)	31.32	0.000(3)	0
100	18	0.783(2)	31.08	0.019(1)	90

observed in $YBa_2Cu_3O_7$, i.e., spectral weight above the symmetry line ($\eta = 0$ line) is much less than what is expected from a homogeneously twinned crystal and a distribution of the EFG asymmetry parameter η is present since the pattern is not simply covered by ΔV_{ZZ}. Thus, there are more planar Cu nuclei experiencing an EFG with its smallest component V_{XX} in magnetic field direction and there is a significant part of planar Cu nuclei having an (almost) axially symmetric EFG. At 18 kbar 300 K, the encountered symmetric line is covered ΔV_{ZZ} which means that all Cu nuclei experience a rather well defined, almost axially symmetric EFG. A comparable situation is found at 9 kbar 100 K. Lowering the temperature at 18 kbar, the planar Cu EFG changes and two interpretations are possible: First, the observed shifted line remains symmetric indicating compared to, for instance, the spectra at ambient pressure that $\eta \approx 0$. However, this would demand that the largest EFG principle value V_{ZZ} have been changed by rotating the magnetic field direction. Second, if the difference of the measured spectrum to the axial-symmetry line (dashed line) is due to an EFG asymmetry ($\eta \neq 0$), the respective spectral weight expected in a twinned crystal is missing, cf. thin green line in Fig. 5.6 (18 kbar 100 K). Note, that no intensity loss is observed between 0 kbar and 18 kbar and that a temperature dependent misalignment of the crystal would shift the line to *lower* frequencies.

To evaluate the EFG at 18 kbar, the temperature dependence of the three ^{63}Cu transitions has been measured from 300 K down to 74 K and is depicted in Fig. 5.7. The CT increases slightly with decreasing temperature till it drops below 85 K due to the vanishing spin susceptibility in the superconducting phase[1].

The lower and upper satellite lines are symmetric and move away from each other in a linear fashion by cooling the sample. From the distance of both satellites one can calculate

---

[1] The critical temperature T_c is reduced in a magnetic field.

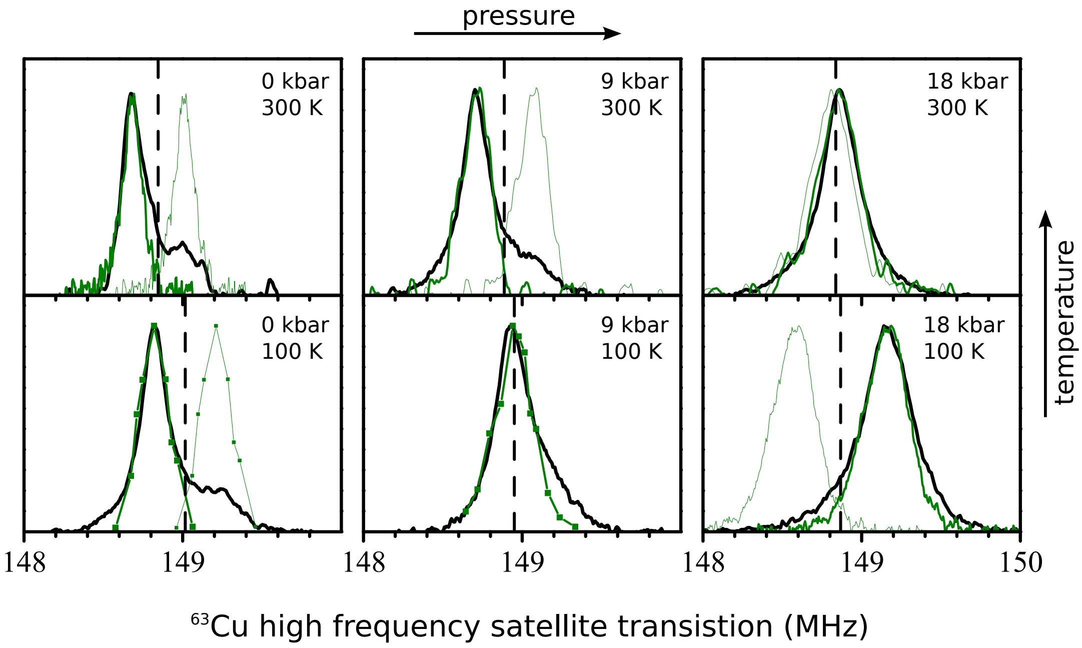

Figure 5.6: Comparison of the measured (black) pressure and temperature dependent ^{63}Cu ST in $YBa_2Cu_3O_{6.9}$ with the simulated spectra (green) based on the assumptions of an orthorhombic, homogeneously twinned crystal. For the simulation the quadrupolar distribution obtained by NQR and the NMR parameters summarized in Tab. 5.1 were used. While the thick green line corresponds to the most often encountered EFG asymmetries, the thin line corresponds to the same EFG but rotated by 90° about the c-axis. See text for details.

either $^{63}\nu_{\mathrm{Q}}(T)$ assuming $\eta = 0$, or $\eta(T)$ with $^{63}\nu_{\mathrm{Q}}(T)$ determined by NQR, cf. Sec. 2.2.1. The brown dashed line represents the expectation for the CT if $^{63}\nu_{\mathrm{Q}}$ increases with lowering the temperature ($\eta = 0$). Clearly the brown line do not cover the experimental data[1]. The result for a temperature dependent asymmetry parameter η using $^{63}\nu_{\mathrm{Q}}(T)$ from NQR are shown as red lines. These lines match all three transitions simultaneously and the accuracy of this model can be seen by the discrepancy of the CT data with the blue line which represents the sum of the determined magnetic part[2] with the second order part having $\eta = 0$. This means that $\eta(T)$ is significant in second order. Thus, the shift of the satellite line is due to a temperature dependent EFG asymmetry.

The result of the temperature dependence at 18 kbar is summarized in Fig. 5.8 where the planar Cu EFG principle component $V_{YY}(T)$ measured in $\sigma \parallel B_0$ is presented. The temperature dependence of the largest EFG principle value V_{ZZ} measured by NQR (green)

---

[1] Although the temperature dependent magnetic part does not depend much on the procedure it is determined, the appropriate way for the ($\eta = 0$)-scenario is to take the mean value of the satellite positions. That this works quite well can be seen at 300 K.

[2] The magnetic part is calculated by subtracting $\nu_{\mathrm{q}}^{(2)}(\nu_{\mathrm{Q}}, \eta)$ from the peak position of the CT.

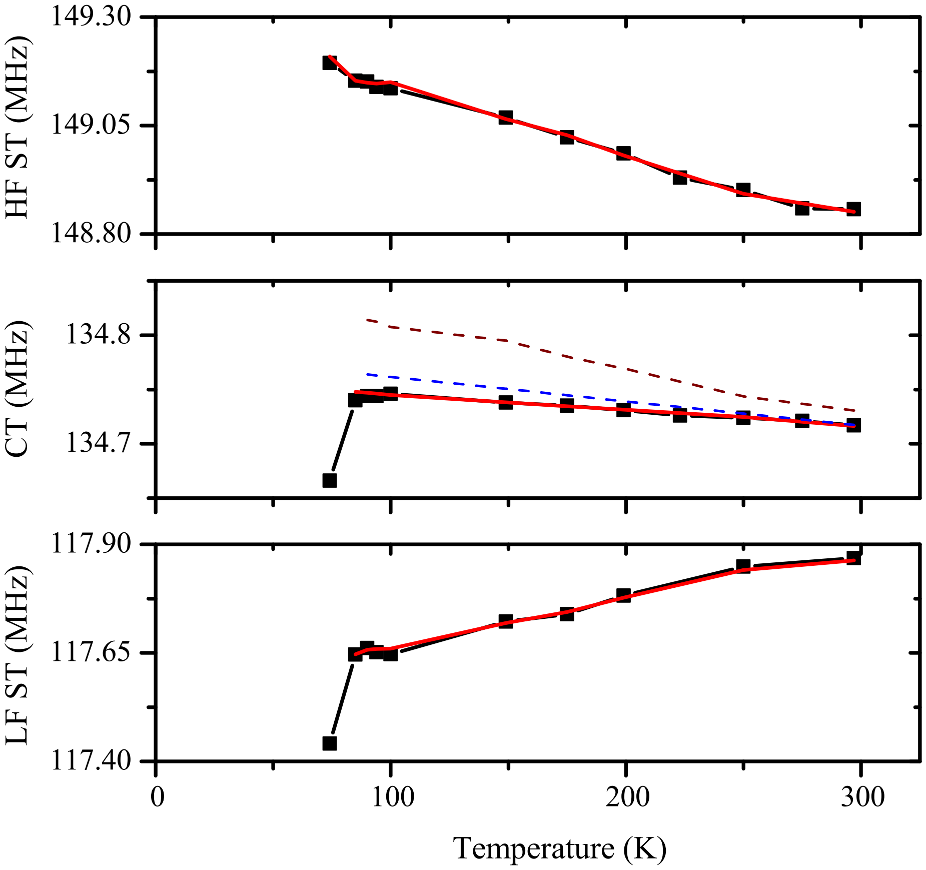

Figure 5.7: Temperature dependence of the three planar ^{63}Cu transitions in $YBa_2Cu_3O_{6.9}$ for $\sigma \parallel B_0$ at 18 kbar. The brown dashed line in the plot of the CT corresponds to the scenario that the divergent STs are explained by a change of the largest EFG component V_{ZZ}. The red line corresponds to a change of the EFG asymmetry η to explain the temperature dependence of the STs. The difference between the red ($\eta(T)$) and the blue ($\eta = 0$) line shows the contribution of η to the second order effect for the CT. Below the critical temperature T_c there is a drop of the CT due to the disappearing spin susceptibility.

and NMR for $c \parallel B_0$ (black) is scaled for comparison assuming an axial symmetric EFG, i.e. $V_{YY} = -V_{ZZ}/2$. Clearly, the measured V_{ZZ} by NQR and NMR in $c \parallel B_0$ agree and the temperature dependence of V_{ZZ} is smaller and opposite compared to $V_{YY}(T)$. The discrepancy can only be lifted by a temperature dependent EFG asymmetry, i.e., $|V_{YY}| > |V_{XX}|$. It must be emphasized, that this is by no means trivial, since an EFG asymmetry which was believed to be determined by the crystals orthorhombicity must result in two lines in a twinned sample which is clearly not the case, cf. thin green line in Fig. 5.6 (18 kbar 100 K). Right below $T_c(B_0 = 11.7\,\mathrm{T})$, it is still possible to measure a signal from the small single

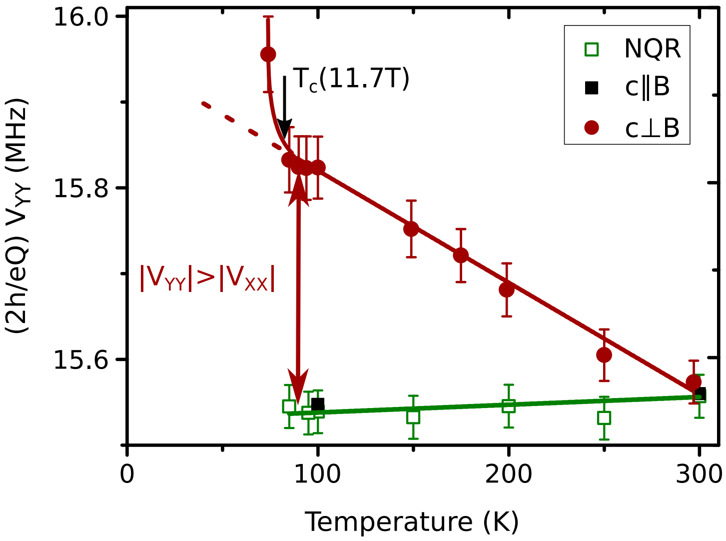

Figure 5.8: Temperature dependence of the planar Cu EFG component V_{YY} measured in $\sigma \parallel B_0$ in $YBa_2Cu_3O_{6.9}$ at 18 kbar. Also shown is the scaled largest Cu EFG component V_{ZZ} determined by NQR (green) and NMR in $c \parallel B_0$ (black) assuming an axially symmetric Cu EFG ($V_{YY} = -V_{ZZ}/2$). The discrepancy is lifted by an asymmetric EFG ($\eta \neq 0$). Note, that there is a jump right below the critical temperature $T_c(B_0 = 11.7\,\mathrm{T})$ which is not observed below $T_c(B_0 = 0\,\mathrm{T})$ with NQR.

crystals[1] and a jump of the EFG principle value is measured in $\sigma \parallel B_0$. Unfortunately, it was not possible to observe a NQR signal at the respective temperature (74 K). Nevertheless, just below the superconducting transition $T_c(B_0 = 0\,\mathrm{T}) = 94\,\mathrm{K}$, a NQR spectrum was obtained which reveals no increase of V_{ZZ} below T_c. From this, it can be concluded, that the jump is either related to a quadrupole effect (V_{ZZ} or η) at about 74 K or a rapid increase of η at the transition into the superconducting state.

Since ΔV_{ZZ} covers almost the full line at 18 kbar, cf. Fig 5.6, most Cu EFGs are aligned, i.e., most Cu nuclei experience an EFG with the principle value V_{YY} in field direction, opposite to what have been found at ambient pressure. Since the EFG asymmetry disappears and reappear by lowering the temperature at 9 kbar and 18 kbar, respectively, detwinning of the sample by accidentally applied uniaxial pressure can be ruled out. Thus, it can be concluded that the distribution of the planar Cu EFG asymmetry is modified dramatically by moderate pressures and changing the temperature. Since there are no structural changes occurring in this pressure and temperature range, i.e., neither significant changes of the crystals orthorhombicity and twining occur nor a structural phase transition is known, this modification is not directly related to the geometric arrangement of ions. The unbalanced peak

---

[1] The low signal to noise ratio of the small single crystal used for the NMR pressure cell is reduced drastically in the superconducting phase due to the screening of the sample.

height observed, for instance, at ambient pressure is anomalous for a homogeneously twinned sample and may be related to the magnetic field direction as it was found in $YBa_2Cu_3O_7$, i.e., the planar Cu EFG asymmetry changes by rotating the magnetic field by 90° about the crystal's c-axis[1]. Furthermore, the gradual change of η as a function of temperature at 18 kbar is indicative of an electronic effect. Therefore, the change of the distribution of the EFG asymmetry η must be due to a modifications of the planar charge arrangement seen by Cu. In fact, the aligned non-axial Cu EFGs at 18 kbar 100 K, but also the two characteristic EFGs at ambient pressure indicate planar charge ordering. Since a charge variation in the Cu $d_{x^2-y^2}$ orbital will not cause an EFG asymmetry at the respective Cu nuclei, the charge contents of the neighboring O atoms must be involved. Thus planar ^{17}O NMR should give more vital clues.

5.3 Charge order from planar O NMR

NMR experiments on planar ^{17}O in a single crystal of $YBa_2Cu_3O_{6.9}$ were performed under the same conditions as the measurements on planar ^{63}Cu shown in the previous section, i.e., in the same sample, for the same orientations and pressures. Only the tunning frequency of the probe has been adjusted for the O resonances. Details about the alignment procedure and the oxygen exchange process can be found in Sec. 3.2.3 and Sec. 3.3.2, respectively. Due to the low quadrupole frequency of planar ^{17}O, comparative measurements with NQR are not feasible for the small crystallites which are used for the pressure cell experiments. In this section, the results of the planar ^{17}O investigation in $YBa_2Cu_3O_{6.9}$ will be presented and discussed with the focus on quadrupolar effects.

The NMR spectrum of ^{17}O with a spin $I = 5/2$ consists of 5 lines - a central transition (CT) and 4 satellite transitions (ST). With the magnetic field along either one planar Cu-O bond direction ($\sigma \parallel B_0$), NMR measures simultaneously[2] spectra from planar O sites with their bond parallel ($O_{\sigma\parallel}$) as well as perpendicular ($O_{\sigma\perp}$) to the magnetic field, cf. the structure of the CuO_2 plane depicted in Fig. 5.2. In addition to planar O, there is a chain and an apex site which are denoted by O(1) and O(4), respectively, cf. Sec. 2.1. Thus, there are a lot of resonances to distinguish. Fortunately, the magnetic shift and EFG tensors of all O sites in $YBa_2Cu_3O_{6+y}$ close to optimal doping are well known at ambient pressure [Pennington and Slichter, 1990] and they change only moderately with pressure and temperature. For the separation of different O sites, it is advantageous that planar ^{17}O is most abundant and

---

[1] Unfortunately, this cannot be proven in the pressure cell since for the needed crystal alignment, the NMR coil axis is parallel to the external magnetic field which makes NMR impossible.

[2] Note, that this is not related to the crystal's orthorhombicity and crystal twinning.

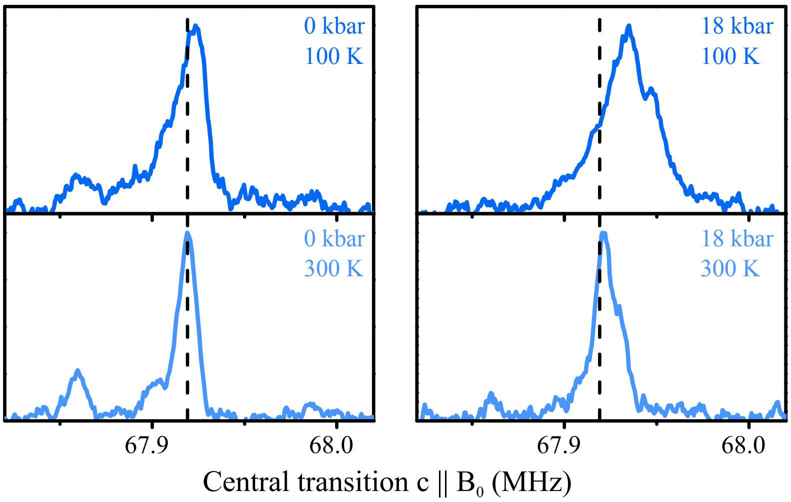

Figure 5.9: Pressure and temperature dependence of the planar ^{17}O CT for $c \parallel B_0$. The dashed line indicates the peak position at 0 kbar 300 K for comparison.

has a comparatively short longitudinal relaxation time T_1 [Pennington and Slichter, 1990]. For clarity and to increase the resolution, the different transitions of a particular O site were selectively measured and transitions which do not belong to the considered site are marked in the respective spectra. All O transitions show a small, but significant second order quadrupole shift $\nu_\mathrm{q}^{(2)}$. However, the modifications of the planar O EFG with pressure and temperature are not significant for $\nu_2^{(2)}$. Thus, the different transitions are corrected for second order effects using the equations listed in Tab. 2.2 and the quadrupole frequency ν_Q and the EFG asymmetry parameters η determined at ambient pressure which agree with literature data [Pennington and Slichter, 1990]. The linewidth of the different O transitions is described by Eq. (2.13). As has been shown by Haase et al. [2002], the planar ^{17}O linewidths can be influenced by a significant correlation between charge and spin density variations. Note that the second order contribution to the linewidth is negligible.

Magnetic field B_0 parallel to the crystal's c-axis ($c \parallel B_0$) The planar ^{17}O CT at 0 kbar and 18 kbar are shown in Fig. 5.9. The CT is affected by $\nu_\mathrm{q}^{(2)}$ and has to be corrected to extract the magnetic shift K_c, however, since $\nu_\mathrm{q}^{(2)}(p, T) \approx$ const., the spectra of CTs reveal the modification of the shift. Starting from ambient conditions (0 kbar 300 K), the shift and the magnetic linewidth increases slightly by cooling down to 100 K or by increasing the pressure to 18 kbar. At 18 kbar, the shift of the CT is considerably larger and the line becomes much broader by cooling down to 100 K compared to ambient pressure.

The full set of planar ^{17}O resonances for $c \parallel B_0$ are shown in Fig. 5.10 for selected

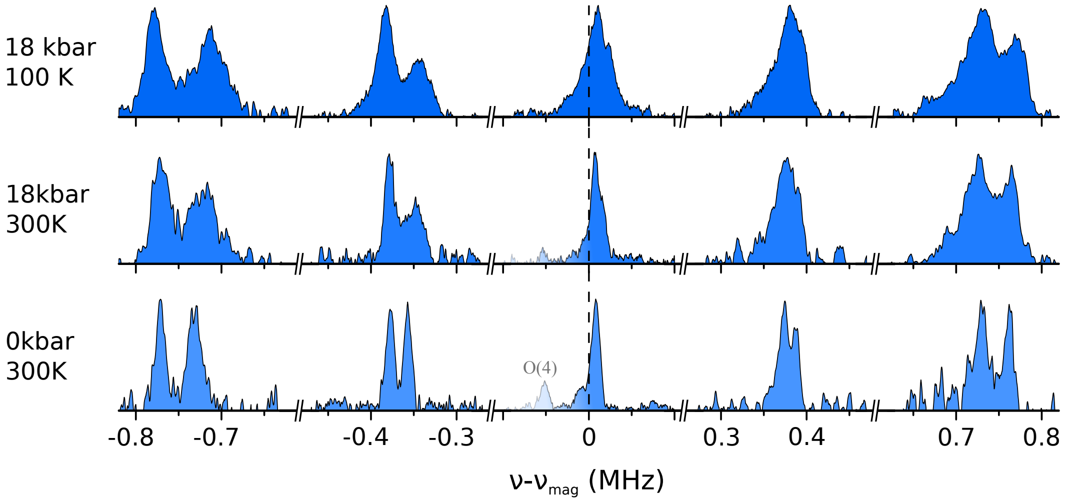

Figure 5.10: Pressure and temperature dependence of the planar ^{17}O central as well as satellite transitions measured for $c \parallel B_0$. For improved comparison of quadrupolar effects, the magnetic part $\nu_{\mathrm{mag}} = (1 + K_c)\nu_0$ was subtracted from each resonance, cf. Tab. 5.2 and Tab. 5.3 for the extracted shifts K_c and quadrupole splittings $^{17}\nu_{\mathrm{Q},c}$. At ambient pressure, the CT of the apex O(4) is visible which was at high pressures suppressed by a larger repetition rate.

conditions. For improved visualization of quadrupolar effects, the magnetic part $\nu_{\mathrm{mag}} = (1+K_c)\nu_0$ is subtracted from each resonance and the shift data can be found in Tab. 5.2. Note, that the shown spectra are not corrected for second order. At ambient pressure, there is a single CT, but the STs reveal two peaks of quadrupolar origin with roughly the same intensity. Assuming a line splitting rather than a special distribution, the peaks of all transitions as measured[1] can be fitted with Gaussian functions and the obtained frequencies are corrected for second order. The two sets of 5 frequencies are than described by $\nu(n) = \nu_{\mathrm{mag}} + n\nu_{\mathrm{Q},c}$ with $n = m - 1/2$ (for $m \leftrightarrow m - 1$) and a linear fit extract the two magnetic and quadrupolar contributions, cf. Sec. 2.2.1 for details. The obtained magnetic shifts of the two sets are identical and the two extracted EFG components agree with literature data [Pennington and Slichter, 1990] and have been interpreted as due to the crystal's orthorhombicity, cf. Sec. 5.1.

Pressure, but also temperature largely do *not* affect the two EFG components, cf. Tab. 5.2, but a significant quadrupolar line broadening is obtained at 18 kbar 300 K which is supersede by a dominating magnetic broadening at 18 kbar 100 K. This effect is emphasized in Fig. 5.14, where the uppermost satellite transition is compared with the solely magnetically broadened CT.

---

[1] Without subtracting the magnetic part.

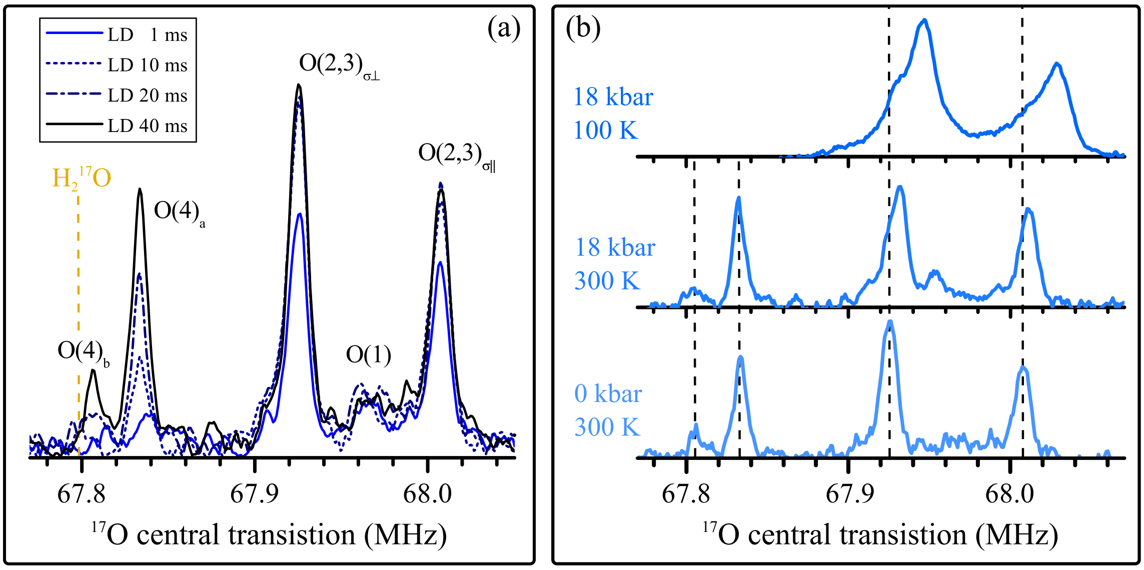

Figure 5.11: Site assignment as well as pressure and temperature dependence of ^{17}O central transitions in $YBa_2Cu_3O_{6.9}$ for $\sigma \parallel B_0$. (a) ^{17}O CTs of various O sites measured with different repetition times (LD). Also shown is the frequency of the reference compound (tap water) and the site assignment. See text for details. (b) Pressure and temperature dependence of the respective ^{17}O CTs. The dashed lines indicate the peak positions at ambient pressure for comparison.

Magnetic field $\boldsymbol{B_0}$ parallel to the planar Cu-O bond ($\boldsymbol{\sigma \parallel B_0}$) In this field direction various O CTs are found and they are depicted in Fig. 5.11 (a) where the spectra are recorded with different repetition times. While the chain O(1) possesses an almost isotropic shift, the more abundant planar O(2,3) sites are expected to have an almost axially symmetric shift with the largest component along the Cu-O bond direction [Pennington and Slichter, 1990]. Contrary, the shift in field direction of the apex O(4) is small and the CT is expected to be close to the reference frequency of tap water which is also shown in Fig. 5.11 (a). Furthermore, while the chain ^{17}O(1) and planar ^{17}O(2,3) nuclei have similar T_1-relaxation times, the apex ^{17}O(4) nuclei relax much slower [Pennington and Slichter, 1990]. Based on these findings as well as the quadrupole splittings (see below), the different transitions in Fig. 5.11 (a) were assigned to the different O sites.

There are two pronounced peaks which correspond to the planar ^{17}O sites having their bond parallel ($O_{\sigma\|}$) as well as perpendicular ($O_{\sigma\perp}$) to the magnetic field. From crystal twinning, two ^{17}O chain resonances are expected close to the position marked with O(1) in Fig. 5.11 (a). Although some intensity is observed, the two transitions are not resolved which is probably due to the low abundance of the chain O. Twinning enables the simultaneous measurement of the two apex ($O(4)_a$ and $O(4)_b$) resonances which reveal unbalanced inten-

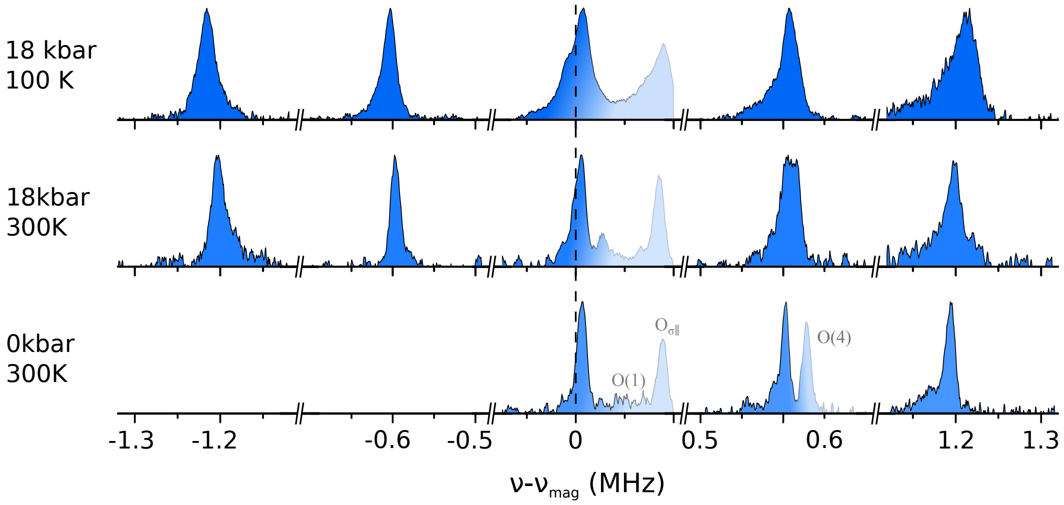

Figure 5.12: Pressure and temperature dependence of the planar $^{17}\mathrm{O}_{\sigma\perp}$ central as well as satellite transitions measured for $c \perp B_0$ (Planar Cu-O bond perpendicular to the magnetic field). For improved comparison of quadrupolar effects, the magnetic part $\nu_{\mathrm{mag}} = (1 + K_{\sigma\perp})\nu_0$ was subtracted from each resonance, cf. Tab. 5.2 and Tab. 5.3 for the extracted shifts $K_{\sigma\perp}$ and quadrupole splittings $^{17}\nu_{\mathrm{Q},\sigma\perp}$. Low frequency STs were not measured at ambient pressure. Close to the planar $^{17}\mathrm{O}_{\sigma\perp}$ CT, the CTs of the chain $^{17}\mathrm{O}(1)$ and planar $^{17}\mathrm{O}_{\sigma\|}$ sites are visible. There is an overlap of the first high frequency ST with the ST of the apex O(4) site.

sities. This is confirmed by the intensity ratio of the first upper apex $^{17}\mathrm{O}(4)$ STs of the respective orientations. The intensity ratio is similar to the unbalanced planar $^{63}\mathrm{Cu}$ STs in that field orientation, cf. Fig. 5.5.

In Fig. 5.11 (b), examples for the pressure and temperature evolution of the CTs are shown. As observed for $c \parallel B_0$, increasing the pressure at 300 K shifts the planar $^{17}\mathrm{O}$ CTs to higher frequencies and cooling to 100 K at 18 kbar further shifts the lines accompanied with a substantial line broadening. Different to planar $^{17}\mathrm{O}$, the apex resonances are not affected. Due to the larger bonding energy of the apex O compared to that of planar O [Conder, 2001], the unaffected apex transitions confirm that no significant structural change occur.

The respective pressure and temperature dependence of the planar $^{17}\mathrm{O}$ CT and STs corresponding to the $\mathrm{O}_{\sigma\perp}$ sites are shown in Fig. 5.12. The most striking feature is the absence of the two peaks in the STs which has been observed before [Pennington and Slichter, 1990]. Only a weak distribution to lower quadrupole frequencies is obtained. Note that the first upper satellite resonance for the different pressures and temperatures is affected by an apex O ST which was proven by different repetition times. While the measured planar O quadrupole splitting $^{17}\nu_{\mathrm{Q},\sigma\perp}$ is not affected by increasing the pressure to 18 kbar,

Table 5.2: Pressure and temperature dependence of the principle values of the planar ^{17}O magnetic shift tensor. The extracted values correspond to the second order corrected peak values of the CTs. Tap water was used as a reference with a frequency of 67.7986 MHz.

T (K)	p (kbar)	$K_{\sigma\|}$(%)	$K_{\sigma\perp}$(%)	K_c(%)
300	0	0.31(1)	0.18(1)	0.17(1)
300	18	0.31(1)	0.19(1)	0.17(1)
100	18	0.34(1)	0.21(1)	0.18(2)

Table 5.3: Pressure and temperature dependence of the planar ^{17}O quadrupole splittings measured with the magnetic field along the EFG's principle axis. See text for details about their determination.

T (K)	p (kbar)	$^{17}\nu_{\mathrm{Q},\sigma\|}$ (MHz)		$^{17}\nu_{\mathrm{Q},\sigma\perp}$ (MHz)	$^{17}\nu_{\mathrm{Q},c}$ (MHz)		δ_{p} (10^{-2})
300	0	0.984(1)	0.963(1)	0.599(1)	0.383(1)	0.365(1)	0.73
300	18	0.995(1)	0.973(2)	0.601(1)	0.383(1)	0.362(1)	0.85
100	18	1.006(2)		0.609(1)	0.388(1)	0.362(1)	1.05

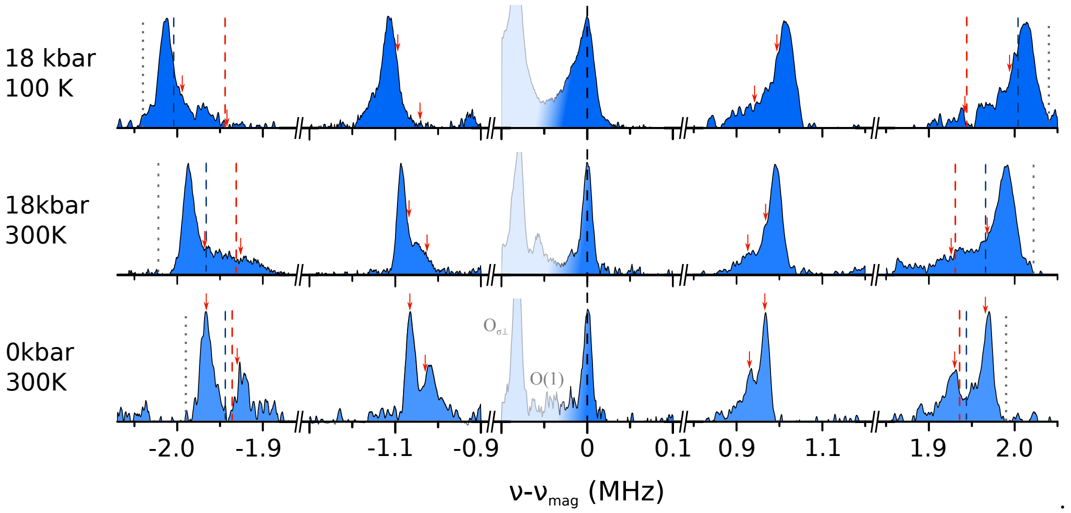

Figure 5.13: Pressure and temperature dependence of the planar $^{17}\mathrm{O}_{\sigma\|}$ CT as well as STs measured for $c \perp B_0$ (planar Cu-O bond parallel to the magnetic field B_0). For improved comparison of quadrupolar effects, the magnetic part $\nu_{\mathrm{mag}} = (1 + K_{\sigma\|})\nu_0$ was subtracted from each resonance, cf. Tab. 5.2 and Tab. 5.3 for the extracted shifts $K_{\sigma\|}$ and quadrupole frequencies $^{17}\nu_{\mathrm{Q}} = {}^{17}\nu_{\mathrm{Q},\sigma\|}$. Close to the planar $\mathrm{O}_{\sigma\|}$ CT, the CTs of the chain O(1) and planar $\mathrm{O}_{\sigma\perp}$ sites are visible. The blue dashed lines represent the first moment of the entire outermost STs. The red dashed lines show the expectation of the first moments from the respective first moments of the spectra from the two other directions using Laplace equation. The grey dotted lines and the red arrows show the expectation for the high frequency edge and peak position from the corresponding properties of the spectra of the other two directions, respectively, again using Laplace equation.

cf. Tab. 5.2, the quadrupolar variation increases. Lowering the temperature at 18 kbar increases ${}^{17}\nu_{\mathrm{Q},\sigma\perp}$ slightly and all transitions are dominated by magnetic variations which is similar to observation for $c \parallel B_0$, cf. Fig. 5.14.

In Fig. 5.13, the full set of the planar ^{17}O resonances which corresponds to the $\mathrm{O}_{\sigma\parallel}$ sites are shown. At ambient pressure, two features are present for each ST which are absent for the CT. The heights of the two peaks are unbalanced. Furthermore, the sharp edges to higher quadrupole frequencies are not observed for the low quadrupole frequency edges of the satellite patterns. Thus, if two lines are present, they have different shapes. This is illustrated in Fig. 5.15 (a) where the first upper planar ^{17}O ST is fitted with a distribution function consisting of a Gaussian and Lorentzian line with rather similar intensities. Two identical functions fit the transition much worse. Clearly, the apparent intensity mismatch given by the different peak heights can be lifted. Note, that a more sophisticated distribution than a line splitting from two chemical sites may also be the origin of the observed planar ^{17}O pattern at ambient conditions. Nevertheless, using the described fit function of a Gaussian and Lorentzian line, two quadrupole splittings ${}^{17}\nu_{\mathrm{Q},\sigma\parallel}$ are obtained, cf. Tab. 5.3, which are in agreement with literature data[1] and have been interpreted as due to the crystal's orthorhombicity, cf. Sec. 5.1. By increasing the pressure to 18 kbar, the sharp feature of the satellites shift to higher quadrupole frequencies and remains sharp. The broad feature shifts similarly but broadens considerably. The quadrupole frequency corresponding to the sharp line of the satellites increases further by lowering the temperature at 18 kbar to 100 K, and the broad feature almost disappears. In fact, since no intensity is lost, cf. Fig. 5.15 (b), both spectral features merge almost completely at 18 kbar and 100 K. Again, at low temperatures the transitions are dominated by magnetic variations, cf. Fig. 5.14. Note, that a misalignment of the sample would decrease the quadrupole splittings and thus can be ruled out.

To sum up, while there is almost no change of the planar ^{17}O spectra obtained for $c \parallel B_0$ and for the $\mathrm{O}_{\sigma\perp}$ sites, the spectra corresponding to the $\mathrm{O}_{\sigma\parallel}$ sites reveal a substantial modification. In particular, the two O EFGs obtained at ambient conditions change differently with pressure and cannot be distinguished anymore at 18 kbar and 100 K. These spectral modifications cannot be due to the crystals orthorhombicity which is insensitive for temperature and pressure variations. Neither can the results be explained by detwinning of the sample since the planar O EFGs merge by *lowering* the temperature at 18 kbar[2]. In other words, if the planar O satellite line splitting for $c \parallel B_0$ which is still visible at 18 kbar and 100 K is due to the crystal's orthorhombicity, than it must also be visible for the $\mathrm{O}_{\sigma\parallel}$ sites in a twinned

---

[1] That the determined planar Cu and O shift and EFG tensors agree with literature demonstrates the accuracy of the alignment procedure of the micro samples in the pressure cell described in Sec. 3.2.3.

[2] High temperatures and uniaxial pressures are needed to detwin the sample [Liang et al., 2000].

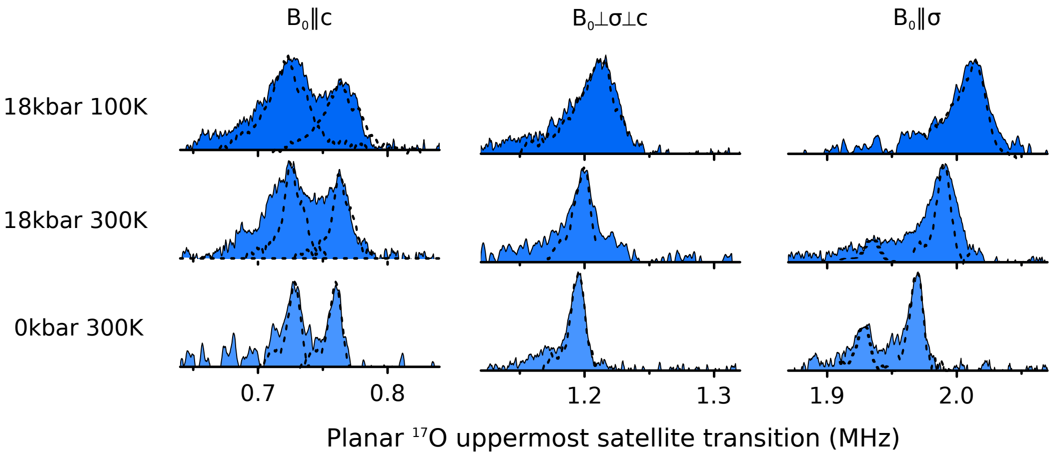

Figure 5.14: Comparison of the uppermost planar ^{17}O STs measured along the different EFG principle axes. For comparison, the magnetic shift was subtracted from each resonance. The outermost satellites possess the largest quadrupole variation. The corresponding shifted CTs which show solely magnetic broadening are plotted for comparison. Note, for the satellites where two splittings were extracted, the CT was plotted for each peak.

crystal. This is clearly not the case. The results are similar to the observations at planar ^{63}Cu where the orthorhombicity is not of importance for the Cu EFG at high pressures. Thus, the planar ^{17}O pattern constitute a variation of the planar O EFGs due to a spatial variation of the planar O charge content n_p which was already suspected from the ^{63}Cu data, cf. Sec. 5.2.

Comparing the planar ^{17}O spectra obtained for different field directions, it is conspicuous that the quadrupole splittings do not increase uniformly, i.e., there is a substantial shift of the spectra corresponding to the $\mathrm{O}_{\sigma\|}$ sites to higher quadrupole frequencies, but almost no change in the other directions. To visualizing this effect, the first moment of the entire outermost satellite spectra are calculated and are shown as blue dashed lines in Fig. 5.13. Note, that the quadrupole effects are largest for the outermost satellites. Using Laplace equations, i.e., $V_{ZZ} = -(V_{XX} + V_{YY})$, the first moments can also be calculated (red dashed lines) from the first moments of the corresponding outermost satellites obtained in the other directions. This analysis is possible since the corresponding intensities of the outermost satellites match for the different orientations, cf. Fig. 5.15 (b). The arrows shown in Fig. 5.13 correspond to the expectations from the peak values instead of the first moments. At ambient pressure, the obtained and expected quadrupole splittings agree well, however, at 18 kbar and 300 K the first moments and peak values are significantly off. At 100 K the discrepancy increases and the expected first moment is totally out of the observed spectrum. This can only be possible if spectral weight from nuclear spins has been summed up that do not reflect one and the same EFG distribution, i.e., the $\mathrm{O}_{\sigma\|}$ sites are different from the $\mathrm{O}_{\sigma\perp}$ sites. Note,

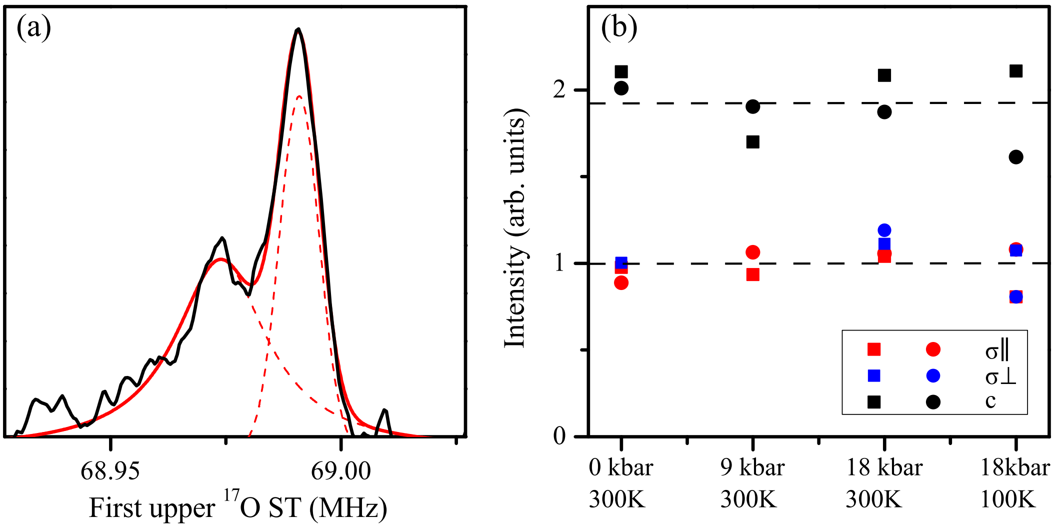

Figure 5.15: (a) The planar ^{17}O first high frequency ST at ambient pressure measured with the magnetic field along the Cu-O bond direction reveals only one sharp edge. Also shown is a fit of a distribution function (solid red) consisting of a Gaussian and Lorentzian line (dashed red) with roughly equal intensities. (b) Intensities of the total planar ^{17}O uppermost (square) and lowermost (circle) satellites for different conditions (p, T). While two oxygen sites ($\mathrm{O}_{\sigma\|}$, $\mathrm{O}_{\sigma\perp}$) are distinguished with the magnetic field within the plane ($\sigma \parallel B_0$), both sites are simultaneously measured with the field perpendicular to the plane ($c \parallel B_0$).

that the expectation from the sharp high frequency edge (gray dotted line in Fig. 5.13) are in agreement for all outermost STs. Again, the obtained discrepancy cannot be related to the orthorhombic structure and indicates that the $\mathrm{O}_{\sigma\|}$ and $\mathrm{O}_{\sigma\perp}$ sites have different O charge contents. Thus, the oxygen charges are spatially ordered.

5.4 Characterization of the observed charge ordering

The NMR measurements on planar ^{63}Cu and ^{17}O presented in the previous sections revealed ordered planar Cu and O EFGs. Since the geometric arrangement of the atoms cannot explain the pressure and temperature dependency, specifically ordered charges lead to the observed planar Cu and O EFGs. To analyze the local charge arrangement, the crystal is assumed to be tetragonal, i.e., there is no direct contribution from the lattice parameters to the EFGs. Since the experiments were performed in the same sample and for the same orientations, a direct comparison of the measured planar ^{63}Cu and ^{17}O data is possible.

As it was shown in Sec. 2.3.2, the planar ^{63}Cu and ^{17}O quadrupole frequencies are determined by the hole content of the bonding orbitals of the $\mathrm{CuO_2}$ plane, and thereby provide a quantitative measure thereof [Haase et al., 2004; Jurkutat et al., 2014]. In particular, while the planar O EFG is solely affected by the on-site hole content n_p, the planar Cu EFG is influenced by both the on-site hole content n_d and the hole content of the four neighboring O atoms $4n_\mathrm{p}$. As mentioned before, n_d and n_p are average hole contents but vary on a local scale, cf. Sec. 4.1. Thus, besides the position of the NMR/NQR resonances, spectral features of the planar ^{63}Cu spectra may originate in the spatial distribution of planar O holes. In the following, a local unit consisting of one Cu with its hole content $\overline{n}_\mathrm{d}$ and four surrounding O atoms with $n_{\mathrm{p},1\ldots4}$ is considered, cf. Fig. 5.16. From Eq. (2.14) and (2.15) one can infer on the Cu and O quadrupole frequencies ν_Q of such a local unit:

$$^{17}\nu_{\mathrm{Q},\sigma} = 2.453\ \mathrm{MHz} \cdot n_{\mathrm{p},i} + 0.39\ \mathrm{MHz} \tag{5.1}$$

$$^{63}\nu_{\mathrm{Q,c}} = 94.3\ \mathrm{MHz} \cdot \overline{n}_\mathrm{d} - 5.68\ \mathrm{MHz} \sum_{i=1\ldots4} (2 - n_{\mathrm{p},i}). \tag{5.2}$$

The planar ^{63}Cu and ^{17}O spectra will be interpreted as a histogram of such local CuO$_4$ units which helps to characterize the local charge ordering.

5.4.1 Broken axial symmetry of the planar Cu EFG due to O charges

Considering the CuO$_4$ unit as point ions, it is obvious that different O valence states may lead to an EFG asymmetry at the Cu site. This must have its equivalence in the description of the quadrupole splittings by the hole contents of planar Cu and O as for example given in Eq. (5.1) and (5.2).

Haase et al. [2004] gave the contribution from the on-site hole content n_p to the planar ^{17}O quadrupole splitting measured for $c \parallel B_0$ which is half of that measured for $\sigma \parallel B_0$:

$$^{17}\nu_{\mathrm{Q,c}} = -1.226\ \mathrm{MHz} \cdot n_{\mathrm{p},i} + {}^{17}C_c. \tag{5.3}$$

In fact, since the EFG is traceless, the on-site charge contribution must be negative. This is also evident from the shape of the $2p_\sigma$ orbital which generates an axially symmetric EFG, i.e., $V_{XX} = V_{YY} = -V_{ZZ}/2$. Note, that the constant $^{17}C_c$ accounts for the planar O EFG asymmetry and is expected to be largely pressure and temperature independent[1].

In a similar way, one can deduce the quadrupole splitting $^{63}\nu_{\mathrm{Q},\sigma}$ of planar ^{63}Cu measured for $\sigma \parallel B_0$ from the symmetry of the involved orbitals [Jurkutat, 2017]. The EFG of the Cu $d_{x^2-y^2}$ orbital is axially symmetric and thus, the contribution to $^{63}\nu_{\mathrm{Q},\sigma}$ from the on-site hole content is negative and half of that measured for $c \parallel B_0$. In Eq. (5.2), the contribution from planar O holes to $^{63}\nu_{\mathrm{Q,c}}$ has been modeled by expanding the O $2p_\sigma$ wave function in the basis

---

[1] The constants appearing in that approach are largely independent on the investigated cuprate and doping level, cf. Sec. 2.3.2. Thus, pressure and temperature are not expected to change them.

of

Cu orbitals $(4s, 4p)$ where only the in-plane $4p$ orbitals contribute to the Cu EFG [Haase et al., 2004]. Since the directions of the symmetry axes of the two in-plane Cu $4p$ orbitals are different, the magnetic field direction has to be taken into account for ${}^{63}\nu_{\mathrm{Q},\sigma}$, i.e., the planar O sites having their Cu-O bond parallel to the magnetic field direction ($\mathrm{O}_{\sigma\|}$) and those O sites where the bond is perpendicular to the field ($\mathrm{O}_{\sigma\perp}$) contribute differently to ${}^{63}\nu_{\mathrm{Q},\sigma}$ and one finds:

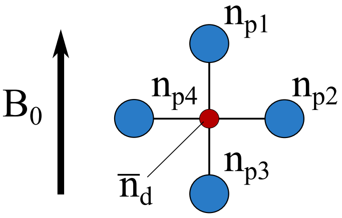

Figure 5.16: Local CuO$_4$ unit consisting of one Cu with its hole content $\overline{n}_{\mathrm{d}}$ and four surrounding O atoms with $n_{\mathrm{p},1\ldots4}$.

$$ {}^{63}\nu_{\mathrm{Q},\sigma} = -47.15\ \mathrm{MHz} \cdot n_d + 11.36\ \mathrm{MHz}(4 - n_{\mathrm{p},1} - n_{\mathrm{p},3}) - 5.68\ \mathrm{MHz}(4 - n_{\mathrm{p},2} - n_{\mathrm{p},4}). \quad (5.4) $$

As shown in Fig. 5.16, the hole contents of the $\mathrm{O}_{\sigma\|}$ atoms are denoted by $n_{\mathrm{p},1}$ and $n_{\mathrm{p},3}$. The contribution of these O sites to ${}^{63}\nu_{\mathrm{Q},\sigma\|}$ is positive and twice as large as the contribution from the $\mathrm{O}_{\sigma\perp}$ atoms having a hole content $n_{\mathrm{p},2}$ and $n_{\mathrm{p},4}$[1].

It is advantageous to describe the individual oxygen hole contents $n_{\mathrm{p},i} = \overline{n}_{\mathrm{p}} + \delta_{\mathrm{p},i}$ as a deviation $\delta_{\mathrm{p},i}$ from the mean value $\overline{n}_{\mathrm{p}} = 1/4 \sum_i n_{\mathrm{p},i}$ in a CuO$_4$ unit. Since the average of the deviation is zero, i.e., $\sum_i \delta_{\mathrm{p},i} = 0$, only the mean value $\overline{n}_{\mathrm{p}}$ is important for the ^{63}Cu quadrupole frequency measured in $c \parallel B_0$ and Eq. (5.2) can be written as:

$$ {}^{63}\nu_{\mathrm{Q,c}} = 94.3\ \mathrm{MHz} \cdot \overline{n}_{\mathrm{d}} - 5.68\ \mathrm{MHz} \cdot 4(2 - \overline{n}_{\mathrm{p}}). \quad (5.5) $$

Thus, the quadrupole contribution to the ^{63}Cu spectra measured for $c \parallel B_0$ are independent of the actual charge variation $\delta_{\mathrm{p},i}$ within a CuO$_4$ unit. This means that the bulk average $n_{\mathrm{d}} =< \overline{n}_{\mathrm{d}} >$ and $n_{\mathrm{p}} =< \overline{n}_{\mathrm{p}} >$ set the position of the line and the spatial variations of $\overline{n}_{\mathrm{d}}$ and $\overline{n}_{\mathrm{p}}$ determine[2] the spectral distribution of the planar Cu resonances in $c \parallel B_0$. Moreover, Eq. 5.5 gives a specific in-plane contribution $(-{}^{63}\nu_{\mathrm{Q,c}}/2)$ which helps to write Eq. 5.4 in the form of the first order quadrupole correction ${}^{63}\nu_{\mathrm{Q},\sigma} = -{}^{63}\nu_{\mathrm{Q},c}/2(1 + \overline{\eta})$ with:

$$ \frac{{}^{63}\nu_{\mathrm{Q},c}\,\overline{\eta}}{2} = 5.68\ \mathrm{MHz} \cdot \frac{3}{2}(\delta_{\mathrm{p},1} - \delta_{\mathrm{p},2} + \delta_{\mathrm{p},3} - \delta_{\mathrm{p},4}), \quad (5.6) $$

which is a measure for the Cu EFG asymmetry $V_{XX} - V_{YY}$ of the CuO$_4$ unit. In fact, ${}^{63}\nu_{\mathrm{Q,c}}\,\overline{\eta}/2$, measures the deviation from the position of an axially symmetric Cu EFG due

---

[1] In Eq. (5.2), only one O prefactor appears since for $c \parallel B_0$, the magnetic field is perpendicular to all in-plane $4p$ orbitals.

[2] Both may be correlated which could influence the spectrum.

to the different O hole contents within a CuO_4 unit. Thus, with the knowledge of $\delta_{\mathrm{p},i}$, the deviation can be calculated. Note that there are configurations which conserve the axial symmetry of the EFG at the Cu site, e.g., for $\delta_{\mathrm{p},1} = \delta_{\mathrm{p},2}$ and $\delta_{\mathrm{p},3} = \delta_{\mathrm{p},4}$, cf. Fig. 5.17. Furthermore, in addition to a variation of $\overline{n}_{\mathrm{d}}$ and $\overline{n}_{\mathrm{p}}$, a distribution of $\delta_{\mathrm{p},i}$ will cause spectral modification of the Cu ST in $\sigma \parallel B_0$, e.g., the Cu STs could be broader than half of the satellite linewidth measured for $c \parallel B_0$.

In the following, this model will be used to analyze the measured data.

5.4.2 Insights from the spectra measured for $c \parallel B_0$

For $c \parallel B_0$, the magnetic field does not distinguish different planar O sites and thus, ^{17}O NMR measures all planar O sites simultaneously. Planar ^{17}O NMR revealed two equally abundant oxygen sites for $c \parallel B_0$ at ambient pressure. Since the planar O quadrupole splitting is determined by the on-site hole content (Eq. (5.3)), the two sites indicate a slight difference in the charge content ($2\delta_{\mathrm{p}}$). In fact, the quadrupole splittings do not vary largely with pressure and temperature, cf. Fig. 5.10, and thus an O charge distribution with a substantial amplitude δ_{p} seems to be a pressure and temperature independent feature of the CuO_2 plane. If two distinct hole contents are present $n_{\mathrm{p},i} = n_{\mathrm{p}} \pm \delta_{\mathrm{p}}$, there are 16 configurations of the CuO_4 unit possible which are illustrated in Fig. 5.17. Note, that the 16 configurations have different mean values $\overline{n}_{\mathrm{p}}$ which could affect the ^{63}Cu spectra in this field direction. Using Eq. (5.3), the amplitude $\delta_{\mathrm{p}} = \Delta\nu_{\mathrm{Q},c}/(2 \cdot 1.226\ \mathrm{MHz})$ can be calculated from the satellite line splitting $\Delta\nu_{\mathrm{Q},c}$ obtained for $c \parallel B_0$. The modifications of δ_{p} with pressure and temperature are listed in Tab. 5.3. From the obtained spectra it is clear that the two different hole contents are most prominent, but there may also exist units without a variation ($\delta_{\mathrm{p},i} = \pm\delta_{\mathrm{p}} \approx 0$) which are much less abundant. More generally, a complex distribution of charges with two features may also be realized and not visible in the spectra[1]. However, for the sake of discussion two distinct O hole contents will be assumed.

The planar Cu quadrupole frequency $^{63}\nu_{\mathrm{Q},c}$ is affected by the hole contents of the Cu and O orbitals. The contribution from O holes for the different configurations are given in Tab. 5.4. If only CuO_4 units appear where the charge variations compensate, i.e., $\overline{n}_{\mathrm{p}} = n_{\mathrm{p}}$ (configurations C1 and C6), variations at planar O do not contribute to the Cu linewidth. However, if the mean value $\overline{n}_{\mathrm{p}}$ is distributed, the lineshape and linewidth can be influenced. For instance, if there are only two CuO_4 units present having a mean value of either $\overline{n}_{\mathrm{p}} = n_{\mathrm{p}} + \delta_{\mathrm{p}}$ (C1) or $\overline{n}_{\mathrm{p}} = n_{\mathrm{p}} - \delta_{\mathrm{p}}$ (C6), a ^{63}Cu satellite line splitting of about 330 kHz is expected at ambient conditions, cf. Tab. 5.4. Since the planar ^{63}Cu STs for $c \parallel B_0$ are symmetric

---

[1] For instance, if the quadrupole width is half of the magnetic width, it is not easily revealed in the O spectra dominated by magnetic broadening.

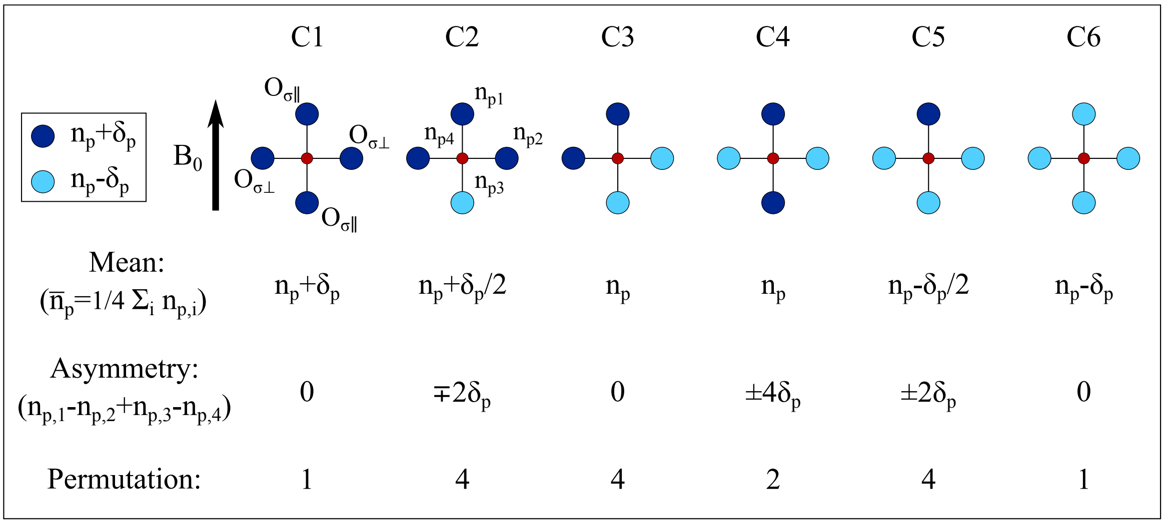

Figure 5.17: Configurations of the CuO$_4$ unit with two distinct O hole contents $n_{\mathrm{p},1\ldots4} = n_\mathrm{p} \pm \delta_\mathrm{p}$. While $n_{\mathrm{p},1}$ and $n_{\mathrm{p},3}$ are the hole contents of the O$_{\sigma\|}$ orbitals, $n_{\mathrm{p},2}$ and $n_{\mathrm{p},4}$ belong to the O$_{\sigma\perp}$ orbitals. In total, there are 16 combinations of a CuO$_4$ unit with two distinct hole contents possible. The mean value ($\bar{n}_\mathrm{p} = 1/4\sum_i n_{\mathrm{p},i}$) and the asymmetry ($n_{\mathrm{p},1} - n_{\mathrm{p},2} + n_{\mathrm{p},3} - n_{\mathrm{p},4}$) of the respective CuO$_4$ configurations affects the Cu spectra. See text for details.

and more narrow (300 kHz), such a scenario can be excluded. Thus, most of the units must have mixed O hole contents and various scenarios are possible. As will be shown, the NMR data obtained for $\sigma \parallel B_0$ give further limitations for the possible local units which will be discussed for the different conditions (p,T) separately.

5.4.3 Local charge distribution at 18 kbar 100 K

At these conditions, the O lines are dominated by magnetic broadening, cf. Fig. 5.14. This means that the quadrupolar linewidth is much smaller than the total linewidth of the ^{17}O STs and thus, the planar O EFGs are rather well defined. Although, there are two lines present in the satellite pattern measured for $c \parallel B_0$, there is only one line observed for the oxygens with the magnetic field parallel to their bond (O$_{\sigma\|}$) as well as for the O sites having their bond perpendicular to the field (O$_{\sigma\perp}$). This indicates that there is only one characteristic type of O present for the O$_{\sigma\|}$ as well as for the O$_{\sigma\perp}$ sites which are both simultaneously measured for $c \parallel B_0$. Furthermore, it was shown that the EFGs of the O$_{\sigma\|}$ sites are different from the EFGs of the O$_{\sigma\perp}$ sites which was attributed to different O hole contents. Since the quadrupole frequency of the O$_{\sigma\|}$ sites is larger than the expectation from the spectra of the other field directions, cf. dashed lines in Fig. 5.13, the O$_{\sigma\|}$ sites must have a larger hole content, i.e., $n_\mathrm{p} + \delta_\mathrm{p}$. Consequently, the O$_{\sigma\perp}$ sites must have the lower hole content, i.e., $n_\mathrm{p} - \delta_\mathrm{p}$. This is

Table 5.4: Configurations of the $\mathrm{CuO_4}$ unit with two distinct hole contents $n_\mathrm{p} \pm \delta_\mathrm{p}$ as shown in Fig. 5.17 and their implications on the ^{63}Cu satellite transitions for 0 kbar 300 K and 18 kbar 100 K. The contribution to the quadrupole frequency measured for $c \parallel B_0$ can be calculated using $\Delta^{63}\nu_{\mathrm{Q},c} = -5.68\ \mathrm{MHz} \cdot 4\delta_\mathrm{p}(\xi_1 + \xi_2 + \xi_3 + \xi_4)$. The shift from the ^{63}Cu satellite position of an axially symmetric EFG measured for $\sigma \parallel B_0$ is given by $^{63}\nu_{\mathrm{Q},c}\,\overline{\eta}/2 = 5.68\ \mathrm{MHz} \cdot 3\delta_\mathrm{p}(\xi_1 - \xi_2 + \xi_3 - \xi_4)$. The amplitude δ_p is estimated from the ^{17}O satellite line splitting measured for $c \parallel B_0$. See text for details.

					0 kbar 300 K $\delta_\mathrm{p} = 0.73 \cdot 10^{-2}$		18 kbar 100 K $\delta_\mathrm{p} = 1.05 \cdot 10^{-2}$	
	ξ_1	ξ_2	ξ_3	ξ_4	$\Delta^{63}\nu_{\mathrm{Q},c}$ (kHz)	$^{63}\nu_{\mathrm{Q},c}\,\overline{\eta}/2$ (kHz)	$\Delta^{63}\nu_{\mathrm{Q},c}$ (kHz)	$^{63}\nu_{\mathrm{Q},c}\,\overline{\eta}/2$ (kHz)
C1	1	1	1	1	-166	0	-240	0
C2	1	1	-1	1	-83	-125	-120	-180
	1	1	1	-1	-83	+125	-120	+180
	-1	1	1	1	-83	-125	-120	-180
	1	-1	1	1	-83	+125	-120	+180
C3	1	-1	-1	1	0	0	0	0
	1	1	-1	-1	0	0	0	0
	-1	1	1	-1	0	0	0	0
	-1	-1	1	1	0	0	0	0
C4	1	-1	1	-1	0	+250	0	+360
	-1	1	-1	1	0	-250	0	-360
C5	1	-1	-1	-1	+83	+125	+120	+180
	1	1	-1	-1	+83	-125	+120	-180
	-1	-1	1	-1	+83	+125	+120	+180
	-1	-1	-1	1	+83	-125	+120	-180
C6	-1	-1	-1	-1	+166	0	+240	0

a strong limitation, since only one $\mathrm{CuO_4}$ unit symmetry fulfills these requirements which is depicted in Fig. 5.18 (a). The deduced configuration with $\delta_\mathrm{p} = (1.05 \pm 2) \cdot 10^{-2}$ explains the discrepancy of about 30 kHz indicated by the dashed lines in Fig. 5.13. In fact, a difference of 39 kHz is predicted[1] between the expected (red) and actual (blue) quadrupole frequencies. Despite uncertainties due to the linewidths, it is clear that the presented $\mathrm{CuO_4}$ unit must be dominant throughout the whole crystal.

The Cu data at these conditions revealed an asymmetric EFG that is ordered along the magnetic field direction, i.e., only the Cu EFG component V_{YY} was measured in magnetic field direction. Using Eq. 5.6, the predominant $\mathrm{CuO_4}$ unit with $\delta_\mathrm{p} = (1.05 \pm 2) \cdot 10^{-2}$ determined from ^{17}O satellite line splitting results in a Cu EFG asymmetry with a positive frequency shift of +360 kHz. This is in astonishing agreement with the observed shift shown

---

[1] The deviation of the first moments can be calculated by: $< {}^{17}\nu_{\mathrm{Q},\sigma\parallel} > - < {}^{17}\nu_{\mathrm{Q},\sigma\perp} > - < {}^{17}\nu_{\mathrm{Q},c} >= 1.226\ \mathrm{MHz} \cdot (2 < n_\mathrm{p} + \delta_\mathrm{p} > - < n_\mathrm{p} - \delta_\mathrm{p} > - < n_\mathrm{p} \pm \delta_\mathrm{p} >) = 1.226\ \mathrm{MHz} \cdot 3\delta_\mathrm{p}$.

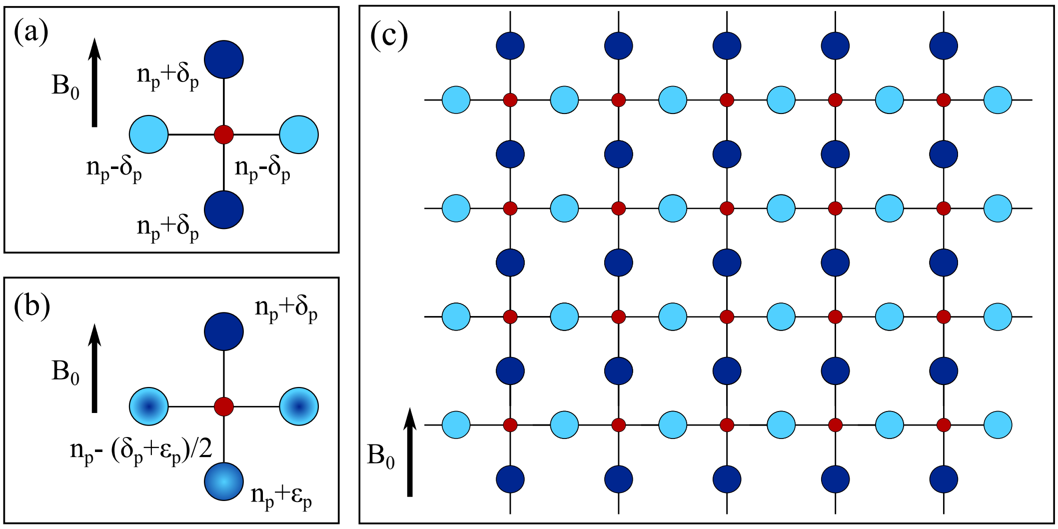

Figure 5.18: Determined CuO$_4$ units and long range order pattern. The ^{63}Cu and ^{17}O spectra at 18 kbar 100 K reveal an unambiguous CuO$_4$ unit (a) with the larger hole content found in the O$_{\sigma\|}$ orbitals. The data are in agreement with a long range order pattern (c). The spectra at 18 kbar 300 K show less order. The characteristic unit (b) at these conditions is described by a rather well defined $n_\mathrm{p} + \delta_\mathrm{p}$ and a distributed $n_\mathrm{p} + \epsilon_\mathrm{p}$ ($-\delta_\mathrm{p} < \epsilon_\mathrm{p} < \delta_\mathrm{p}$) hole content of the O$_{\sigma\|}$ orbitals as well as two distributed hole contents $n_\mathrm{p} - (\delta_\mathrm{p} - \epsilon_\mathrm{p})/2$ of the O$_{\sigma\perp}$ orbitals.

in Fig. 5.5, where the peak frequency is shifted from the axial symmetry line by +320 kHz. Note, that there is no other configuration of the CuO$_4$ unit which can account quantitatively for the ^{63}Cu data, cf. Tab. 5.4. Furthermore, the planar ^{63}Cu linewidth is not influenced by a variation $n_\mathrm{p} \pm \delta_\mathrm{p}$ of the oxygen charges in the determined CuO$_4$ unit. This is exactly what was obtained, i.e., the measured width for $\sigma \parallel B_0$ (350 kHz) is approximately half of that measured for $c \parallel B_0$ (750 kHz). Thus, it is concluded that the ^{63}Cu linewidth actually originate from a variation of the Cu hole content n_d with an amplitude of about $\delta_\mathrm{d} = 0.4{\cdot}10^{-2}$.

In summary, for 18 kbar 100 K charge ordering throughout the sample is obtained and one is tempted to conclude that the data demand long-range ordering as shown in Fig. 5.18 (c). However, NMR measures only local order and the Cu and O linewidths leave room for more sophisticated models. For instance, it could be possible that the order is incommensurate after a few units, and thus difficult to see with long range probes.

5.4.4 Local charge distribution at 18 kbar 300 K

For these conditions, the first moments of the O spectra obtained in $c \parallel B_0$ do not change from 100 K to 300 K, however, the first moments of the spectra obtained for $\sigma \parallel B_0$ decrease. In addition, there is a substantial quadrupole variation present in all the obtained ^{17}O spectra,

Table 5.5: Variations of the characteristic $\mathrm{CuO_4}$ unit at 18 kbar 300 K as shown in Fig. 5.18 (b) and their implications on the ^{63}Cu satellite transitions. The contribution to the quadrupole frequency measured for $c \parallel B_0$ can be calculated using $\Delta^{63}\nu_{\mathrm{Q},c} = -5.68\ \mathrm{MHz} \cdot 4\delta_\mathrm{p}(\xi_1 + \xi_2 + \xi_3 + \xi_4)$ and is zero for the characteristic unit at 18 kbar 300 K. The shift from the ^{63}Cu satellite position of an axially symmetric EFG measured for $\sigma \parallel B_0$ is given by $^{63}\nu_{\mathrm{Q},c}\,\overline{\eta}/2 = 5.68\ \mathrm{MHz} \cdot 3\delta_\mathrm{p}(\xi_1 - \xi_2 + \xi_3 - \xi_4)$. The amplitude $\delta_\mathrm{p} = 0.85 \cdot 10^{-2}$ is estimated from the O satellite line splitting measured for $c \parallel B_0$. See text for details.

ξ_1	ξ_2	ξ_3	ξ_4	$\Delta^{63}\nu_{\mathrm{Q},c}$ (kHz)	$^{63}\nu_{\mathrm{Q},c}\,\overline{\eta}/2$ (kHz)
1	0	-1	0	0	0
1	-0.125	-0.75	-0.125	0	36
1	-0.25	-0.5	1	0	72
1	-0.375	-0.25	-0.375	0	109
1	-0.5	0	-0.5	0	145
1	-0.625	0.25	-0.625	0	181
1	-0.75	0.5	-0.75	0	217
1	-0.875	0.75	-0.875	0	254
1	-1	1	-1	0	290

cf. 5.14. The change of the position and the quadrupolar variations of the lines indicate a charge redistribution within the plane resulting in a larger variation of the $\mathrm{CuO_4}$ units. Thus, it is not possible to discuss merely two distinct O hole contents. Nevertheless, the data give restrictions which allow to infer on a characteristic local $\mathrm{CuO_4}$ unit.

The spectra sampling the $\mathrm{O}_{\sigma\parallel}$ sites reveal a rather sharp peak, cf. 5.13, which corresponds to a well defined O hole content $n_{\mathrm{p},1} = n_\mathrm{p} + \delta_\mathrm{p}$ (or $n_{\mathrm{p},3}$)[1]. These sites are found for approximately half of the $\mathrm{O}_{\sigma\parallel}$ nuclei, while the other half are represented by a broad featureless line to lower quadrupole frequencies. This indicates a smaller but largely distributed hole content $n_{\mathrm{p},3} = n_\mathrm{p} + \epsilon_\mathrm{p}$ ($\epsilon_\mathrm{p} < \delta_\mathrm{p}$) for the latter oxygens. This is similar to the spectra found for $c \parallel B_0$ where only the high quadrupole frequency edge is rather well defined, cf. Fig. 5.14. In contrast, the spectra corresponding to the $\mathrm{O}_{\sigma\perp}$ sites are rather symmetric and reveal neither a sharp edge to lower nor to the higher quadrupole frequencies. Thus, the spectra do not reveal two characteristic sites and a distributed hole content is expected for the $\mathrm{O}_{\sigma\perp}$ sites due to the pronounced quadrupole broadening. It is assumed that on average the O charges within a $\mathrm{CuO_4}$ unit compensate which allows to estimate the charge content of the $\mathrm{O}_{\sigma\perp}$ sites $n_{\mathrm{p},2/4} = n_\mathrm{p} - (\delta_\mathrm{p} + \epsilon_\mathrm{p})/2$. This is consistent with the featureless and broad spectra of the $\mathrm{O}_{\sigma\perp}$ sites and the smaller Cu linewidth measured for $c \parallel B_0$ compared to 100 K.

The characteristic $\mathrm{CuO_4}$ unit for 18 kbar 300 K is shown in Fig. 5.18 (b). Similar to

---

[1] It cannot be concluded on the position of the O with the higher charge content, i.e., the index may be exchange 1 ↔ 3.

the 100 K data, the hole distributions differ distinctly between the "sharp" $\mathrm{O}_{\sigma\|}$ sites and all $\mathrm{O}_{\sigma\perp}$ sites. However, depending on the actual distribution of δ_p and ϵ_p, some of the "broad" $\mathrm{O}_{\sigma\|}$ sites will have the same hole contents as some $\mathrm{O}_{\sigma\perp}$ sites which will result in common spectral elements. This is in accord with the expectations from Laplace equation, cf. dashed lines in Fig. 5.13. While the discrepancy between the actual (blue) and expected (red) first moments of the outermost satellites is reduced from 100 K to 300 K and the broad feature reveals common spectral elements, the sharp feature is still off from the expectation from the peak positions (arrows).

The actual distribution of δ_p and ϵ_p influences the planar Cu EFG asymmetry and the quadrupolar linewidth. In Tab. 5.5, the shift from the satellite position of an axially symmetric Cu EFG is shown for some ϵ_p in the range of $-\delta_\mathrm{p} < \epsilon_\mathrm{p} < \delta_\mathrm{p}$. From the almost axial symmetric ^{63}Cu ST, cf. Fig. 5.5, it can be concluded that ϵ_p is rather negative.

Clearly, increasing the temperature reduces local and global ordering and it is not possible to draw a well defined picture as for 18 kbar 100 K. However, the sharp high quadrupole frequency peaks indicate that ordering is not completely lost since for half of the $\mathrm{O}_{\sigma\|}$ sites the hole content is rather well defined. From the temperature dependence of the Cu EFG asymmetry, cf. Fig. 5.8, it can be concluded that ordering at low temperatures is achieved gradually.

5.4.5 Local charge distribution at 0 kbar 300 K

At these conditions, there are two features present in the spectra corresponding to the $\mathrm{O}_{\sigma\|}$ sites. This is similar to what is found for $c \parallel B_0$, i.e., two lines were measured having similar intensities. Laplace equations allows to predict the first moments as well as the peak positions correctly, cf. dashed lines and arrows in Fig. 5.13. This indicates that the peaks observed for the $\mathrm{O}_{\sigma\|}$ sites correspond to the peaks measured for $c \parallel B_0$. Thus, it is concluded that two representative hole contents are present and all 16 combinations of the CuO_4 unit may be possible, cf. Tab. 5.4. However, although the total linewidth of the spectra corresponding to the $\mathrm{O}_{\sigma\|}$ is roughly twice of the linewidth observed in the other two directions as expected, the satellite line splitting measured for $\sigma \parallel B_0$ and $c \parallel B_0$ are similar. Therefore, the amplitude δ_p is not well defined, cf. Eq. (5.1) and Eq. (5.3). The expectations for the planar ^{63}Cu satellites using $\delta_\mathrm{p} = 0.73 \cdot 10^{-2}$ from the $c \parallel B_0$ data are given in Tab. 5.4. Note, that the calculated frequencies are approximately half of that given in Tab. 5.4 if δ_p is extracted from the $\mathrm{O}_{\sigma\|}$ spectra.

From the ^{63}Cu STs measured in $c \parallel B_0$, CuO_4 units with a unique O charge content (configurations C1 and C6) can be excluded, cf. Sec. 5.4.2. Even for half of the amplitude, they are unlikely, and thus there are not merely two phases present. Furthermore, the ^{63}Cu satellite pattern measured for $\sigma \parallel B_0$ revealed a distribution of the EFG asymmetry parameter η with a characteristic feature to lower frequencies, cf. Fig. 5.5. Therefore, the CuO$_2$ plane may be composted of configurations C2-C5, however, C3 cannot be dominant since it results in an axially symmetric Cu EFG, cf. Tab. 5.4. Furthermore, lower charge contents $n_\mathrm{p} - \delta_\mathrm{p}$ are more often encountered for the O$_{\sigma\parallel}$ sites than for the O$_{\sigma\perp}$ sites, since more Cu nuclei are obtained below the axial symmetry line.

Due to the linewidth of the spectra and the uncertainties in δ_p, it is not possible to conclude on a characteristic CuO$_4$ unit at 0 kbar 300 K. Still, a random distribution of two O charges is not in agreement with planar ^{63}Cu spectra, and thus the peaks signal some type of order. Since configuration C4 possesses no excess charge ($\overline{n}_\mathrm{p} = n_\mathrm{p}$), it could be energetically favored compared to C2 and C5. In fact, a lattice composed of the two permutations of C4 could result in the pattern as illustrated in Fig. 5.2 (different colors) representing are commensurate charge modulation as proposed previously Haase and Slichter [2003].

5.4.6 Discussion of the applied analysis

The formulas (2.14) and (2.15) which relate the quadrupole frequencies of planar ^{63}Cu and ^{17}O with the hole contents of the bonding orbitals of the CuO$_2$ plane, are very well established on a global scale, i.e., for the average quadrupole frequencies and average planar hole contents [Haase et al., 2004; Jurkutat et al., 2014; Rybicki et al., 2016]. However, it remains to be shown whether the method is also valid on a microscopic scale. In a theoretical paper, Kharkov and Sushkov [2016] used Eq. (2.14) and (2.15) to quantify the amplitude of the charge density wave in YBCO observed in high magnetic fields and low temperatures. The observed amplitudes at planar Cu and O are similar to what was found at 18 kbar 100 K. In addition, the astonishing agreement of the measured Cu EFG asymmetry with the calculated one using the amplitude of the O charge variation indicates that these equations are indeed useful on a microscopic scale.

On the other hand, for the data at 0 kbar 300 K it was not possible to draw a well defined local unit and the spatial variation of planar charges needs to be investigated further. In fact, although the spectral width of the different spectra scale as expected, it is unclear why the O satellite line splitting measured for $c \parallel B_0$ is similar to the splitting observed for the O$_{\sigma\parallel}$ sites (half of the value is expected). Furthermore, there is no clear splitting visible for spectra corresponding to the O$_{\sigma\perp}$ sites, although, this is expected for all the remaining configurations of the CuO$_4$ unit at 0 kbar 300 K. Clearly, for a frequency distribution given by a fixed spatial variation of charges, only the first moment and the extension of the distribution must agree for different field directions. The peak values must not stay in a simple relation. Thus, a more sophisticated charge modulation maybe present. In addition, it is not excluded that other orbitals than the Cu $d_{x^2-y^2}$ and O $2p_\sigma$ are involved. Indeed, if the charge content of the O $2p_{\pi,c}$ orbital were modified, the discrepancy of the O satellite line splittings at ambient conditions would be lifted.

In Sec. 4.3 it was shown that the magnetic field strength and direction affect the planar Cu EFG. Furthermore, the data at 18 kbar 100 K reveal the emergence of charge order along the magnetic field direction, i.e., larger hole contents are found for the oxygens with their Cu-O bond parallel to the magnetic field direction[1]. Thus, the origin of this field dependence needs to be closer investigated and it has to be shown whether and how spectra corresponding to different magnetic field orientations can be compared. Magnetic field and angular dependent NMR measurements may help to decide on that. For instance, a commensurate charge density wave (CDW) could be in phase with the lattice for $c \parallel B_0$, i.e., the planar nuclei sample the extrema of the CDW. It would then be sufficient that only the phase of the CDW is affected by the magnetic field direction such that the nuclei do not sample the extrema of the CDW anymore. The quadrupole splitting is then smaller than expected from the $c \parallel B_0$ data.

Finally, one can only infer unambiguously on local pictures from NMR if the observed charges are static on the NMR timescale. The knowledge of the timescale of the charge fluctuations would constitute a great advance for the investigation of the charge effects in the cuprates.

5.5 Conclusion

The results presented in this chapter have important consequences. First of all, the interpretation of the planar Cu and O EFGs in orthorhombic YBCO have been renewed. The EFGs are distributed and are affected by moderate pressures and temperatures. The crystal's orthorhombicity cannot account for the modifications and thus they are of soft electronic origin.

At ambient pressure, the observed double peak structure of the Cu and O NMR satellite patterns reveals the manifestation of charge ordering at planar O. Pressure and lowering the temperature induce further ordering and establish a unique CuO_4 unit at 18 kbar 100 K. The data are consistent with a long range charge density wave with pronounced d-wave symmetry, cf. Fig. 5.18 (c). Similar electronic structure symmetries were discovered with scanning tunneling microscopy (STM) [Fujita et al., 2014] and x-ray [Comin et al., 2015]. In addition, NMR allows to infer on the amplitude of the charge modulation and the data at 18 kbar 100 K

---

[1] This is independent of the analysis, since the measured planar Cu and O EFGs reveal this feature already.

reveal a Cu and O amplitude of about $\delta_\mathrm{d} = 0.004$ and $\delta_\mathrm{p} = 0.01$, respectively. These amplitudes are similar to what has been found in high magnetic fields and very low temperatures in underdoped YBCO [Kharkov and Sushkov, 2016; Wu et al., 2011, 2013]. Thus, it is concluded that charge ordering is not an exclusive feature of underdoped YBCO. Furthermore, the investigated sample is close to optimal doping ($T_\mathrm{c} = 90.3\,\mathrm{K}$) and pressure increases the critical temperature by 4 K. This shows that charge ordering coexist with superconductivity. This is emphasized by the further increased local order seen by planar Cu below T_c at 18 kbar.

The predominant CuO_4 unit measured at 18 kbar 100 K reveal a symmetry breaking, i.e., the large O hole content is encountered for the $O_{\sigma\|}$ sites, whose origin is unclear. The uniform direction of the obtained CuO_4 unit cannot be related to the orthorhombicity since two orientations of that unit would be expected in the investigated twinned crystal which is not obtained. On the other hand, the magnetic field is known to induce or enhance charge ordering [Chang et al., 2016; Hücker et al., 2014] and it was shown in Sec. 4.3 that the magnetic field affects the planar Cu EFG. Thus, one may conclude that the magnetic field also breaks the electronic symmetry of the CuO_2 plane. Unfortunately, this cannot be proven within the current setup[1].

The asymmetric EFG at planar Cu, hitherto explained by the crystal's orthorhombicity, is shown to be in quantitative agreement with the observed oxygen charge ordering. This verifies the validity of the description of the planar Cu and O EFGs by the local hole contents of the bonding orbitals of the CuO_2 plane. Conversely, the asymmetry of the planar Cu EFG gives restrictions to the symmetry of charge ordering and the pressure dependent data signal a modification of the charge order symmetry with pressure.

If planar charge ordering is sensitive to such soft modifications as due to moderate pressures and variations of the temperature, other perturbations may affect the planar electronics as well. For instance, it cannot be excluded that the orthorhombic lattice distortion contributes indirectly to the EFG of the planar nuclei at ambient pressure. Furthermore, the observed O splittings in high magnetic fields as well as the two Cu and O lines due to empty and full chains in (detwinned) Ortho-phases of YBCO [Wu et al., 2011, 2013; Yamani et al., 2004] may just represent another perturbation of the sensitive planar electronics which leads to ordered electronic structures.

---

[1] The necessary orientation aligns simultaneously the NMR coil axis with the external magnetic field which makes NMR experiments impossible.

Chapter 6

Summary, conclusion and outlook

High-temperature superconducting cuprates are still at the center of interest in condensed matter physics even after 30 years of research. Decisive experiments that are able to provide new insights are in demand. Nuclear magnetic resonance (NMR) is a very powerful bulk local probe of chemical and electronic properties of materials, and NMR should be able to provide key information about the properties of the cuprates. In fact, NMR already contributed significantly to the understanding of these materials, in particular with shift and relaxation measurements, but there are outstanding issues that leave NMR data not well understood.

Our group has addressed open issues over the past years and developed high pressure anvil cell NMR, since application of moderate pressure is able to tune the electronic properties of materials while leaving the chemical structure unchanged. The first applications showed that the pseudogap behavior seen with NMR disappears under pressure for $YBa_2Cu_4O_8$ and a two-component shift behavior becomes apparent in this material that was used to prove single-component behavior many years ago.

The focus of this thesis was to explore whether anvil cell NMR can be used to address an issue which concerns the electric field gradient (EFG) of the CuO_2 plane. Most materials show excessive quadrupolar linewidths, i.e., the EFG varies largely across the CuO_2 plane, but there are exceptions, in particular the stoichiometric materials $YBa_2Cu_4O_8$ and $YBa_2Cu_3O_7$, which exhibit rather narrow NMR lines. This well-known observation was taken as proof that inhomogeneity in the cuprates is mostly a chemical issue, i.e., caused by symmetry-breaking doping of these materials, or due to sample quality issues. On the other hand, these stoichiometric materials show substantial line splittings that were attributed to their orthorhombic structure. However, also a contradicting explanation for the NMR data is possible: strong charge density variations in the ubiquitous CuO_2 plane of certain symmetry could explain the data as well. Clearly, this would lead to a new perspective on the NMR linewidth. Using pressure NMR on single crystals it should be possible to address this issue, which was the main subject of this thesis.

For the investigation of the linewidth, the pressure dependence of the EFG experienced by planar Cu and O was measured with NMR in single crystals of $YBa_2Cu_3O_7$ and $YBa_2Cu_3O_{6.9}$. In addition, pressure dependent nuclear quadrupole resonance (NQR) experiments were performed on these samples as well as on powder samples of $YBa_2Cu_4O_8$. While previous pressure NMR/NQR measurements on the cuprates obtained solely the pressure and temperature dependence of the largest principle component of the Cu EFG, in the course of this study the pressure and temperature dependences of the (complete) planar Cu *and* O EFG tensors were measured for the first time. For this, the preparation of the pressure anvil cell for single crystal NMR measurements including the alignment of the tiny crystal with the external magnetic field, constituted a particular challenge of the work for this thesis. The alignment procedure using the planar Cu central transition as well as the planar O satellite transition has been demonstrated to be efficient and precise, and establishes a method that can also be used for the pressure investigation of other cuprates.

Pressure affects the distribution of the planar Cu EFG substantially in all investigated samples. It was shown that pressure inhomogeneities cannot explain these modifications and thus they must represent intrinsic effects. The size of the induced variations of the Cu EFG by pressure is similar to the effect of chemically induced disorder by element substitution. This is unusual since pressure is not supposed to induce disorder, and thus signals an instability of the planar electronic properties.

It was found, that the observed pressure and temperature modifications of the planar Cu and O EFGs in $YBa_2Cu_3O_{6.9}$ cannot be soley related to the crystal structure and composition. In particular, the long-standing interpretation of the planar Cu EFG asymmetry and the two chemical O sites - O(2,3) - as due to the crystal's orthorhombicity could be refuted. The planar EFGs are indeed a consequence of a charge density variation, and pressure and lowering the temperature induce charge ordering. This observation constitutes the first proof of local charge ordering on planar oxygen in $YBa_2Cu_3O_{6+y}$ close to optimal doping and the data at 18 kbar and 100 K are consistent with a charge density wave with d-wave symmetry. It was shown that ordering establishes gradually by lowering the temperature at 18 kbar and that the amplitude of the charge variation is about $\delta_p = 0.01$ holes per O. Furthermore, the amplitude and structure of the O charge ordering explains the measured Cu EFG asymmetry quantitatively. The Cu data indicate a variation of the planar Cu hole content with an amplitude of about $\delta_d = 0.004$. The measured amplitudes are similar to the observed charge density wave amplitudes obtained from the NMR data in high magnetic fields and low temperatures [Kharkov and Sushkov, 2016]. Thus, charge ordering is not an exclusive feature of underdoped $YBa_2Cu_3O_{6+y}$ and pressure affects planar charge ordering.

The influence of a magnetic field on the charge symmetry has been investigated in $YBa_2Cu_3O_7$ at ambient pressure. In this sample, unusual modifications of the Cu EFG distribution were obtained by applying a magnetic field of 11.7 T. First, there is a substantial difference between the width and shape of the distribution of the largest planar Cu EFG component V_{ZZ} without and with a magnetic field. This effect is obtained below 200 K, but above T_c. The measured distribution could be a complex distribution of V_{ZZ} or a line splitting. Second, there is an asymmetric distribution of the Cu EFG asymmetry parameter η at room temperature. The asymmetric distribution is rather constant when the magnetic field is rotated by 90° about crystal's *c*-axis and shows that the EFG orientation depends on the direction of the external magnetic field.
The most striking differences to previous results are that (i) the modifications depend on the direction of the magnetic field, (ii) they occur far above the critical temperature T_c and (iii) they are observed in $YBa_2Cu_3O_{6+y}$ close to optimal doping. This means that spatial planar charge variation and the magnetic field are closer related than often assumed [Chang et al., 2012; Ghiringhelli et al., 2012] and that this relation is not an exclusive element of underdoped $YBa_2Cu_3O_{6+y}$.

Considering all findings in this thesis, the EFG experienced by the nuclei of the CuO_2 plane is not solely determined by the chemical composition and structure of the respective cuprate since it is affected by low energy perturbations such as moderate pressures, magnetic fields and different temperatures. Certainly, weak chemical disorder can be expected to trigger similar effects. In this regard, the Cu quadrupolar linewidth of $YBa_2Cu_3O_7$ - the smallest among the cuprates - may constitute a natural lower boundary. The large planar ^{63}Cu and ^{17}O linewidth of the cuprates which were discussed in this work may then reveal planar charge variations of about $0.002 \leq \delta n_\mathrm{d} \leq 0.07$ for Cu and $0.008 \leq \delta n_\mathrm{p} \leq 0.05$ for O *induced* by chemical disorder.

Whether charge variations in general and charge ordering in particular are of fundamental importance for cuprate physics must be further investigated. It was shown in this thesis that NMR is capable of measuring charge ordering, and NMR can help to understand the relation between the planar electronic structure and cuprate phenomena such as superconductivity and the pseudogap. Furthermore, it was demonstrated that pressure is a tuning parameter for planar charge ordering. In forthcoming experiments, the pressure effects on charge ordering for various doping levels and in different cuprates should be investigated since they will give important information about the connection of charge ordering and the different electronic phases of the cuprates. In particular, the investigation of charge ordering under pressure in the underdoped materials will yield distinct insights to the anomalous suppression of T_{c} in this doping range.

References

N.H. Andersen, M. von Zimmermann, T. Frello, M. Käll, D. Mønster, P.-A. Lindgård, J. Madsen, T. Niemöller, H.F. Poulsen, O. Schmidt, J.R. Schneider, Th. Wolf, P. Dosanjh, R. Liang, and W.N. Hardy. *Physica C*, 317-318:259–269, 1999. doi: 10.1016/S0921-4534(99)00066-0. 7

A. Bianconi, N. L. Saini, A. Lanzara, M. Missori, T. Rossetti, H. Oyanagi, H. Yamaguchi, K. Oka, and T. Ito. *Phys. Rev. Lett.*, 76:3412–3415, 1996. doi: 10.1103/PhysRevLett.76.3412. 25

S. Blanco-Canosa, A. Frano, E. Schierle, J. Porras, T. Loew, M. Minola, M. Bluschke, E. Weschke, B. Keimer, and M. Le Tacon. *Phys. Rev. B*, 90:054513, 2014. doi: 10.1103/PhysRevB.90.054513. 25

R. Blinc. *Physics Reports*, 79:331–398, 1981. doi: 10.1016/0370-1573(81)90108-3. 76

M. Bloom, E. Hahn, and B. Herzog. *Phys. Rev.*, 97:1699–1709, 1955. doi: 10.1103/PhysRev.97.1699. 15

D. Braithwaite, G. Chouteau, G. Martinez, J.L. Hodeau, M. Marezio, J. Karpinski, E. Kaldis, S. Rusiecki, and E. Jilek. *Physica C*, 178:75–80, 1991. doi: 10.1016/0921-4534(91)90160-Z. 58, 61

D. Brinkmann. *Appl. Magn. Reson.*, 3:483–494, 1992. doi: 10.1007/BF03166279. 72

M. Calamiotou, A. Gantis, E. Siranidi, D. Lampakis, J. Karpinski, and E. Liarokapis. *Phys. Rev. B*, 80:1–7, 2009. doi: 10.1103/PhysRevB.80.214517. 57, 67, 84, 86

G. Campi, A. Bianconi, N. Poccia, G. Bianconi, L. Barba, G. Arrighetti, D. Innocenti, J. Karpinski, N.D. Zhigadlo, S.M. Kazakov, M. Burghammer, M. von Zimmermann, M. Sprung, and A. Ricci. *Nature*, 525:359–362, 2015. doi: 10.1038/nature14987. 25, 26

J. Chang, E. Blackburn, A. T. Holmes, N. B. Christensen, J. Larsen, J. Mesot, R. Liang, D.A. Bonn, W.N. Hardy, A. Watenphul, M. von Zimmermann, E. M. Forgan, and S. M. Hayden. *Nat. Phys.*, 8:871–876, 2012. doi: 10.1038/nphys2456. 5, 26, 71, 117

J. Chang, E. Blackburn, O. Ivashko, A. T. Holmes, N. B. Christensen, M. Hücker, R. Liang, D.A. Bonn, W.N. Hardy, U. Rütt, M. von Zimmermann, E. M. Forgan, and S. M. Hayden. *Nat. Commun.*, 7:11494, 2016. doi: 10.1038/ncomms11494. 26, 71, 113

R. Comin, R. Sutarto, F. He, E. H. da Silva Neto, L. Chauviere, A. Fraño, R. Liang, W. N. Hardy, D. A. Bonn, Y. Yoshida, H. Eisaki, A. J. Achkar, D. G. Hawthorn, B. Keimer, G. A. Sawatzky, and A. Damascelli. *Nat. Mater.*, 14:796–800, 2015. doi: 10.1038/nmat4295. 112

Riccardo Comin and Andrea Damascelli. *Annu. Rev. Condens. Matter Phys.*, 7:369–405, 2016. doi: 10.1146/annurev-conmatphys-031115-011401. 25

Kazimierz Conder. *Materials Science and Engineering: R: Reports*, 32:41–102, 2001. doi: 10.1016/S0927-796X(00)00030-9. 7, 47, 48, 50, 83, 86, 98

J. Crocker, A. P. Dioguardi, N. apRoberts Warren, A. C. Shockley, H.-J. Grafe, Z. Xu, J. Wen, G. Gu, and N. J. Curro. *Phys. Rev. B*, 84:224502, 2011. doi: 10.1103/PhysRevB.84.224502. 25

T. P. Croft, C. Lester, M. S. Senn, A. Bombardi, and S. M. Hayden. *Phys. Rev. B*, 89:224513, 2014. doi: 10.1103/PhysRevB.89.224513. 25

E. H. da Silva Neto, P. Aynajian, A. Frano, R. Comin, E. Schierle, E. Weschke, A. Gyenis, J. Wen, J. Schneeloch, Z. Xu, S. Ono, G. Gu, M. Le Tacon, and A. Yazdani. *Science*, 343: 393–396, 2014. doi: 10.1126/science.1243479. 5, 25

E. H. da Silva Neto, R. Comin, F. He, R. Sutarto, Y. Jiang, R. L. Greene, G. A. Sawatzky, and A. Damascelli. *Science*, 347:282–285, 2015. doi: 10.1126/science.1256441. 26

T.P. Das and E.L. Hahn. *Nuclear quadrupole resonance spectroscopy.* Academic Press Inc., New York, 1958. 15, 34

N. Doiron-Leyraud, C. Proust, D. LeBoeuf, J. Levallois, J. Bonnemaison, R. Liang, D.A. Bonn, W.N. Hardy, and L. Taillefer. *Nature*, 447:565–568, 2007. doi: 10.1038/nature05872. 26

F.D. Doty, T.J. Connick, X.Z. Ni, and M.N. Clingan. *J. Magn. Reson.*, 77:536–549, 1988. doi: 10.1016/0022-2364(88)90011-X. 30

A. Erb, E. Walker, and R. Flükiger. *Physica C*, 258:9–20, 1996. doi: 10.1016/0921-4534(95)00807-1. 47, 50

Andreas Erb. *The Impact Of Crystal Growth, Oxygenation And Microstructure On The Physics Of The Rare Earth (123) Superconductors.* habilitation, Université de Genève, 1999. 49

K. Fujita, M. H. Hamidian, S. D. Edkins, C. K. Kim, Y. Kohsaka, M. Azuma, M. Takano, H. Takagi, H. Eisaki, S. Uchida, A. Allais, M. J. Lawler, E.-A. Kim, S. Sachdev, and J. C. S. Davis. *PNAS*, 111:E3026–E3032, 2014. doi: 10.1073/pnas.1406297111. 112

L. Gao, Y. Xue, F. Chen, Q. Xiong, R. Meng, D. Ramirez, C. Chu, J. Eggert, and H. Mao. *Phys. Rev. B*, 50:4260–4263, 1994. doi: 10.1103/PhysRevB.50.4260. 23

G. Ghiringhelli, M. Le Tacon, M. Minola, S. Blanco-Canosa, C. Mazzoli, N.B. Brookes, G. M. De Luca, A. Frano, D.G. Hawthorn, F. He, T. Loew, M. Moretti Sala, D.C. Peets, M. Salluzzo, E. Schierle, R. Sutarto, G.A. Sawatzky, E. Weschke, B. Keimer, and L. Braicovich. *Science*, 337:821–825, 2012. doi: 10.1126/science.1223532. 26, 117

A.A. Gippius, E.V. Antipov, W. Hoffmann, and K. Lüders. *Physica C*, 276:57–64, 1997. doi: 10.1016/S0921-4534(97)00019-1. 56

H. J. Grafe. *Physica C*, 481:93–100, 2012. doi: 10.1016/j.physc.2012.03.073. 25

G. Grissonnanche, O. Cyr-Choinire, F. Lalibert, S. Ren de Cotret, A. Juneau-Fecteau, S. Dufour-Beausjour, M. È. Delage, D. LeBoeuf, J. Chang, B. J. Ramshaw, D. A. Bonn, W. N. Hardy, R. Liang, S. Adachi, N. E. Hussey, B. Vignolle, C. Proust, M. Sutherland, S. Krämer, J.-H. Park, D. Graf, N. Doiron-Leyraud, and L. Taillefer. *Nat. Commun.*, 5: 3280, 2014. doi: 10.1038/ncomms4280. 26

J. Haase and C. P. Slichter. *J. Supercond.*, 16:473–475, 2003. doi: 10.1023/A:1023882516857. 26, 27, 54, 55, 85, 111

J. Haase, C.P. Slichter, R. Stern, C.T. Milling, and D.G. Hinks. *J. Supercond. Inc. Nov. Magn.*, 13:723–726, 2000. doi: 10.1023/A:1007853912812. 17, 55

J. Haase, C.P. Slichter, and C.T. Milling. *J. Supercond.*, 15:339–343, 2002. doi: 10.1023/A:1021014028677. 54, 56, 95

J. Haase, O. Sushkov, P. Horsch, and G. Williams. *Phys. Rev. B*, 69:094504, 2004. doi: 10.1103/PhysRevB.69.094504. 20, 102, 103, 104, 111

J. Haase, S.K. Goh, T. Meissner, P.L. Alireza, and D. Rybicki. *Rev. Sci. Instrum.*, 80:073905, 2009. doi: 10.1063/1.3183504. 35, 36

P. C. Hammel, A. P. Reyes, Z. Fisk, M. Takigawa, J. D. Thompson, R. H. Heffner, S-W. Cheong, and J. E. Schirber. *Phys. Rev. B*, 42:6781–6783, 1990. doi: 10.1103/PhysRevB.42.6781. 25

Z.S. Hartwig, C.B. Haakonsen, R.T. Mumgaard, and L. Bromberg. *Fusion Engineering and Design*, 87:201–214, 2012. doi: 10.1016/j.fusengdes.2011.10.002. 6

J. E. Hoffman, E. W. Hudson, K. M. Lang, V. Madhavan, H. Eisaki, S. Uchida, and J. C. Davis. *Science*, 295(5554):466–469, 2002. doi: 10.1126/science.1066974. 25

M. Horvatić, C. Berthier, Y. Berthier, P. Ségransan, P. Butaud, W. G. Clark, J. A. Gillet, and J. Y. Henry. *Phys. Rev. B*, 48:13848–13864, 1993. doi: 10.1103/PhysRevB.48.13848. 87

M. Hücker, N. B. Christensen, A. T. Holmes, E. Blackburn, E. M. Forgan, R. Liang, D. A. Bonn, W. N. Hardy, O. Gutowski, M. von Zimmermann, S. M. Hayden, and J. Chang. *Phys. Rev. B*, 90:054514, 2014. doi: 10.1103/PhysRevB.90.054514. 26, 71, 113

P. Hüsser, E. Stoll, H.U. Suter, and P.F. Meier. *Physica C*, 294:217–224, 1998. doi: 10.1016/S0921-4534(97)01653-5. 72, 85

T. Imai, C. P. Slichter, K. Yoshimura, and K. Kosuge. *Phys. Rev. Lett.*, 70:1002–1005, 1993. doi: 10.1103/PhysRevLett.70.1002. 56

M. Jurkutat. *NMR of Electron-Doped High-Temperature Superconductor* $Pr_{2-x}Ce_xCuO_4$. PhD thesis, Universität Leipzig, 2015. 56

M. Jurkutat, J. Haase, and A. Erb. *J. Supercond. Nov. Magn.*, 26:2685–2688, 2013. doi: 10.1007/s10948-013-2160-1. 25

M. Jurkutat, D. Rybicki, O. P. Sushkov, G. V. M. Williams, A. Erb, and J. Haase. *Phys. Rev. B*, 90:140504, 2014. doi: 10.1103/PhysRevB.90.140504. 20, 21, 25, 54, 56, 67, 102, 111

M. Jurkutat, J. Kohlrautz, S. Reichardt, A. Erb, G. V. M. Williams, and J. Haase. NMR of cuprate superconductors: Recent developments. pages 77–97. Springer International Publishing, Cham, 2017. doi: 10.1007/978-3-319-52675-1_8. 21, 22

Michael Jurkutat. to be published. 2017. 103

J. Karpinski, E. Kaldis, E. Jilek, S. Rusiecki, and B. Bucher. *Nature*, 336:660–662, 1988. doi: 10.1038/336660a0. 7, 86

Y. A. Kharkov and O. P. Sushkov. *Scientific Reports*, 6:34551, 2016. doi: 10.1038/srep34551. 111, 113, 117

K. Kitagawa, N. Katayama, H. Gotou, T. Yagi, K. Ohgushi, T. Matsumoto, Y. Uwatoko, and M. Takigawa. *Phys. Rev. Lett.*, 103:257002, 2009. doi: 10.1103/PhysRevLett.103.257002. 45

S. A. Kivelson and E. Fradkin. How optimal inhomogeneity produces high temperature superconductivity. In *Handbook of High-Temperature Superconductivity*, pages 570–596. Springer New York, New York, NY, 2007. doi: 10.1007/978-0-387-68734-6_15. 25

S. A. Kivelson, I. P. Bindloss, V. Oganesyan, J. M. Tranquada, A. Kapitulnik, and C. Howald. *Rev. Mod. Phys.*, 75:1201–1241, 2003. doi: 10.1103/RevModPhys.75.1201. 25

S. Klotz, W. Reith, and J.S. Schilling. *Physica C*, 172:423–426, 1991. doi: 10.1016/0921-4534(91)90208-G. 24

D. LeBoeuf, N. Doiron-Leyraud, J. Levallois, R. Daou, J.-B. Bonnemaison, N. E. Hussey, L. Balicas, B. J. Ramshaw, R. Liang, D. A. Bonn, W. N. Hardy, S. Adachi, C. Proust, and L. Taillefer. *Nature*, 450:533–536, 2007. doi: 10.1038/nature06332. 26

D. LeBoeuf, S. Krämer, W. N. Hardy, R. Liang, D. A. Bonn, and C. Proust. *Nat. Phys.*, 9: 79–83, 2012. doi: 10.1038/nphys2502. 26

Jeongseop A. Lee, Yizhou Xin, W. P. Halperin, A. P. Reyes, P. L. Kuhns, and M. K. Chan. *New J. Phys.*, 19:033024, 2017. doi: 10.1088/1367-2630/aa6277. 54, 56

Y.K. Lee. *Concepts Magn. Reson.*, 14:155–171, 2002. doi: 10.1002/cmr.10023. 34

R. Liang, D.A Bonn, and W. N Hardy. *Physica C*, 336:57–62, 2000. doi: 10.1016/S0921-4534(00)00091-5. 7, 84, 100

R. Liang, D. A. Bonn, and W. N. Hardy. *Phys. Rev. B*, 73:180505, 2006. doi: 10.1103/PhysRevB.73.180505. 18, 19, 47

O. Lutz, H. Oehler, and P. Kroneck. *Zeitschrift für Physik A*, 288:17–21, 1978. doi: 10.1007/BF01408195. 33

T. Machi, I. Tomeno, T. Miyatake, K. Tai, N. Koshizuka, A. Hayashi, Y. Ueda, T. Imai, and H. Yasuoka. ^{63}Cu and ^{17}O nuclei spin-lattice relaxation in $Y_{1-x}Ca_xBa_2Cu_4O_8$. In H. Hayakawa and N. Koshizuka, editors, *Advances in Superconductivity IV*, pages 115–118. Springer Japan, Tokyo, 1992. doi: 10.1007/978-4-431-68195-3_22. 71

T. Machi, M. Kosuge, N. Koshizuka, and H. Yasuoka. NQR study in $YBa_2Cu_4O_8$ under pressure. In Tadataka Yamafuji, KaoruMorishita, editor, *Advances in Superconductivity VII*, pages 151–154. Springer Japan, Tokyo, 1995. doi: 10.1007/978-4-431-68535-7_33. 26, 57, 60, 69

T. Machi, M. Kosuge, N. Koshizuka, and H. Yasuoka. *J. Magn. Magn. Mater.*, 177-181: 525–526, 1998. doi: 10.1016/S0304-8853(97)00969-4. 45, 60

M. Mali, D. Brinkmann, L. Pauli, J. Roos, H. Zimmermann, and J. Hulliger. *Phys. Lett. A*, 124:112–116, 1987. doi: 10.1016/0375-9601(87)90384-7. 72

P. P. Man, J. Klinowski, A. Trokiner, H. Zanni, and P. Papon. *Chem. Phys. Lett.*, 151: 143–150, 1988. doi: 10.1016/0009-2614(88)80085-X. 14, 31, 50

I. Mangelschots, M. Mali, J. Roos, H. Zimmermann, D. Brinkmann, S. Rusiecki, J. Karpinski, E. Kaldis, and E. Jilek. *Physica C*, 172:57–62, 1990. doi: 10.1016/0921-4534(90)90642-R. 71

I. Mangelschots, M. Mali, J. Roos, D. Brinkmann, S. Rusiecki, J. Karpinski, and E. Kaldis. *Physica C*, 194:277–286, 1992. doi: 10.1016/S0921-4534(05)80005-X. 54, 86

H. K. Mao, P. M. Bell, J. W. Shaner, and D. J. Steinberg. *J. Appl. Phys.*, 49:3276–3283, 1978. doi: 10.1063/1.325277. 36

T. Meier, T. Herzig, and J. Haase. *Rev. Sci. Instrum.*, 85:043903, 2014. doi: 10.1063/1.4870798. 35, 36

T. Meier, S. Reichardt, and J. Haase. *J. Magn. Reson.*, 257:39–44, 2015. doi: 10.1016/j.jmr.2015.05.007. 35

Thomas Meier. *High Sensitivity Nuclear Magnetic Resonance at Extreme Pressures.* PhD thesis, University of Leipzig, 2016. 35

T. Meissner, S. K. Goh, J. Haase, G. V. M. Williams, and P. B. Littlewood. *Phys. Rev. B*, 83:220517, 2011. doi: 10.1103/PhysRevB.83.220517. 1, 19

Thomas Meissner. *Exploring Nuclear Magnetic Resonance at the Highest Pressures.* PhD thesis, University of Leipzig, 2012. 26, 35, 57, 58

A. R. Moodenbaugh, Y. Xu, M. Suenaga, T. J. Folkerts, and R. N. Shelton. *Phys. Rev. B*, 38:4596–4600, 1988. doi: 10.1103/PhysRevB.38.4596. 19

N. Mori, C. Murayama, H. Takahashi, H. Kaneko, K. Kawabata, Y. Iye, S. Uchida, H. Takagi, Y. Tokura, Y. Kubo, H. Sasakura, and K. Yamaya. *Physica C*, 185-189:40–44, 1991. doi: 10.1016/0921-4534(91)91947-3. 23, 24

K. Müller, M. Mali, J. Roos, and D. Brinkmann. *Physica C*, 162-164:173–174, 1989. doi: 10.1016/0921-4534(89)90973-8. 40, 63

C. Murayama, Y. Iye, T. Enomoto, N. Mori, Y. Yamada, T. Matsumoto, Y. Kubo, Y. Shimakawa, and T. Manako. *Physica C*, 183:277–285, 1991. doi: 10.1016/0921-4534(91)90573-H. 24

T. Nakano, S. Tsutsumi, N. Fujiwara, S. Matsuishi, and H. Hosono. *Phys. Rev. B*, 83:180508, 2011. doi: 10.1103/PhysRevB.83.180508. 45

J. Neumeier and H. Zimmermann. *Phys. Rev. B*, 47:8385–8388, 1993. doi: 10.1103/PhysRevB.47.8385. 24, 47

S. Ohsugi, Y. Kitaoka, K. Ishida, G. Zheng, and K. Asayama. *J. Phys. Soc. Japan*, 63: 700–715, 1994. doi: 10.1143/JPSJ.63.700. 54, 56

C. V. Parker, P. Aynajian, E. H. da Silva Neto, A. Pushp, S. Ono, J. Wen, Z. Xu, G. Gu, and A. Yazdani. *Nature*, 468:677–680, 2010. doi: 10.1038/nature09597. 19

C. H. Pennington. *Single Crystal NMR of High Temperature Superconductors.* PhD thesis, University of Illinois at Urbana-Champaign, 1989. 78, 79

C.H. Pennington and C.P. Slichter. Nuclear resonance studies of $YBa_2Cu_3O_{7-\delta}$. In *Physical Properties of High Temperature Superconductors II*, pages 269–367. World Scientific Publishing Co. Pte. Ltd., Singapore, 1990. doi: 10.1142/9789814343046_0005. 8, 11, 41, 77, 78, 84, 85, 89, 94, 95, 96, 97, 98

L. Pintschovius, Y. Endoh, D. Reznik, H. Hiraka, J. Tranquada, W. Reichardt, P. Bourges, Y. Sidis, H. Uchiyama, T. Masui, and S. Tajima. *Physica C*, 412-414:70–75, 2004. doi: 10.1016/j.physc.2004.01.065. 26

M. Raichle, D. Reznik, D. Lamago, R. Heid, Y. Li, M. Bakr, C. Ulrich, V. Hinkov, K. Hradil, C. T. Lin, and B. Keimer. *Phys. Rev. Lett.*, 107:177004, 2011. doi: 10.1103/PhysRevLett.107.177004. 26

S. Reichardt, M. Jurkutat, A. Erb, and J. Haase. *J. Supercond. Nov. Magn.*, 29:3017–3022, 2016. doi: 10.1007/s10948-016-3827-1. 55, 74

S. Renold, S. Pliberšek, E.P. Stoll, T.A. Claxton, and P.F. Meier. *Eur. Phys. J. B*, 23:3–15, 2001. doi: 10.1007/s100510170077. 72, 85

J. H. Ross, Z. Wang, and C. P. Slichter. *Phys. Rev. Lett.*, 56:663–666, 1986. doi: 10.1103/PhysRevLett.56.663. 76

D. Rybicki, J. Haase, M. Greven, G. Yu, Y. Li, Y. Cho, and X. Zhao. *J. Supercond. Nov. Magn.*, 22:179–183, 2009. doi: 10.1007/s10948-008-0376-2. 22, 25, 69

D. Rybicki, M. Jurkutat, S. Reichardt, and J. Haase. *arXiv:1402.4014*, page 14, 2014. 20

D. Rybicki, M. Jurkutat, S. Reichardt, C. Kapusta, and J. Haase. *Nat. Commun.*, 7:11413, 2016. doi: 10.1038/ncomms11413. 6, 20, 22, 25, 111

Damian Rybicki, Jurgen Hasse, Marc Lux, Michael Jurkutat, Martin Greven, Guichuan Yu, Yuan Li, and Xudong Zhao. *arXiv:1208.4690*, pages 1–15, 2012. 54, 56

S. Sadewasser, J. Schilling, A. Paulikas, and B. Veal. *Phys. Rev. B*, 61:741–749, 2000. doi: 10.1103/PhysRevB.61.741. 23, 24, 57, 58

Sebastian Sambala. Einkristall-NMR am Hochtemperatursupraleiter $YBa_2Cu_4O_8$. Master's thesis, University of Leipzig, 2010. 59

H. Schiefer, M. Mali, J. Roos, H. Zimmermann, D. Brinkmann, S. Rusiecki, and E. Kaldis. *Physica C*, 162-164:171–172, 1989. doi: 10.1016/0921-4534(89)90972-6. 26, 47

J. S. Schilling. *J. Phys. Chem. Solids*, 59:553–568, 1998. doi: 10.1016/S0022-3697(97)00207-2. 23

J. S. Schilling. High-pressure effects. In *Handbook of High-Temperature Superconductivity*, pages 427–462. Springer New York, New York, NY, 2007. doi: 10.1007/978-0-387-68734-6_11. 5, 19, 23, 24, 47, 65

P. Schleger, W.N. Hardy, and B.X. Yang. *Physica C*, 176:261–273, 1991. doi: 10.1016/0921-4534(91)90722-B. 50

H. J. Schneider-Muntau. *Solid State Nucl. Magn. Reson.*, 9:61–71, 1997. doi: 10.1016/S0926-2040(97)00044-1. 6

J. R. Schrieffer and J. S. Brooks, editors. *Handbook of High-Temperature Superconductivity.* Springer New York, New York, NY, 2007. doi: 10.1007/978-0-387-68734-6. 1, 5

T. Shimizu. *J. Phys. Soc. Japan*, 62:772–778, 1993. doi: 10.1143/JPSJ.62.772. 67

P. M. Singer, A. W. Hunt, and T. Imai. *Phys. Rev. Lett.*, 88:047602, 2002. doi: 10.1103/PhysRevLett.88.047602. 22, 25, 26

C. P. Slichter. *Principles of Magnetic Resonance.* Springer Series in Solid-State Sciences. Springer Berlin Heidelberg, Berlin, Heidelberg, 3 edition, 1990. doi: 10.1007/978-3-662-09441-9. 16

C. P. Slichter. *Magnetic Resonance Studies of High Temperature Superconductors*, pages 215–256. Springer New York, New York, NY, 2007. doi: 10.1007/978-0-387-68734-6_5. 1, 8, 19

B. H. Suits. Nuclear quadrupole resonance spectroscopy. In *Handbook of Applied Solid State Spectroscopy*, chapter 2. Springer US, Boston, MA, 2006. doi: 10.1007/0-387-37590-2. 34

A. Suter, M. Mali, J. Roos, D. Brinkmann, J. Karpinski, and E. Kaldis. *Phys. Rev. B*, 56:5542–5551, 1997. doi: 10.1103/PhysRevB.56.5542. 69

A. Suter, M. Mali, J. Roos, and D. Brinkmann. *J. Phys. Condens. Matter*, 10:5977, 1998. doi: 10.1088/0953-8984/10/26/022. 14

W. Tabis, Y. Li, M. Le Tacon, L. Braicovich, A. Kreyssig, M. Minola, G. Dellea, E. Weschke, M. J. Veit, M. Ramazanoglu, A. I. Goldman, T. Schmitt, G. Ghiringhelli, N. Barišić, M. K. Chan, C. J. Dorow, G. Yu, X. Zhao, B. Keimer, and M. Greven. *Nat. Commun.*, 5:5875, 2014. doi: 10.1038/ncomms6875. 5, 25

M. Takigawa, P. Hammel, R. Heffner, Z. Fisk, K. Ott, and J. Thompson. *Phys. Rev. Lett.*, 63:1865–1868, 1989. doi: 10.1103/PhysRevLett.63.1865. 55, 86

M. Takigawa, A. Reyes, P. Hammel, J. Thompson, R. Heffner, Z. Fisk, and K. Ott. *Phys. Rev. B*, 43:247–257, 1991. doi: 10.1103/PhysRevB.43.247. 86

J. M. Tranquada, B. J. Sternlieb, J. D. Axe, Y. Nakamura, and S. Uchida. *Nature*, 375: 561–563, 1995. doi: 10.1038/375561a0. 19, 25

J. M. Tranquada, J. D. Axe, N. Ichikawa, A. R. Moodenbaugh, Y. Nakamura, and S. Uchida. *Phys. Rev. Lett.*, 78:338–341, 1997. doi: 10.1103/PhysRevLett.78.338. 26

Y. J. Uemura, G. M. Luke, B. J. Sternlieb, J. H. Brewer, J. F. Carolan, W. N. Hardy, R. Kadono, J. R. Kempton, R. F. Kiefl, S. R. Kreitzman, P. Mulhern, T. M. Riseman, D. Ll. Williams, B. X. Yang, S. Uchida, H. Takagi, J. Gopalakrishnan, A. W. Sleight, M. A. Subramanian, C. L. Chien, M. Z. Cieplak, Gang Xiao, V. Y. Lee, B. W. Statt, C. E. Stronach, W. J. Kossler, and X. H. Yu. *Phys. Rev. Lett.*, 62:2317–2320, 1989. doi: 10.1103/PhysRevLett.62.2317. 22

E.N. Van Eenige, R. Griessen, R.J. Wijngaarden, J. Karpinski, E. Kaldis, S. Rusiecki, and E. Jilek. *Physica C*, 168:482–488, 1990. doi: 10.1016/0921-4534(90)90066-N. 61

R. E. Walstedt. *The NMR Probe of High-Tc Materials*, volume 228 of *Springer Tracts in Modern Physics*. Springer Berlin Heidelberg, Berlin, Heidelberg, 1 edition, 2008. doi: 10.1007/978-3-540-75565-4. 1, 7, 8, 11, 12, 19

R. J. Wijngaarden, D. Tristan Jover, and R. Griessen. *Phys. B Condens. Matter*, 265:128–135, 1999. doi: 10.1016/S0921-4526(98)01342-8. 23

G. V. M. Williams. *Phys. Rev. B*, 76:094502, 2007. doi: 10.1103/PhysRevB.76.094502. 25, 26, 48, 55, 70, 71

G. V. M. Williams, S. Krämer, and M. Mehring. *Phys. Rev. B*, 63:104514, 2001. doi: 10.1103/PhysRevB.63.104514. 55, 71

F. Wolf, D. Kline, and H.S. Story. *J. Chem. Phys.*, 53:3538, 1970. doi: 10.1063/1.1674529. 12

T. Wu, H. Mayaffre, S. Krämer, M. Horvatić, C. Berthier, W. N. Hardy, R. Liang, D. A. Bonn, and M.-H. Julien. *Nature*, 477:191–194, 2011. doi: 10.1038/nature10345. 2, 27, 53, 56, 71, 76, 113

T. Wu, H. Mayaffre, S. Krämer, M. Horvatić, C. Berthier, P. L. Kuhns, A. P. Reyes, R. Liang, W. N. Hardy, D. A. Bonn, and M.-H. Julien. *Nat. Commun.*, 4:2113, 2013. doi: 10.1038/ncomms3113. 27, 53, 56, 71, 113

T. Wu, H. Mayaffre, S. Krämer, M. Horvatić, C. Berthier, W.N. Hardy, R. Liang, D. A. Bonn, and M.-H. Julien. *Nat. Commun.*, 6:6438, 2015. doi: 10.1038/ncomms7438. 56, 87

Z. Yamani, W.A. MacFarlane, B.W. Statt, D. Bonn, R. Liang, and W.N. Hardy. *Physica C*, 405:227–239, 2004. doi: 10.1016/j.physc.2004.02.010. 113

Y. Yoshinari, H. Yasuoka, Y. Ueda, K.-i. Koga, and K. Kosuge. *J. Phys. Soc. Japan*, 59: 3698–3711, 1990. doi: 10.1143/JPSJ.59.3698. 54, 55, 56, 69, 86

G.-q. Zheng, E. Yanase, K. Ishida, Y. Kitaoka, K. Asayama, Y. Kodama, R. Tanaka, S. Nakamichi, and S. Endo. *Solid State Commun.*, 79:51–55, 1991. doi: 10.1016/0038-1098(91)90478-E. 67, 68

G.-q. Zheng, Y. Kitaoka, K. Asayama, Y. Kodama, and Y. Yamada. *Physica C its Appl.*, 193:154–162, 1992. doi: 10.1016/0921-4534(92)90882-D. 86

G.-q. Zheng, T. Mito, Y. Kitaoka, K. Asayama, and Y. Kodama. *Physica C*, 243:337–341, 1995. doi: 10.1016/0921-4534(95)00029-1. 57

G.-q. Zheng, Y. Kitaoka, K. Asayama, K. Hamada, H. Yamauchi, and S. Tanaka. *Physica C*, 260:197–210, 1996. doi: 10.1016/0921-4534(96)00092-5. 56

H. Zimmermann, D. Brinkmann, M. Mali, J. Roos, F. Greuter, and P. Kluge-Weiss. *Physica C*, 153-155:739–740, 1988. doi: 10.1016/S0921-4534(88)80064-9. 26, 47, 69

H. Zimmermann, M. Mali, D. Brinkmann, J. Karpinski, E. Kaldis, and S. Rusiecki. *Physica C*, 159:681–688, 1989. doi: 10.1016/0921-4534(89)91304-X. 54, 69

H. Zimmermann, M. Mali, I. Mangelschots, J. Roos, D. Brinkmann, J. Karpinski, S. Rusiecki, and E. Kaldis. *J. Less Common Met.*, 164-165:132–137, 1990. doi: 10.1016/0022-5088(90)90206-Y. 57, 59, 67